Dynamics of Athermal Suspensions

CHACKO, RAHUL,NINAN

Dynamics of Athermal Suspensions

Rahul N. Chacko

A Thesis presented for the degree of
Doctor of Philosophy

Supervised by Prof. Suzanne Fielding
Department of Physics
University of Durham
UK

February 2019

Abstract

Suspensions are systems composed of particles dispersed in a fluid. This is an industrially important set of materials, whose members are capable of exhibiting a diverse range of phenomena. The behaviour of dense suspensions, where the volume fraction of particles is close to the volume fraction of jamming at which the suspension is unable to flow in the limit of vanishing imposed stress, is particularly challenging to model and explain.

In this thesis, we report theoretical research on three dense athermal suspensions, supported in each case by particle simulations. By studying systems in which particles do not undergo Brownian motion, we are able to identify behaviour generic to both thermal and athermal suspensions, and provide insight into the underlying cause. The particle simulations are found to be of great importance in challenging the assumptions of models, testing model predictions and providing direct microstructural insight into the mechanisms by which dense suspensions evolve.

We first extend a model of discontinuous shear thickening in steady-state homogeneous dense suspensions under simple shear to a dynamical one-dimensional model of the suspension, spatially resolved along the vorticity axis with periodic boundary conditions. This model encapsulates a theory of shear thickening in which a suspension of frictional particles transitions from frictionless to frictional rheology as repulsive interparticle forces that prevent contact between particles at low stress are overcome at high stress. We show that in our model, large homogeneous systems are linearly unstable to perturbations along this axis at high volume fractions within a range of imposed stresses. We characterise two long-time inhomogeneous states, both of which are unsteady but periodic. We then test our predictions with particle simulations of a suspension of frictional particles with short-ranged repulsions, finding both states at least transiently, according to parameter regime.

The second suspension we consider corresponds to the first in the limit of vanishing interparticle repulsion, after a reversal of the direction of shear from steady state. This system is strongly dimensionally and symmetrically constrained: shear-

rate provides the only timescale, while the system is invariant under inversion of the vorticity axis (or, equivalently, simultaneous inversion of the flow and flow gradient axes). We leverage these constraints to develop a systematic approach to modelling the evolution of the "fabric tensor", a traceless and symmetric rank-2 tensor related to the second-order spherical harmonic expansion of the distribution of (near-)contact pairs of particles commonly used in the literature to encode the suspension microstructure, as a function of itself and the imposed velocity gradient tensor. By fitting the models to data from particle simulations of the appropriate system, we show that such models are unsuccessful at linear order in the fabric tensor components, and are unlikely to contain any physical insight at higher orders. We then test the suitability of the fabric tensor as a description of the microstructure directly using the particle simulations, and conclude that a second-order spherical harmonic description captures the pair distribution poorly shortly after reversal. We find that a fourth-order description captures the pair distribution well.

Finally, we study a suspension of soft elastic particles close to and above jamming using particle simulations with periodic boundary conditions. We prepare the suspension at a non-zero temperature and then allow it to relax athermally to the global system's local minimum. We observe non-trivial dynamics, such as slow power-law decay of the root mean squared velocity of particles, and coarsening with a power-law growth of velocity correlation lengths. This suggests that generic athermal physics may in fact underlie non-trivial dynamics commonly associated to thermal effects.

Declaration

The work in this thesis is based on research carried out at Durham University under the supervision of Prof. Suzanne Fielding, of the Department of Physics, Durham University, UK, and Prof. Michael Cates, of DAMTP, University of Cambridge, UK. Chapters 2–5 report research conducted under the supervision of Profs. Fielding and Cates, and in close collaboration with Dr. Romain Mari. Chapter 6 reports research conducted under the supervision by Prof. Fielding and in close collaboration with Prof. Peter Sollich. No part of this thesis has been submitted elsewhere for any other degree or qualification and it is all my own work unless referenced to the contrary in the text.

Publications

R. N. Chacko, P. Sollich, and S. M. Fielding. Slow coarsening in jammed athermal soft particle suspensions. arxiv:1903.00991.

R. N. Chacko, R. Mari, M. E. Cates, and S. M. Fielding. Dynamic vorticity banding in discontinuously shear thickening suspensions. *Physical Review Letters* **121**, 108003 (2018).

R. N. Chacko, R. Mari, S. M. Fielding, and M. E. Cates. Shear reversal in dense suspensions: the challenge to fabric evolution models from simulation data. *Journal of Fluid Mechanics* **847**, 700 (2018).

Acknowledgements

My doctoral studies were conducted within the framework of the Soft Matter and Functional Interfaces Center for Doctoral Training (SOFI CDT). SOFI CDT provided the vehicle for my PhD funding by Durham University (see formal funding acknowledgement at the end of this section), so that my PhD would trivially not have been possible without it, but SOFI's contributions to my academic upbringing extend far beyond that. SOFI provided invaluable exposure to a wide variety of soft matter topics by experts at the Universities of Durham, Leeds and Edinburgh and at SOFI CDT's industrial partners. It also meant being made part of a growing network of soft matter scientists that I am certain will continue to expand and flourish in the coming years. I am thus indebted to all those who worked to make SOFI CDT happen, among whom Lian Hutchings and Julie McLoughlin deserve particular praise.

I am grateful to Christopher Ness, Ben Guy and Andrew Clarke for inviting me to come and see them at their institutions, or coming and seeing me in Durham, occasions in which I learned much from their considerable expertise. I am also grateful to M. Imran, formerly of the Department of Mathematics, who created the template from which the formatting of this thesis is adapted.

I am deeply thankful for the great people I have had around me over the last four years, whose support and friendship kept me going through the ups and downs that mark any doctoral journey. Thanks in particular go to SOFI CDT cohort 1, the CMP group at Durham, and the John Duck pub quiz lot. My OC215 office mates, Hugh Barlow, Clara Despard and Nessa Woodhouse, have had to put up with more of me than most people, and for this they deserve sympathy and my thanks for being brilliant people. I owe a particular debt of gratitude to Ben Robertson, my flatmate

for my entire time at Durham. I could not have wished for a better flatmate.

I am grateful to Ewan Hemingway and Ranga Radhakrishnan for teaching me the ropes in Durham, at a time when I could barely use Linux or define the stress tensor. Along with Romain Mari, they have had a large influence on my development as a scientist, encouraging among other things my adoption of Python and C++. I am especially indebted to Romain and his deep scientific insight, vast knowledge of the suspensions literature, and willingness to lend a patient ear to my half-formed ideas.

I am privileged to have had two wonderful collaborators in the course of my research, Romain who provided the particle simulation data for the work in Chs. 3–5, and Peter Sollich who, along with Suzanne Fielding, guided the research shown in Ch. 6.

None of the research in this thesis would have been possible without the guidance of my supervisors, Suzanne Fielding and Mike Cates. I am grateful for their responsiveness throughout my studies, for lending me so much of their time, and for their immense patience with me. Their feedback, advice and support has been incredibly valuable in helping me grow as a scientist.

Finally, I am thankful to my family, who have been a pillar of moral support throughout my PhD.

The work in this thesis was funded by SOFI CDT, Durham University, and the EPSRC (EP/L015536/1).

Contents

Chapter 1

Introduction

Suspensions are materials made up of particles dispersed in a fluid, where the fluid can be treated as continuous on the length scale of the particles. This broad category includes wet granular matter [1], smoke [2], blood [3], foam [4] and cornstarch in water [5], as well as many more substances. Unsurprisingly, given the diversity of materials that fit the definition, the question of how suspensions behave, particularly under flow, is industrially important. For instance, suspensions of hard particles at high solid volume fraction can solidify in strong flows, leading to the failure of mixing motors and damage to mixing blades in industrial processes [6]. By contrast, other suspensions, such as melted chocolate [7], flow more easily in strong flows, which also influences their processing [8].

As well as their industrial significance, suspensions are of physical interest. Historically, Einstein's calculation of the influence of particle concentration on the viscosity of dilute suspensions [9] led to an estimate of Avogadro's constant, important in the context of the atomic theory of matter. More recently, colloids—suspensions of small particles which undergo Brownian motion—have proved useful as model crystals, allowing scientists to study defect motion [10] and the melting transition [11] in an easy-to-image [12] system. Dense amorphous colloidal systems, for their part, are useful in the study of the glass transition [13], an apparent phase transition from a fluid to a solid with no obvious structural signature.

The behaviour of a given suspension will depend on the size [14,15], shape [16,17], hardness [18], polydispersity [19], inertia [20], and concentration of the particles [21],

as well as the material properties of the suspending fluid [22, 23]. In this thesis, we will be chiefly concerned with dense suspensions of spherical particles of radius $\gtrsim 1\,\mu$m [15] whose density is matched with that of the suspending fluid, which we take to be Newtonian, so as to be neutrally buoyant and which do not, on experimental timescales (e.g. $\sim 70\,$h [24]), experience Brownian motion, yet are small enough (radius $\lesssim 10^2\,\mu$m [25]) for particle inertia to be negligible. Many properties of suspensions linked to shape [26] or thermal effects [27] are shared by non-colloidal suspensions of spheres, so we can study these as a minimal system with which to hopefully probe the underlying physics. (The assumptions of negligible inertia and density matching are further simplifications to increase the tractability of the study.) This idea, of exploiting the minimal nature of athermal suspensions of spheres to study generic behaviour also seen in other systems, is one of the two major themes of this thesis. The other is the power of particle simulations of suspensions to aid in this endeavour.

1.1 Layout of thesis

We will explore these themes in the context of three different systems, which will be discussed across four chapters, with a preliminary chapter covering the prerequisite fluid dynamical and rheological background for the following chapters and a conclusion chapter in which we discuss the particular and overall conclusions of the results in this thesis.

1.1.1 Ch. 2: Background

Suspensions encountered in nature, industry or daily life usually contain a large number of particles (e.g. 1 litre of a suspension of $10\,\mu$m-diameter spheres at a volume fraction $\phi = 0.4$ contains $\sim 10^{11}$ particles), so it is necessary to "coarse-grain", or average out details at the microscopic (particle-scale) level, and obtain a description of the suspension on a scale closer to that seen in applications. In Ch. 2, we will describe the approaches to doing so that we will use in this thesis.

The mediating fluid is a defining feature of a suspension, and so Ch. 2 will

introduce the fluid mechanical concepts necessary to understanding the following chapters of the thesis. We will cover the Navier-Stokes equations, key dimensionless quantities, the Stokes limit of vanishing inertia and the resulting Stokes equations, and key objects such as the stress tensor.

Much of this thesis will rely on the particle simulations of Dr. Romain Mari. We will therefore describe the basics of his approach in Ch. 2.

We will, in this thesis, be exclusively interested in the dense regime, in which the volume fraction of particles is so high that the suspension is close to (Chs. 3–5) or above (Ch. 6) the point at which it acts like a solid at low stresses. This "jamming transition" will be also be introduced in Ch. 2.

Finally, the majority of this thesis involves rheology—the study of flow—and so Ch. 2 will also briefly review experimental approaches to rheology in the context of a particularly simple type of flow, shear flow, which we will be studying in this thesis.

1.1.2 Ch. 3: Vorticity banding in dense suspensions

A suspension of cornstarch in water can, at high cornstarch concentration, become hard enough upon impact to run across. This is a manifestation of a phenomenon known as shear thickening, in which the viscosity of a fluid increases as it is deformed at a higher rate. The precise mechanism through which shear thickening occurs in cornstarch has been controversial, but recent research supports a view in which shear thickening results from frictional contact between particles. Given short-ranged repulsive interactions between particles which prevents contact at low imposed stress, the suspension rheology can interpolate between that of frictionless particles to one of frictional particles as stress is increased, and it is this interpolation which is thought to result in the shear thickening observed in suspensions.

A recent model encapsulates this mechanism in a scalar, steady-state description of the suspension rheology. In particular, it explains discontinuous increases in stress as shear rate is increased by the existence of an underlying S-shaped constitutive curve of stress against shear rate. However, homogeneous flow in negatively-sloped regions of stress versus strain constitutive curves is expected to be unstable to small

perturbations.

In Ch. 3, we consider a dense, non-Brownian suspension of hard particles with short-ranged interparticle repulsive forces and frictional contact interactions under an imposed shear flow. Using a minimal extension of the aforementioned scalar model to a dynamical model in one-dimension, we show that homogeneous flow in large systems of this type is unstable to perturbations. We identify two limiting states that such perturbations can grow into, and, at least transiently, find both of these states in particle simulations of this system, according to parameter regime.

We also use the particle simulations to directly test the equations that make our model, determining which equations work well and which would be the most profitable equations to seek improvements of.

1.1.3 Ch. 4: Fabric tensor dynamics of dense non-Brownian suspensions: phenomenological modelling

Having had some success with a one-dimensional model, we next seek to understand the scope for developing a full, three dimensional model for the rheology of dense suspensions. A strategy employed with success in liquid crystal and polymer contexts is to, implicitly or otherwise, express the stress as a function of a conformation tensor which encodes the microstructure of the material. A model of the microstructural evolution of the material then yields a constitutive equation. We follow previous authors in emulating this approach in the suspensions context by defining a rank-2 traceless and symmetric "fabric" tensor, the detraced second moment of the distribution of near-contact orientations, whose evolution we then attempt to model.

We test our models using Dr. Mari's particle simulations. To ensure that the test is sufficiently stringent for a successful model to require physical insight, we adopt a protocol in which the direction of shear is reversed from steady state at a time defined as $t = 0$. At early strains after this point, structure formed by the pre-reversal flow is broken up. At later strains, the post-reversal flow forms new structure as a new steady state is approached. We model the evolution of the fabric tensor across this transition.

To minimise the number of complicating ingredients to account for, we study the case of a suspension without short-ranged repulsive interactions between particles, in simple shear flow. We show that the symmetries and lack of ingredients of such a system can be exploited to develop three-dimensional models for the evolution of the fabric tensor in a modular way.

In the end, however, we conclude that any fabric tensor model of this kind is unlikely to be physically meaningful.

1.1.4 Ch. 5: Fabric tensor dynamics of dense non-Brownian suspensions: microstructural insights

The results of the previous section lead us to query the assumptions underlying the use of a fabric tensor model to describe the suspension microstructure. By directly studying data from Dr. Mari's particle simulations, we find that the second-order spherical harmonic expansion of the distribution of near-contact orientations, in terms of which the fabric tensor can be defined, captures the distribution poorly at early strains after reversal, while the fourth-order term dominates during these early strains, and retains a significant size up to steady state. A description involving tensors related to both the second- and fourth-order spherical harmonic expansion terms may thus prove more successful at modelling the microstructural evolution of suspensions.

1.1.5 Ch. 6: Ageing in a frictionless soft suspension

Having up to this point considered hard particle suspensions under shear, we switch tack in Ch. 6 and consider a frictionless soft non-Brownian suspension at a volume fraction high enough that the system cannot relax into a state without particle overlaps. Suspensions of this type, such as foams, exhibit interesting dynamics under shear or at finite temperature, such as slow "glassy" relaxation and localised plastic deformations. The dynamics of a quiescent soft suspension relaxing towards its local equilibrium have not been previously reported, having presumably been assumed trivial.

In Ch. 6, we perform such a study, quenching a soft suspension from a highly colloidal to an athermal state. We find slow power-law relaxations of quantities such as the mean squared speed, as well as evidence of coarsening as the system relaxes. Finally, we also see displacement fields around plastic events suggestive of the quadrupolar displacements seen in thermal or sheared systems, though we are unable to isolate any quadrupoles. We thus demonstrate that the dynamics of a relaxing quiescent soft suspension can be unexpectedly interesting.

1.1.6 Ch. 7: Conclusions

Finally, in Ch. 7 we summarise the results of the previous chapters, and the overall conclusions that can be drawn with respect to the themes of the thesis, namely the usefulness of the study of athermal systems and the application of particle simulations in probing the physics of suspensions. We also give an outlook on possible directions for future work suggested by these chapters.

1.2 A note on notation

In this thesis, symbols denoting vectors or tensors, such as the position vector $\boldsymbol{r}$ or the stress tensor $\boldsymbol{\Sigma}$, are written in bold. Scalars, such as the volume fraction ϕ, are not. Given a bold symbol representing a vector, such as $\boldsymbol{r}$, the corresponding non-bold symbol, in the absence of a sub- or superscript specifying a component, denotes its magnitude, i.e. $r := |\boldsymbol{r}|$. Furthermore, given positions $\boldsymbol{r}_i$ and $\boldsymbol{r}_j$ of particles i and j, we use the shorthand $\boldsymbol{r}_{ij} := \boldsymbol{r}_j - \boldsymbol{r}_i$, with the relative velocity $\boldsymbol{v}_{ij}$ defined similarly. The force on particle i due to particle j is denoted $\boldsymbol{F}_{ij}$. Adjacent vectors or tensors, such as $\boldsymbol{pppp}$ for a unit vector $\boldsymbol{p}$, denote a dyadic product, so $(\boldsymbol{pppp})_{ijkl} = p_i p_j p_k p_l$. Contractions over indices are indicated using dots, so e.g. $\boldsymbol{Q} \cdot \boldsymbol{D}$ contracts over the last index of $\boldsymbol{Q}$ and the first of $\boldsymbol{D}$, while $\langle \boldsymbol{pppp} \rangle : \boldsymbol{D}$ contracts over the last two indices of $\langle \boldsymbol{pppp} \rangle$ and the first two of $\boldsymbol{D}$. We also note that this thesis adopts the column-vector convention, so that $(\nabla \boldsymbol{v})_{ij} \equiv \partial_j v_i$. Finally, given a function $f(\boldsymbol{r}, \boldsymbol{s})$ of position $\boldsymbol{r}$ and some vector quantity $\boldsymbol{s} = (s_1, s_2, \ldots, s_d)$, we write $\nabla_{\boldsymbol{s}} f := (\partial_{s_1} f, \partial_{s_2} f, \ldots, \partial_{s_d} f)$.

Chapter 2

Background

2.1 Coarse-graining

When describing the material properties of a macroscopic fluid, it is convenient to adopt the continuum hypothesis [28]. Here, the value of a material quantity, such as the density ρ, at a point $\boldsymbol{r}$ in space (in a given coordinate system) is defined as an average over (effectively) a small volume [29], over a time interval [30] or over ensembles of particle configurations [31], in a process known as coarse-graining. Each approach to coarse-graining has its own advantages, and all three will be used at some point in this thesis as demanded by the situation when discussing continuum models of suspensions and calculating averaged quantities from particle simulation data. We will mainly adopt the first convention, treating the suspension as one continuous material consisting of volume elements, as illustrated for a two-dimensional suspension in Fig. 2.1. Each volume element must be small enough that coarse-grained quantities are approximately constant on their length scale, but consist of many constituents, so that small-scale fluctuations (noise) are small.

Sometimes, there are too few constituents (particles, or "events" such as the formation of a contact between particles) to avoid noise, given volume elements of a desired size. In homogeneous systems, we can address this by averaging each volume element over an ensemble: the coarse-grained value of e.g. the velocity at a box centred at $\boldsymbol{r}$ at time t is obtained by averaging over all particles within the box at time t for multiple different choices of initial condition consistent with the

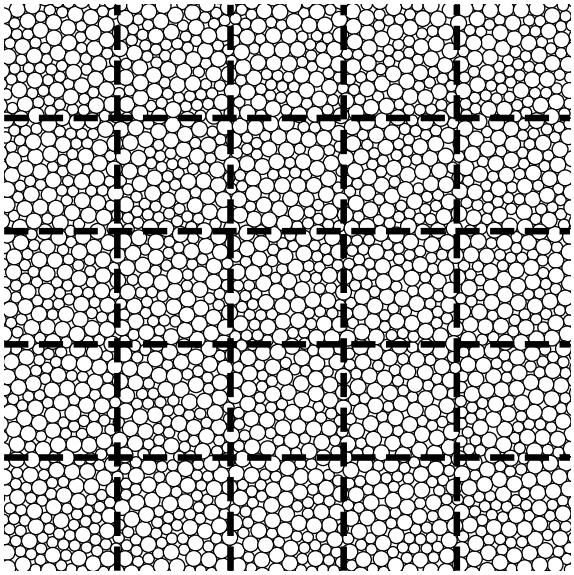

Figure 2.1: Illustration of coarse-graining over a volume, in which space is divided up into volume elements—boxes bounded by dashed lines. One might obtain, for instance, a coarse-grained velocity at the centre of a box by taking the average velocity of all particles within the box.

macroscopic state of the system at the initial time. Similarly, we will, in the course of this thesis, need to average over events that occur at discrete points in time. We must then average over a finite time interval in order to obtain enough events per volume element to reduce the noise to acceptable limits. Fig. 2.2 illustrates these two additional approaches to coarse-graining.

2.2 The Navier-Stokes equations

To model the dynamics of our fluid, we apply the laws of classical mechanics. The assumption of incompressibility and Newton's 2nd law lead, respectively, to the equations [28]

$$\begin{aligned} \nabla \cdot \boldsymbol{v} &= 0, \\ \rho \left[\frac{\partial \boldsymbol{v}}{\partial t} + (\boldsymbol{v} \cdot \nabla) \boldsymbol{v} \right] &= \nabla \cdot \boldsymbol{\Sigma} + \boldsymbol{f}, \end{aligned} \tag{2.2.1}$$

where ρ is the local density of the fluid, and $\boldsymbol{v}$ is the local velocity. External forces (e.g. gravity) per unit volume are included via the variable $\boldsymbol{f}$. The suspensions

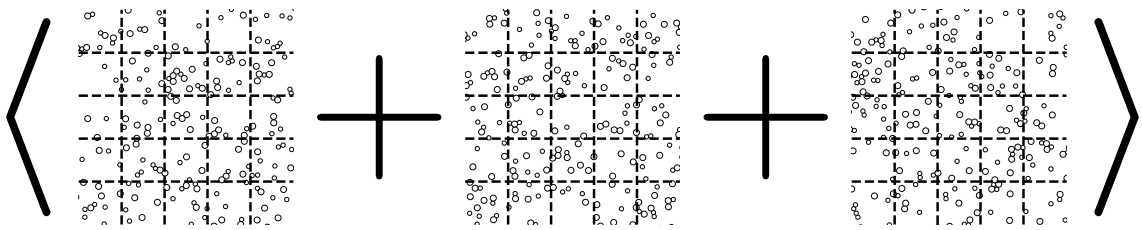

Figure 2.2: Illustration of coarse-graining over ensembles or a period of time. The three grids correspond to the same volume elements at different times, or the same time but a different initial condition. The coarse-grained value of a quantity in a volume element is averaged over particles in that volume element in all three grids.

we study in this thesis are density-matched and have no other external forces, so $\boldsymbol{f} \equiv 0$ in our case. To model internal forces, we define the stress tensor $\boldsymbol{\Sigma}$, which represents the forces acting on a volume element by contiguous volume elements, such as momentum exchange between particles at the boundaries of the elements. The stress tensor is a second-rank tensor which, when contracted with a unit vector $\boldsymbol{n}$ yields the force per unit area acting on a surface element (of a volume element) with outward normal $\boldsymbol{n}$. Splitting the stress tensor into its isotropic and traceless parts, $\boldsymbol{\Sigma} = -p\boldsymbol{I} + \boldsymbol{\Sigma}'$, we call p the pressure and $\boldsymbol{\Sigma}'$ the deviatoric stress. When $\boldsymbol{\Sigma}'$ is of the particularly simple form $\boldsymbol{\Sigma}' = \eta\left(\nabla\boldsymbol{v} + \nabla\boldsymbol{v}^{\mathrm{T}}\right)$, we say the fluid is Newtonian and call η the viscosity. Eqs. 2.2.1 are then known as the Navier-Stokes equations.

A few dimensionless quantities are particularly important when determining what contributions to the motion of a suspension need to be considered [25]. A simple shear flow is one in which the velocity field can be written $\boldsymbol{v} = (\dot{\gamma}y, 0, 0)$ in some inertial frame, as illustrated in Fig. 2.3. We can then define the Péclet number, $\mathrm{Pe} \equiv 6\pi\eta_{\mathrm{f}}\dot{\gamma}a^3/k_{\mathrm{B}}T$, where η_{f} is the viscosity of the suspending fluid, a is the particle diameter, k_{B} is the Boltzmann constant and T is the suspension temperature. This characterises the relative importance of the shear rate $\dot{\gamma}$ and of Brownian motion. Thus, in our athermal case, we are in the limit $\mathrm{Pe} \longrightarrow \infty$. Other dimensionless numbers describe the relative sizes of different terms in Eq. 2.2.1 with respect to one another. One important example is the Stokes number, $\mathrm{St} \equiv \rho\dot{\gamma}a^2/\eta_{\mathrm{f}} \sim \rho\partial_t\boldsymbol{v}/\left(\nabla\cdot\boldsymbol{\Sigma}\right)$, where ρ is the particle-phase density, which, due to density matching, is also that of the bulk suspension. For our μm-sized particles, in typical experimental set-ups

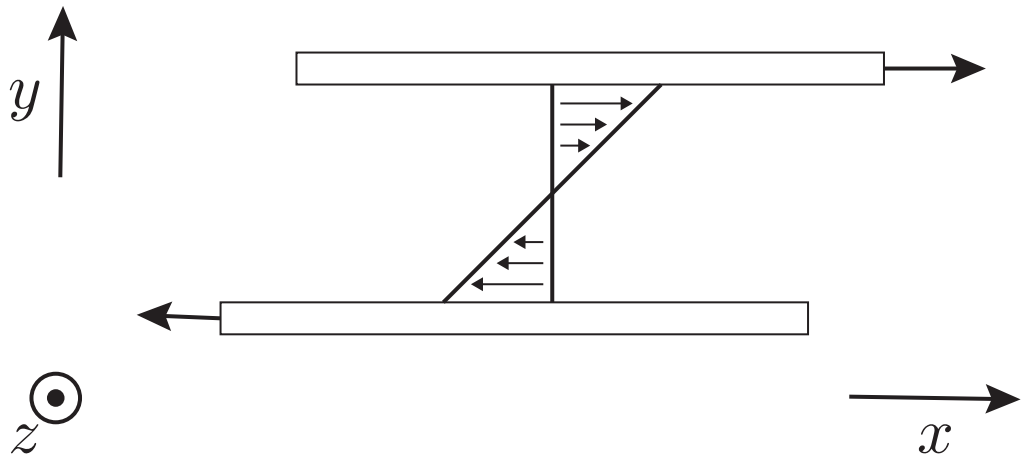

Figure 2.3: A simple shear flow $\boldsymbol{v} = (\dot{\gamma} y, 0, 0)$ imposed by moving walls.

(see §2.6), this is approximately zero, except at very large shear rates. The Reynolds number $\mathrm{Re} \equiv \rho a^2 \dot{\gamma} / \eta_{\mathrm{f}} \sim \rho \left(\boldsymbol{v} \cdot \nabla \right) \boldsymbol{v} / \left(\nabla \cdot \boldsymbol{\Sigma} \right)$, where ρ is the bulk suspension density, is another important example. This too, thanks to the small size of particles in the suspension and large fluid viscosities, is approximately zero in most regimes we consider.

2.3 The Stokes equations

Taking the limits $\mathrm{Re} \longrightarrow 0$ and $\mathrm{St} \longrightarrow 0$ in Eq. 2.2.1, we arrive at the Stokes equations

$$\begin{aligned} \nabla \cdot \boldsymbol{v} &= 0, \\ \nabla \cdot \boldsymbol{\Sigma} + \boldsymbol{f} &= \boldsymbol{0}. \end{aligned} \tag{2.3.2}$$

Given a model for the evolution of $\boldsymbol{\Sigma}$ in flow, called a constitutive model, and a set of initial and boundary conditions, we can solve Eqs. 2.3.2 for the unknowns $\boldsymbol{v}$ and $\boldsymbol{\Sigma}$ [32].

We now consider Stokes flow of a Newtonian fluid in which hard particles are suspended. In a Newtonian fluid, the Stokes equations are linear and homogeneous. The flow is therefore time-reversible, with consequences such as symmetry in the approach and retreat trajectories of particle pairs [25]. Frankel and Acrivos [33] calculated the hydrodynamic interactions between particles of radius a moving relative

to one another with relative speed $u_\perp$ along the line of the particles' centres and $u_\parallel$ in the tangent plane, in the limit of vanishing separation h. They found that the force along the particle centres is

$$F_\perp \sim \frac{3}{2}\pi a \eta u_\perp \frac{2a}{h}, \tag{2.3.3}$$

while the tangential force is

$$F_\parallel \sim 2\pi\eta u_\parallel a \log\left(\frac{2a}{h}\right). \tag{2.3.4}$$

One can then add these pairwise hydrodynamic forces, called lubrication forces, to the Stokes drag $\boldsymbol{F}^{\text{Stokes}} = 6\pi\eta a\boldsymbol{u}$ on particles with velocity $\boldsymbol{u}$ relative to the imposed background flow field, to obtain an approximate total hydrodynamic force $\boldsymbol{F}^{\text{H}}$ on each particle. At high volume fractions, such as those we will consider in this thesis, lubrication forces are the dominant hydrodynamic interactions [34], so this approximation should hold. Linearity of the Stokes equation implies that these forces are linear in the particle velocities and angular velocities. Furthermore, the Stokes equation requires the sum of all forces on each particle to vanish. So long as non-hydrodynamic forces do not break the linearity with respect to relative velocity and angular velocity, this then yields a linear system of equations which can be solved to obtain the velocities and angular velocities of each particle [35]. Pairwise non-hydrodynamic forces $\boldsymbol{F}_{ij}^{\text{NH}}$ on particle i due to particle j contribute a stress $\boldsymbol{S}_{ij}^{\text{NH}} = \boldsymbol{r}_{ij}\boldsymbol{F}_{ij}^{\text{NH}}$ to the system, where $\boldsymbol{r}_{ij}$ is the position of particle j relative to that of particle i. The calculation of the hydrodynamic contribution to the stress is more complicated; the details can be found in Appendix A of [36].

Beyond simplifying Eq. 2.2.1, taking the limit of no inertia has one other important consequence: frame indifference. This is the constraint that non-inertial systems must be invariant under time-dependent rigid rotations. One important consequence of this is that any function F of the flow gradient $\nabla\boldsymbol{v}$ and a second-order tensor $\boldsymbol{T}$ must be of the form [37]

$$F\left(\nabla v, \boldsymbol{T}\right) = \boldsymbol{\Omega}\cdot\boldsymbol{T} - \boldsymbol{T}\cdot\boldsymbol{\Omega} + \tilde{F}\left(\boldsymbol{D}, \boldsymbol{T}\right), \tag{2.3.5}$$

where $\boldsymbol{D}$ and $\boldsymbol{\Omega}$ are the symmetric and anti-symmetric parts of $\nabla\boldsymbol{v}$ respectively, and $\tilde{F}$ corresponds to F in a frame in which $\boldsymbol{\Omega} \equiv \boldsymbol{0}$.

2.4 Critical Load Model

In much of this thesis, we will be discussing data from particle simulations, provided by Dr. Mari, that use the lubrication approach described in the previous section with one caveat [36]. This is due to work by Ball and Melrose [38] which showed that particles in dense suspensions under an imposed shear flow get sufficiently close for the continuum approximation to break down, and for something akin to solid contact between particles to emerge. To account for this possibility given the divergence of lubrication forces as $h \longrightarrow 0$, Dr. Mari's simulations introduce a regularisation length $\delta/(a_1 + a_2)$ which is added to the non-dimensionalised gap $h/(a_1 + a_2)$ when calculating lubrication interactions [39]. Dr. Mari's simulations also cut off the lubrication interactions above an interparticle gap $h/(a_1 + a_2) > 0.2$ since these are small, and since the lubrication approximation is only valid at small gap sizes. Doing so also means $\sim N$ interactions need to be considered, rather than $\sim N^2$, given a system of N particles at a set volume fraction.

Dr. Mari's simulations employ a model for contact friction adopted from granular physics [40, 41], described in detail in [36], which enforce Coulomb's law

$$\left|\boldsymbol{F}_{\parallel}^{\mathrm{C}}\right| \leq \mu \left|\boldsymbol{F}_{\perp}^{\mathrm{C}}\right| . \tag{2.4.6}$$

Here, $\boldsymbol{F}_{\perp}^{\mathrm{C}}$ is the component of the contact force between two particles in contact along their centre-to-centre vector, $\boldsymbol{F}_{\parallel}^{\mathrm{C}}$ is the component in their mutual tangent plane, and μ is the Coulomb friction coefficient. The simulations model short-ranged repulsive forces preventing contact between particles at low stresses using the Critical Load Model [36] (CLM) for the behaviour of μ: μ vanishes below a critical value F_* of $\left|\boldsymbol{F}_{\perp}^{\mathrm{C}}\right|$, and takes a constant value above it. This makes it convenient for describing the "frictional state" of a suspension, a concept that will be needed in Ch. 3, since it can in this case be defined as the fraction of particles in contact that interact with a non-zero μ. We can also study a system without short-ranged repulsive interactions between particles, as will be considered in Chs. 4 and 5 in the context of the CLM by taking $F_* \equiv 0$.

2.5 Jamming

At high concentrations of particles, it can become impossible for particles to flow past one another without deforming. The suspension behaves like a solid, with non-zero bulk and shear elastic moduli, and is said to be jammed [42]. The transition is characterised by critical behaviour on either side of ϕ_{J}, despite the absence of any obvious structural change in the amorphous system. As ϕ_{J} is approached from below, for instance, the shear viscosity diverges with a power law $\eta \sim (\phi_{\mathrm{J}} - \phi)^{-\nu}$ [21, 36]. O'Hern *et al.* [42] also report power-law behaviour in a number of quantities in a granular system of frictionless spheres without interstitial fluid and at local equilibrium as ϕ_{J} is approached from above.

The volume fraction, ϕ_{J}, at which this fluid-to-solid transition occurs is not unique, but rather depends on the details of the suspension as well as the preparation protocol of the jammed configuration. For instance, a protocol in which a granular system of hard spheres is equilibrated at an initial volume fraction $\phi_0 < \phi_{\mathrm{J}}$ before being expanded at high rate until expansion is no longer possible yields a ϕ_0-dependent continuous range of ϕ_{J} in the thermodynamic limit [43]. Equilibrating a three-dimensional system of monodisperse soft spheres at infinite temperature before quenching to $T = 0$ yields the value $\phi_{\mathrm{J}} \approx 0.64$ in the thermodynamic limit, consistent with historical measurements of "random close packing", ϕ_{RCP} [44].

As suggested by the example of an Apollonian packing [45], polydispersity allows for higher jamming fractions, with small spheres able to fit into volumes excluded to larger spheres. The jamming volume fractions of a polydisperse system of hard frictionless spheres is in general affected by the shape of the distribution of particle radii, and not just its width [46]. In order to avoid crystallisation, we will in this thesis consider bidisperse systems in two and three dimensions, with large particles of radius 1.4 times that of the small particles. We will consider systems in which small and large particles are equally numerous, as well as systems in which their total volumes are approximately equal. While jamming fractions of frictionless spheres are preparation protocol-dependent, it is useful to state values for them as a rough guide to where the jamming point is located. We thus list literature values for these jamming points in Table 2.5.

	equal volume	equal population
$d = 2$	–	0.842 [47]
$d = 3$	0.66 [36]	0.646 [derived from Fig. 8 of [47]]

Table 2.1: Literature values for random close packing from the literature for bidisperse systems with size ratio 1:1.4 in two and three dimensions at equal number and equal volume, where such values could be found.

Systems of frictional spheres jam at lower volume fractions [36]. This is best understood by counting the constraints required to jam a system of particles. In a frictionless system, each contact contributes one constraint to the motion of particles in the system. Writing Z for the coordination number, or mean number of contacts per particle, this translates to $NZ/2$ constraints for a system of N particles. In d dimensions, there are dN degrees of freedom, so that providing at least one constraint per degree of freedom means $Z \geq 2d$, with $Z \approx 2d$ at the jamming threshold, excluding rattlers—particles that have space to move around within a cage of jammed neighbours (see Fig. 2.4). (Strictly speaking, additional contacts are required in order to obtain finite bulk and shear moduli in a finite system [48], but this result holds true in the thermodynamic limit.) Friction additionally constrains motion tangential to the contact orientation, so that systems of frictional particles can jam at lower coordination numbers (see Fig. 2.4), which in turn increases the number of configurations at lower volume fractions that are jammed.

2.6 Experimental shear flows

Rheology is the term used to refer to the behaviour of fluids under flow, as well as the study of this behaviour. The only flows we shall study in this thesis are simple shear flows of periodic systems. However, such flows are not experimentally possible. Rheologists instead have a variety of types of rheometer which can impose an approximate shear flow. These can record components of the stress response of the material to an imposed shear rate, or, conversely, the shear rate signal resulting from an imposed shear stress. In the remainder of this section, we assume a homogeneous

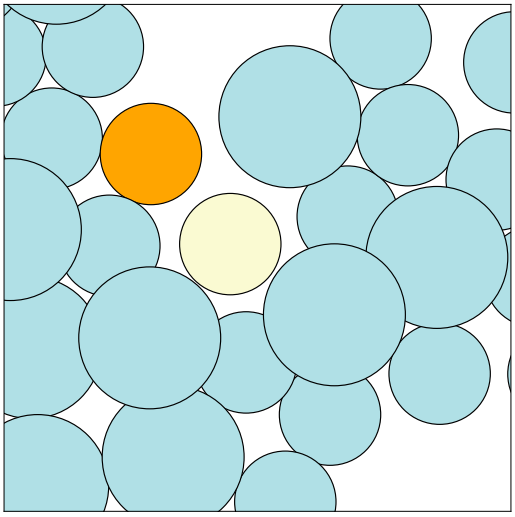

Figure 2.4: A collection of elastic particles. The pale yellow (pale grey) particle is a rattler: it is underconstrained and able to move at no energy cost. The orange (dark grey) particle is underconstrained in a frictionless system, but unable to move in the limit of infinite friction. This illustrates the mechanism by which friction can lead to jamming at lower coordination numbers, and hence volume fractions, than in frictionless systems.

system without wall slip.

Experimental geometries related to simple shear flow include the plate-plate geometry, in which the material is sheared between a stationary base and a rotating disc separated by a gap h, as shown in Fig. 2.5, left. Adopting cylindrical coordinates centred on the axis of rotation of the upper plate, this imposes a flow field $\boldsymbol{v} = \frac{r\omega z}{h}\hat{\boldsymbol{\theta}}$, where ω is the angular velocity of the rotating plate. This corresponds to a radially-varying shear rate $\dot{\gamma} = r\omega/h$. By measuring the forces on the upper plate, rheologists are able to measure the shear stress $\Sigma_{\theta z}$ and the normal stress difference $\Sigma_{\theta\theta} - \Sigma_{rr}$ [49, 50], where $\boldsymbol{\Sigma}$ is the total stress of the sheared material.

The cone-plate geometry, in which the rotating disc of a plate-plate rheometer is replaced by a cone pointing into the material (Fig. 2.5, centre), provides a better approximation of a simple shear flow, imposing a velocity field $\boldsymbol{v} = \frac{r\omega z}{\delta + r\sin\varphi}\hat{\boldsymbol{\theta}}$, where φ is the angle between the cone and the base, and δ is the minimum gap size. This corresponds to a uniform shear rate $\dot{\gamma} = \omega/\sin\varphi$ in the limit of vanishing δ. The forces on the cone yield in this case shear stress $\Sigma_{\theta z}$ and the normal stress difference

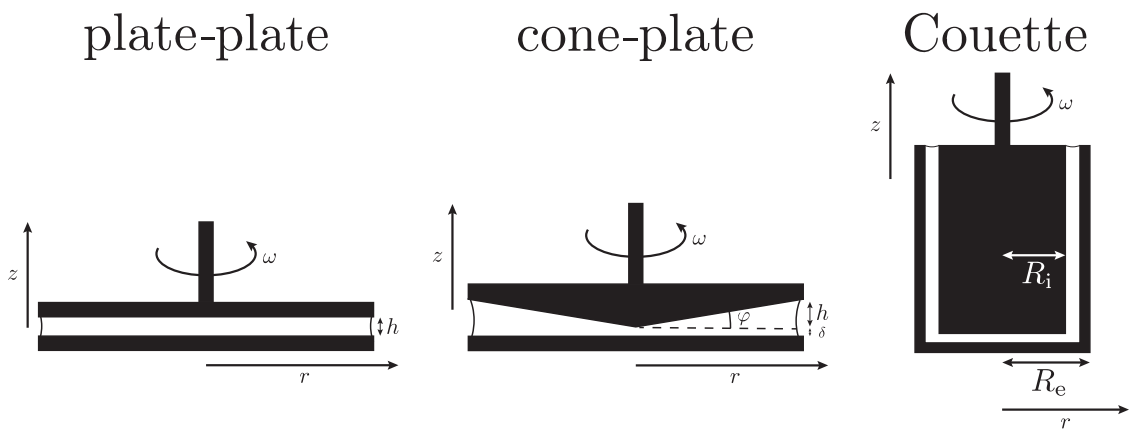

Figure 2.5: Diagrams illustrating three common experimental geometries that approximate a simple shear flow.

$\Sigma_{\theta\theta} - \Sigma_{zz}$ [49, 50].

The Couette cell provides a third common example of an experimental shearing geometry. Here, the material is placed in between two concentric cylinders, with the inner cylinder of radius R_i rotated while the external cylinder of radius R_e is fixed, as shown in Fig. 2.5, right. The resulting flow is $\boldsymbol{v} = \frac{R_\mathrm{e}^2 R_\mathrm{i}}{R_\mathrm{e}^2 - R_\mathrm{i}^2}\left(\frac{R_\mathrm{i}}{r} - \frac{R_\mathrm{i} r}{R_\mathrm{e}^2}\right)\omega\hat{\boldsymbol{\theta}}$ [49], approximating a shear rate $\omega(R_\mathrm{i}^2 R_\mathrm{e}^2)/(R_\mathrm{e}^2 - R_\mathrm{i}^2)$ for $R_\mathrm{e} - R_\mathrm{i} \ll R_\mathrm{i}$. This time, the rheometer measures only the shear stress $\Sigma_{r\theta}$ [50].

Chapter 3

Vorticity banding in dense suspensions

3.1 Introduction

A demonstration sometimes seen at scientific outreach events involves filling a large container with a dense suspension of cornstarch in water and having volunteers run across it [5, 51]. That these volunteers don't simply sink into the fluid (so long as they are running) is a consequence of shear thickening [6, 14, 51]. This is a phenomenon in which the steady-state viscosity of a fluid under shear increases with increasing shear rate $\dot{\gamma}$. One may distinguish three different kinds of shear thickening, seen at different volume fractions ϕ. At lower volume fractions (e.g. $0.4 \lesssim \phi \lesssim 0.55$ [6,36,52,53]), one typically finds continuous shear thickening (CST), in which the viscosity increase is gradual. Discontinuous shear thickening (DST), in which viscosity undergoes a discontinuous jump as shear rate is increased, is found in a narrow band above this range (e.g $0.55 \lesssim \phi \lesssim 0.58$ [6,36,52,53]). Finally, at higher volume fractions (e.g. $0.58 \lesssim \phi \lesssim \phi_{\mathrm{RCP}} \approx 0.64$ [36, 52]) and high enough stress, the suspension may solidify after a finite strain [54], a phenomenon known as shear jamming (SJ). General shear-thickening systems may have complicated constitutive behaviour, with both shear thinning and shear thickening regimes [51, 55], but this chapter will consider the simplest case, in which the system is Newtonian at low and high stresses. Fig. 3.1 shows representative examples of flow curves for a strain-rate

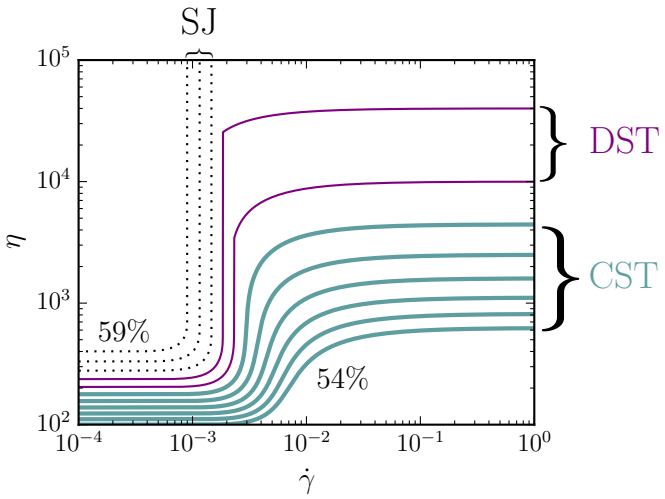

Figure 3.1: Representative flow curves of viscosity η against shear rate $\dot{\gamma}$ for an upward sweep in shear rate of a Wyart-Cates model fluid (evolving Eqs. 3.2.1 to steady-state in homogeneous shear flow, using $\phi_{\mathrm{J}}^{\mu} = 0.58$ and $\phi_{\mathrm{J}}^{0} = 0.64$) at volume fractions $\phi = 0.540, 0.545, \ldots, 0.590$. These contain examples of continuous shear thickening (thick blue curves), discontinuous shear thickening (thin purple curves) and shear jamming (dotted black curves).

controlled experiment.

A number of mechanisms have been proposed to explain these phenomena [5, 51, 56]. In some systems, shear thickening is seen to coincide with a transition from an ordered to a disordered state [57–59]. However, such a transition is absent in other shear thickening systems [60, 61], ruling it out as a generic mechanism for thickening. An alternative physical picture is prompted by experimental [60–62] and simulation [63, 64] studies of dense colloids under shear, which find that shear thickening coincides with the formation of "hydroclusters": transient, high-concentration aggregates of particles. In this picture, shear thickening is a result of large lubrication forces within these clusters [5], which can form at high imposed stress but are broken up by Brownian motion at low stress. This is, however, inconsistent with the zero strain-rate at finite stress seen in shear jammed systems, and simulations based on it have not shown this mechanism to yield the orders-of-magnitude viscosity increases seen in DST [51]. Dilatancy—the tendency of systems of particles to spread out when under shear so that particles can flow past one another—provides a third

explanation [6, 65–69]. This, however, predicts thickening in attractive systems, which are not found to exhibit shear thickening when the attraction is large [70–72], as well as in frictionless suspensions with hard particle-particle interactions, which are constrained by dimensional analysis to being Newtonian at fixed ϕ [21].

One theory that has a growing body of supporting evidence [36, 39, 52, 69, 73–83] explains shear thickening as a consequence of repulsive interparticle forces that prevent contact between particles at low stress but are overcome at high stress. These forces are sometimes introduced as a means of stabilising suspensions which would otherwise flocculate [78, 79, 83, 84], or are naturally present (e.g. in cornstarch [79]). As stronger flows are imposed, pairs of particles are able to overcome their mutual repulsion, and the rheology evolves from one of frictionless spheres to one of frictional particles in contact. (Though lubrication forces between particles diverge at vanishing interparticle separation [14, 25], Ball and Melrose [38] show that sheared systems of particles come within ångströms of contact, at which length scale the continuum approximation would not be expected to work.) These systems have different critical volume fractions, ϕ_{J}, at which their viscosities diverge due to particles no longer being able to slide past one another [36, 85, 86]. Given a scaling law for the divergence of this viscosity as $\phi \longrightarrow \phi_{\mathrm{J}}$, Wyart and Cates [56] showed that interpolating ϕ_{J} between its frictionless value, ϕ_{J}^{0}, and its lower, frictional value, ϕ_{J}^{μ}, with an interpolation parameter increasing sigmoidally with stress, leads to a transition from Newtonian curves at the $\phi \longrightarrow 0$ limit, to increasingly (continuously) shear thickening curves as ϕ is increased. Above a critical volume fraction ϕ_* less than but close to ϕ_{J}^{μ}, the constitutive curves for shear stress against strain rate become S-shaped (see Fig. 3.2). Increasing $\dot{\gamma}$ from zero will then eventually require a homogeneous system to discontinuously transition from the lower positively-sloped branch of the curve to the upper one [56, 68, 74]. Additionally, when $\phi_{\mathrm{J}}^{\mu} < \phi < \phi_{\mathrm{J}}^{0}$, the curves collapse onto the line $\dot{\gamma} = 0$ for Σ above a finite value Σ_{J}, meaning that flow is no longer possible above this stress. The theory thus explains CST, DST and SJ. Examples of the constitutive curves proposed by Wyart-Cates theory are shown in Fig. 3.3 (black curves), with CST for $\phi < 0.57$, DST for $0.57 \leq \phi < 0.58$ and SJ for $\phi > 0.58$ ($\phi = 0.58$ is a special case corresponding to SJ with $\Sigma_{\mathrm{J}} = \infty$).

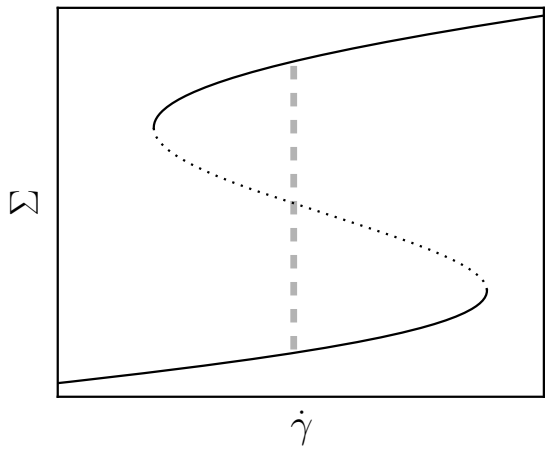

Figure 3.2: Example S-shaped constitutive curve. Solid black: linearly stable region. Dotted black: linearly unstable region. Dashed grey: line at constant shear rate $\dot{\gamma}$. Any such line that crosses the constitutive curve in the unstable region will also cross at two points in stable regions.

The success of Wyart-Cates theory has led to much recent activity uncovering the microscopic physics—particularly the nature of surface-to-surface contacts between particles, and their role in shear thickening [79–82, 87–92]—as well as the macroscopic picture. It is one aspect of this macroscopic picture, concerning the stability of uniform flow [68, 74, 93–98], that this chapter will address. In simple shear, large, homogeneous systems at a negatively-sloped point $\Sigma'(s)/\dot{\gamma}'(s) < 0$ on the constitutive curve $s \mapsto (\Sigma(s), \dot{\gamma}(s))$ of steady-state total shear stress, Σ, against shear rate, $\dot{\gamma}$, are known—for a broad class of constitutive models—to be unstable to small perturbations [99]. These perturbations are sometimes seen to grow into locally-homogeneous regions, or shear bands, parallel to the flow direction. The flow can separate along the flow gradient direction (gradient banding) or the vorticity direction (vorticity banding). The flow curve of steady-state stress against shear rate observed in a stress- or shear rate-controlled experiment or simulation then deviates from the constitutive curve for a system that remains homogeneous. S-shaped constitutive curves are among the two canonical examples of constitutive curves capable of supporting steady vorticity bands identified by Olmsted [100]. In simple shear flow, $\dot{\gamma}$ is imposed by boundary conditions in the flow gradient direc-

tion (e.g. no-slip at walls at $y = \pm L$ travelling at velocity $\boldsymbol{v} = \pm\dot{\gamma}L\hat{\boldsymbol{x}}$). These boundary conditions don't vary along the vorticity axis ($\hat{\boldsymbol{z}}$ in this example), and we therefore expect $\dot{\gamma}$ to also be constant along this axis. Consequently bands should lie on the constitutive curve at the same value of $\dot{\gamma}$. This constraint is compatible with S-shaped constitutive curves: a line of constant $\dot{\gamma}$ that crosses the constitutive curve at a negatively-sloped point will also cross at two positively-sloped points (see Fig. 3.2). A system initially at an unstable point can therefore separate into locally-homogeneous bands at the same $\dot{\gamma}$ but on different stable branches of the constitutive curve. Added to this is a constraint imposed by the Stokes equation requiring the normal vorticity component of the total stress (Σ_{zz} in this example) to be constant [100]. In the case of gradient banding, by contrast, $\dot{\gamma}$ may vary, but the Stokes equation requires both the normal flow gradient component of the total stress and Σ to be constant [100], the latter constraint specifying a unique point on the S-shaped flow curve for any Σ (any horizontal line in Fig. 3.2 will cross the constitutive curve exactly once).

In dense suspensions, this picture is complicated by two factors. The first is concentration coupling: bands may have different volume fractions, and therefore lie on different constitutive curves. This has consequences for flow curves, which would otherwise be expected to be vertical at unstable imposed bulk shear stress $\bar{\Sigma}$, a phenomenon known as shear-rate selection [100, 101]. Instead, concentration-coupled systems are expect to have tilted flow curves [102, 103], since varying $\bar{\Sigma}$ will vary which values of ϕ and hence which constitutive curves the bands sit on. The second factor is the impossibility of static banding, as suggested by Hermes *et al.* [95]: because the solvent phase of a suspension is much more mobile than the solid phase, any gradient in the solvent phase pressure will induce a flow of the solvent phase. Thus, solvent and particle pressures would have to be separately balanced at the interface between two static bands. Hermes *et al.* [95] show that the particle pressure balance condition is essentially impossible to satisfy in a dense suspension, so that banding can't be steady, and must be accompanied by particle migration. Consistent with the suggestion of Hermes *et al.*, experiments on suspensions have revealed an unsteady strain rate signal under conditions of constant imposed macroscopic shear

stress in the DST regime, with complicated time dependence [95–97, 104]. Particle simulations, however, had not previously succeeded in finding flow instabilities in dense suspensions [93].

In this chapter, we introduce a dynamical one-dimensional model allowing for inhomogeneities along the vorticity direction. The model is a generalisation the Wyart-Cates model [56] incorporating a finite response strain for the evolution of the frictional state of a volume element after a change in the local stress as well as a "suspension balance model" [29, 105–108] for particle migration. Through a linear stability analysis, we determine conditions under which homogeneous flow is unstable to arbitrarily small perturbations along the vorticity axis, finding homogeneous flow in an infinite system to be linearly unstable whenever our constitutive curve has negative slope. We then numerically integrate our model, identifying two characteristic long-time inhomogeneous behaviours, which we term "travelling bands" (TBs) and "locally oscillating bands" (LOBs). We also calculate flow curves which capture the maximal extent of the metastability of our TB and SB states. Finally, by choosing parameters predicted by our model to yield unstable flow, Dr. Mari successfully finds TBs and, transiently, LOBs, in a simulated CLM suspension, providing the first observation of unstable flow in a particle simulation of a dense suspension. We compare the TB profiles seen in these particle simulations with those predicted by our model, and explore extensions to our model to see if our fit can be improved. The results in this chapter expand on those published in [98].

3.2 Model

Here and in the rest of this chapter, we assume an imposed velocity field $\bar{\boldsymbol{v}} = (\dot{\gamma} y, 0, 0)$, so that the flow, flow gradient and vorticity directions are $\hat{\boldsymbol{x}}$, $\hat{\boldsymbol{y}}$ and $\hat{\boldsymbol{z}}$ respectively. We only consider variations along $\hat{\boldsymbol{z}}$, adopting the simplifying assumption that fluctuations in particle concentration, stress and velocity gradient along $\hat{\boldsymbol{x}}$ and $\hat{\boldsymbol{y}}$ can be neglected. We take a flow cell of size L along $\hat{\boldsymbol{z}}$, with periodic boundary conditions.

The development of our model begins with that of Wyart and Cates [56]:

$$\Sigma = \eta\dot{\gamma}, \tag{3.2.1a}$$

$$\eta = \begin{cases} \eta_0 \left(\phi_{\mathrm{J}} - \phi\right)^{-2} & \text{if} \quad \phi < \phi_{\mathrm{J}} \\ \infty & \text{otherwise,} \end{cases} \tag{3.2.1b}$$

$$\phi_{\mathrm{J}} = \left(1 - f\right)\phi_{\mathrm{J}}^{0} + f\phi_{\mathrm{J}}^{\mu}, \tag{3.2.1c}$$

$$f = e^{-\Sigma_*/|\Sigma|}. \tag{3.2.1d}$$

Eqs. 3.2.1 represent the Wyart-Cates model broken down into its constituent ingredients. Eq. 3.2.1a is simply the definition of the shear viscosity, η, as the ratio of the (total) shear stress Σ to the shear rate $\dot{\gamma}$. Eq. 3.2.1b describes how this viscosity scales as the volume fraction ϕ approaches a critical value ϕ_{J}, the volume fraction of jamming. Here, η_0 is the power law coefficient for the divergence of the viscosity. This scaling law is based on experiments by Boyer *et al.* [21], who find the same scaling for both η and the ratio of the particle pressure to the shear rate. Eq. 3.2.1c interpolates ϕ_{J} between its frictionless value ϕ_{J}^{0} and its frictional value ϕ_{J}^{μ} using a parameter, f, which represents the frictional state of the system. Finally, Eq. 3.2.1d models the dependence of f on Σ based on a fit to a simulation study of this dependence for the CLM [36], where f is defined as the fraction of contacts for which friction is turned on.

Since we are interested in vorticity-axis physics, our first modification is to model the normal vorticity component of the particle-phase stress, σ_{zz}^{p}, instead of the total shear stress, Σ. To achieve this, we decompose the total stress into a fluid and a particle phase stress. We note that the normal components of the particle-phase stress $\boldsymbol{\sigma}^{\mathrm{p}}$ scale similarly to one another [95] and thus to the particle pressure. This was found by Boyer *et. al* [21] to scale in the same way as Σ, enabling us to take $\Sigma \mapsto |\sigma_{zz}^{\mathrm{p}}|$ and $\dot{\gamma} \mapsto |\dot{\gamma}|$ in Eq. 3.2.1a and so write

$$|\sigma_{zz}^{\mathrm{p}}| = \mu_z^{-1}\eta|\dot{\gamma}|, \tag{3.2.2}$$

with $\mu_z := |\Sigma/\sigma_{zz}^{\mathrm{p}}|$ taken to be constant. For the range of ϕ considered in this chapter, $\mu_z^{-1}\eta_0$ lies within an order of magnitude of the solvent viscosity η_f, and so we simplify our model by taking $\mu_z^{-1}\eta_0 \mapsto \eta_f$.

Our second modification is to add dynamics to the evolution of f. Specifically, we take $f \mapsto f^*$ in Eq. 3.2.1d, with f^* a target value towards which f undergoes a linear relaxation, with relaxation strain γ_0:

$$\partial_t f = -\frac{|\dot{\gamma}|}{\gamma_0}\left[f - f^*\right]. \tag{3.2.3}$$

As well as being a minimal dynamics, this relaxation is consistent with that found in simulations of a homogeneous system [93]. The choice of a relaxation strain, as opposed to a relaxation time, reflects the fact that the dynamics of f relate to the opening and closing of contacts via advection [93].

Our final modification is to allow for concentration flux. We model particle migration using the suspension balance model [29, 105]

$$\nabla \cdot (\phi \boldsymbol{\sigma}^{\mathrm{p}}) + \phi \boldsymbol{F}^{\mathrm{h}} = \boldsymbol{0}, \tag{3.2.4}$$

a two-fluid model [29, 105–108] in which the hydrodynamic drag force per particle phase unit volume, $\phi \boldsymbol{F}^{\mathrm{h}}$, acts like an external force on the particle phase. Using a lubrication approximation for interparticle interactions, the hydrodynamic drag is in general a configuration-dependent linear combination of relative velocities, $\boldsymbol{v}^{\mathrm{p}} - \bar{\boldsymbol{v}}$, relative angular velocities, $\boldsymbol{\omega}^{\mathrm{p}} - \bar{\boldsymbol{\omega}}$, and the symmetrised velocity gradient. We simplify this model considerably, first taking $\nabla \cdot (\phi \boldsymbol{\sigma}^{\mathrm{p}}) \mapsto \phi \nabla \cdot \boldsymbol{\sigma}^{\mathrm{p}}$, and then taking the Stokes drag force per unit volume due to one particle, $\boldsymbol{F}^{\mathrm{h}} = -\zeta\left(\boldsymbol{v}^{\mathrm{p}} - \bar{\boldsymbol{v}}\right)$. Recalling that we are imposing $\bar{v}_z \equiv 0$ and neglecting variations in the $\hat{\boldsymbol{x}}$ and $\hat{\boldsymbol{y}}$ directions, this leaves us with a relation

$$\partial_z \sigma^{\mathrm{p}}_{zz} = \zeta v_z. \tag{3.2.5}$$

Simulations [109] suggest a value for ζ varying with ϕ from $\frac{9}{2}\eta_f a^{-2}$ for $\phi \approx 0$ to $225\eta_f a^{-2}$ when $\phi \approx 0.64$, where η_f is the solvent viscosity and a is the particle radius, but the small (of order 10^{-3}) size of variations in ϕ seen in our study motivates us to adopt the simplification that ζ is a constant. Finally, conservation of particle mass requires that $\partial_t \phi + \nabla \cdot (\phi \boldsymbol{v}^{\mathrm{p}}) = 0$. This suggests a further approximation, similar in nature to our previous one: $\phi \boldsymbol{v}^{\mathrm{p}} \approx \bar{\phi} \boldsymbol{v}^{\mathrm{p}}$. Defining a rescaled drag constant $\alpha := \zeta/\bar{\phi}$, which we take as a model parameter, this gives us

$$\partial_t \phi = -\alpha^{-1} \partial_z^2 \sigma^{\mathrm{p}}_{zz}. \tag{3.2.6}$$

We now non-dimensionalise the model, choosing dimensionless units in which our unit of stress is σ_*, our unit of viscosity is η_f and our unit of length is L. To this end, we define non-dimensional quantities $\tilde{\sigma} := \sigma^{\mathrm{p}}_{zz}/\sigma_*$, $\tilde{\eta} := \eta/\eta_f$, $\tilde{\dot{\gamma}} := \dot{\gamma}/\left(\eta_f^{-1}\sigma_*\right)$, $\tilde{t} := t/\left(\sigma_*^{-1}\eta_f\right)$, $\tilde{z} := z/L$ and $\tilde{\alpha} := \alpha/\left(L^{-2}\eta_f\right)$, where L is the size of our system along $\hat{z}$ and $\sigma_* := \mu_z^{-1}\Sigma_*$. This yields the non-dimensionalised form of the model

$$\partial_{\tilde{t}} f = -\frac{\left|\tilde{\dot{\gamma}}\right|}{\gamma_0}\left[f - e^{-1/|\tilde{\sigma}|}\right], \tag{3.2.7a}$$

$$\partial_{\tilde{t}}\phi = -\tilde{\alpha}^{-1}\partial_{\tilde{z}}^2\tilde{\sigma}, \tag{3.2.7b}$$

$$|\tilde{\sigma}| = \left[(1-f)\,\phi_{\mathrm{J}}^0 + f\phi_{\mathrm{J}}^{\mu} - \phi\right]^{-2}\left|\tilde{\dot{\gamma}}\right|. \tag{3.2.7c}$$

Multiplying both sides of Eqs. 3.2.7a and 3.2.7b by γ_0, changing variable from $\tilde{t}$ to $\tilde{\tilde{t}} := \tilde{t}/\gamma_0$, and changing parameter from $\tilde{\alpha}$ to $\tilde{\tilde{\alpha}} := \tilde{\alpha}/\gamma_0$ has the effect of rescaling the strain $\gamma := |\dot{\gamma}|t$, since $\left|\tilde{\dot{\gamma}}\right|\tilde{\tilde{t}} = \left|\tilde{\dot{\gamma}}\right|\tilde{t}/\gamma_0 = \gamma/\gamma_0$.

For the rest of this chapter, except where explicitly noted, we will simplify our notation, neglecting the tildes above our non-dimensionalised quantities, and the double-tildes above $\tilde{\tilde{t}}$ and $\tilde{\tilde{\alpha}}$. We will also write σ for $|\sigma|$ and $\dot{\gamma}$ for $|\dot{\gamma}|$, leaving us with equations

$$\partial_t f = -\dot{\gamma}\left[f - e^{-1/\sigma}\right], \tag{3.2.8a}$$

$$\partial_t \phi = \alpha^{-1}\partial_z^2\sigma, \tag{3.2.8b}$$

$$\sigma = \eta\dot{\gamma}, \tag{3.2.8c}$$

$$\eta = \left[(1-f)\,\phi_{\mathrm{J}}^0 + f\phi_{\mathrm{J}}^{\mu} - \phi\right]^{-2}, \tag{3.2.8d}$$

$$\dot{\gamma} = \frac{\bar{\sigma}}{\bar{\eta}}, \tag{3.2.8e}$$

where the apparent sign change on the RHS of Eq. 3.2.8b is a consequence of the negative sign of σ^{p}_{zz} in dense suspensions [14]. We set $\phi_{\mathrm{J}}^{\mu} = 0.58$ (corresponding to Coulomb friction with a coefficient $\mu \approx 1$ [21, 36]) and $\phi_{\mathrm{J}}^0 = 0.64$ [44, 110], after which our model has three free parameters: $\bar{\sigma}$, $\bar{\phi}$ and α.

To find vorticity bands, we will consider a stress-controlled protocol in which we impose a volume-averaged stress $\bar{\sigma} := L^{-1}\int_0^L \sigma \mathrm{d}z$ and allow the shear-rate to evolve in response. (A shear rate-controlled system initially at rest would remain on the linearly stable lower branch of the constitutive curve until $\dot{\gamma}$ is raised above

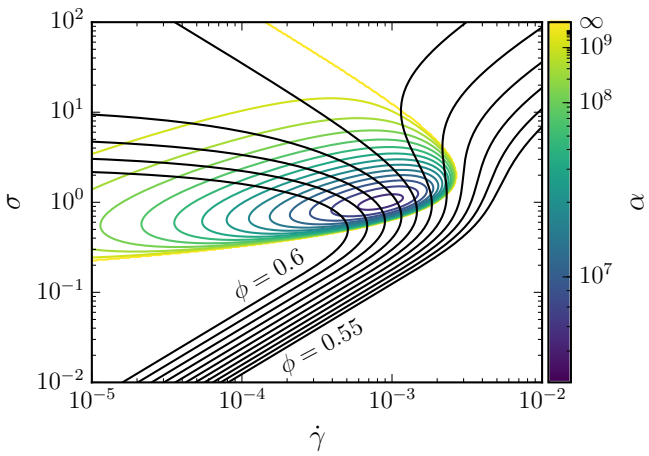

Figure 3.3: Black curves: homogeneous constitutive curves for linearly spaced volume fractions $\phi = 0.550, 0.555, \cdots, 0.600$. These constitutive curves are identical to those of the Wyart-Cates model [56] for particle pressure or shear stress. Coloured curves: Neutral stability contours, surrounding the region in which homogeneous flow is linearly unstable, for linearly spaced $\alpha^{-\frac{1}{2}} = 0.00000, 0.00003, \cdots, 0.00045$.

the maximum shear rate of that branch, at which point the system would jump to the linearly stable upper branch.) We will also impose a volume-averaged volume fraction $\bar{\phi} := L^{-1} \int_0^L \phi \mathrm{d}z$, which will remain constant in time thanks to mass conservation. Writing $\bar{\eta} := L^{-1} \int_0^L \eta \mathrm{d}z$, Eq. 3.2.8c gives us $\dot{\gamma} = \bar{\sigma}/\bar{\eta}$, a consequence of the invariance of $\dot{\gamma}$ along $\hat{\boldsymbol{z}}$.

3.3 Instabilities

3.3.1 Linear stability analysis

A system in an initially homogeneous state is linearly unstable if arbitrarily small spatial perturbations get larger with time. For our simple model, Eqs. 3.2.8, this is something we can determine analytically. We consider an initially steady, homoge-

neous system at imposed bulk stress $\bar{\sigma}$ and bulk volume fraction $\bar{\phi}$, so that

$$\phi = \bar{\phi}, \tag{3.3.9}$$

$$\sigma = \bar{\sigma}, \tag{3.3.10}$$

$$f = e^{-1/\bar{\sigma}}, \tag{3.3.11}$$

$$\dot{\gamma} = \left[\phi_{\mathrm{J}}^{0} - \left(\phi_{\mathrm{J}}^{0} - \phi_{\mathrm{J}}^{\mu}\right) f - \bar{\phi}\right]^{2} \bar{\sigma}. \tag{3.3.12}$$

We then perturb the profiles of our dynamical variables f and ϕ with zero-mean small-amplitude perturbations δf and $\delta\phi$, so that $f = e^{-1/\bar{\sigma}} + \delta f\,(z,t)$ and $\phi = \bar{\phi} + \delta\phi\,(z,t)$. We assume that these perturbations are small enough that we can take the linear-order Taylor expansion of Eqs. 3.2.8a and 3.2.8b about the homogeneous steady state to be exact,

$$\begin{aligned} \partial_t \delta f &= -\dot{\gamma}\delta f + 2\bar{\sigma}^{-\frac{1}{2}}\dot{\gamma}^{\frac{1}{2}} e^{-\bar{\sigma}^{-1}} \left[\left(\phi_{\mathrm{J}}^{0} - \phi_{\mathrm{J}}^{\mu}\right)\delta f + \delta\phi\right], \\ \partial_t \delta\phi &= 2\alpha^{-1}\bar{\sigma}^{\frac{3}{2}}\dot{\gamma}^{-\frac{1}{2}}\partial_z^2 \left[\left(\phi_{\mathrm{J}}^{0} - \phi_{\mathrm{J}}^{\mu}\right)\delta f + \delta\phi\right]. \end{aligned} \tag{3.3.13}$$

This can be solved by taking the Fourier expansions $\delta f = \sum_{k=-\infty}^{\infty} \delta\hat{f}_k\, e^{2\pi i k z}$ and $\delta\phi = \sum_{k=-\infty}^{\infty} \delta\hat{\phi}_k\, e^{2\pi i k z}$, yielding, for each k-mode (except the $k = 0$ mode which vanishes for δf and $\delta\phi$),

$$\partial_t \begin{pmatrix} \delta\hat{f}_k \\ \delta\hat{\phi}_k \end{pmatrix} = \begin{pmatrix} -\dot{\gamma} + 2\left(\phi_{\mathrm{J}}^{0} - \phi_{\mathrm{J}}^{\mu}\right) e^{-\bar{\sigma}^{-1}} \bar{\sigma}^{-\frac{1}{2}}\dot{\gamma}^{\frac{1}{2}} & 2\, e^{-\bar{\sigma}^{-1}} \bar{\sigma}^{-\frac{1}{2}}\dot{\gamma}^{\frac{1}{2}} \\ -8\pi^2 \left(\phi_{\mathrm{J}}^{0} - \phi_{\mathrm{J}}^{\mu}\right) \alpha^{-1}\bar{\sigma}^{\frac{3}{2}}\dot{\gamma}^{-\frac{1}{2}} k^2 & -8\pi^2\alpha^{-1}\bar{\sigma}^{\frac{3}{2}}\dot{\gamma}^{-\frac{1}{2}} k^2 \end{pmatrix} \cdot \begin{pmatrix} \delta\hat{f}_k \\ \delta\hat{\phi}_k \end{pmatrix} \tag{3.3.14}$$

with solution $e^{\boldsymbol{W}_k t} \cdot (\delta\hat{f}_k, \delta\hat{\phi}_k)^{\mathrm{T}}$, where $\boldsymbol{W}_k$ is the matrix in Eq. 3.3.14. We note that the quantisation of the Fourier modes of the perturbations seen here is a consequence of the finite size of our periodic box.

Our perturbation will grow if, for some non-zero k, some eigenvalue of $\boldsymbol{W}_k$ has a positive real part. Being a 2×2 matrix, $\boldsymbol{W}_k$ has eigenvalues $T \pm \sqrt{T^2 - D}$, where $T := \mathrm{Tr}[\boldsymbol{W}_k]/2$ and $D := \det[\boldsymbol{W}_k]$. If $T^2 \leq D$, both eigenvalues have positive real part iff $T > 0$. If $T^2 > D$ and $D > 0$, both eigenvalues will be real, with one being positive and the other negative, iff $T > 0$. Were $D < 0$, we would in principle have two real eigenvalues with opposing sign irrespective of the sign of T. In our case, however, $D = 8\pi^2\alpha^{-1}\bar{\sigma}^{\frac{3}{2}}\dot{\gamma}^{\frac{1}{2}}k^2 > 0$, so the $D < 0$ case does not apply. We thus see that the perturbation will grow iff $T > 0$. Noting that on the

constitutive curve $\dot{\gamma}(\sigma)$ for the unperturbed state with volume fraction ϕ, $-\sigma\frac{\mathrm{d}\dot{\gamma}}{\mathrm{d}\sigma} = -\dot{\gamma} + 2\left(\phi_{\mathrm{J}}^{0} - \phi_{\mathrm{J}}^{\mu}\right)\sigma^{-\frac{1}{2}}\dot{\gamma}^{\frac{1}{2}}e^{-1/\sigma}$, we therefore obtain the instability criterion

$$\frac{\mathrm{d}\dot{\gamma}}{\mathrm{d}\sigma} < -8\pi^{2}\alpha^{-1}\eta^{\frac{1}{2}}k^{2}. \tag{3.3.15}$$

Recalling that α here refers to $\tilde{\tilde{\alpha}} = L^{2}\eta_{f}^{-1}\gamma_{0}^{-1}\bar{\phi}^{-1}\zeta$, we see that the $L \longrightarrow \infty$ limit gives us our usual instability criterion for large systems, $\mathrm{d}\sigma/\mathrm{d}\dot{\gamma} < 0$. The neutral stability contours, corresponding to equality in Eq. 3.3.15 for the most unstable mode, $k = 1$, are shown in Fig. 3.3. These show that, for every S-shaped flow curve, there exists a critical value of α, and hence L, below which no linearly unstable points exist on the curve. This explains the absence of linear instabilities in some previous particle simulation studies [93].

A physical picture of how this instability works can be obtained by initially neglecting variations in ϕ, noting that, as seen on the RHS of Eq. 3.3.15, concentration coupling has a stabilising influence on the dynamics. In this case, Eq. 3.2.8a shows us that a small local increase δf in f will lower the jamming fraction ϕ_{J} at that point, leading to an increase in local viscosity and thus stress, which will in turn increase the target value $f^{*} = e^{-1/\sigma}$ that f is relaxing towards. If the increase in f^{*} caused by the increase in f is larger than δf itself, the rate at which f grows, determined by the now greater distance between f and f^{*}, will increase. Formally, δf evolves at a rate $\partial_{t}\delta f = -\dot{\gamma}\left[\delta f - \frac{\mathrm{d}f^{*}(\sigma(f))}{\mathrm{d}f}\Big|_{f=f^{*}}\delta f\right]$, and so will grow if $\frac{\mathrm{d}f^{*}(\sigma(f))}{\mathrm{d}f}\Big|_{f=f^{*}} > 1$. The connection with the negative-slope criterion for the constitutive curve $\dot{\gamma}(\sigma) = \sigma/\eta(\sigma)$ comes from the fact that the inequality $\mathrm{d}\dot{\gamma}/\mathrm{d}\sigma < 0$ requires the viscosity increase induced by a stress increase to outweigh the stress increase itself, i.e. $\delta\sigma < \dot{\gamma}\frac{\mathrm{d}\eta}{\mathrm{d}\sigma}\delta\sigma$ (since $\frac{a+\alpha}{b+\beta} < \frac{a}{b}$ iff $\frac{\alpha}{\beta} < \frac{a}{b}$, where $b > |\beta| > 0$). As before, the viscosity is increased via an increase in f (noting that $f \equiv f^{*}$ on the constitutive curve), and it is this shared mechanism that yields our criterion, since it means that locally, $\frac{\mathrm{d}f^{*}(\sigma(f))}{\mathrm{d}f}\Big|_{f=f^{*}} = \dot{\gamma}\frac{\mathrm{d}f^{*}(\sigma)}{\mathrm{d}\sigma}\frac{\mathrm{d}\eta(f)}{\mathrm{d}f}\Big|_{f=f^{*}}$ (since $\frac{\mathrm{d}\sigma(\eta)}{\mathrm{d}\eta} = \dot{\gamma}$), while on the constitutive curve, $\dot{\gamma}\frac{\mathrm{d}\eta}{\mathrm{d}\sigma} = \dot{\gamma}\frac{\mathrm{d}\eta(f^{*})}{\mathrm{d}f^{*}}\frac{\mathrm{d}f^{*}(\sigma)}{\mathrm{d}\sigma}$. Negatively-sloped regions on the constitutive curve thus correspond exactly to the regions in which a small increase δf in the local frictional state f is able to create a destabilisingly large increase in the target frictional state f^{*}. The role of the volume fraction dynamics, Eq. 3.2.8b, is then to create a concentration flux in response to spatial variations in σ. This stabilises

the system against inhomogeneities by reducing (increasing) ϕ, and thus the local viscosity, around stress peaks (troughs). This emerges from the fact that, within our model, stress gradients imply particle migration.

At volume fractions $\bar{\phi} > \phi_{\mathrm{J}}^{\mu}$, there is a critical stress $\sigma_{\mathrm{J}} = -1/\log\left(\frac{\phi_{\mathrm{J}}^{0}-\bar{\phi}}{\phi_{\mathrm{J}}^{0}-\phi_{\mathrm{J}}^{\mu}}\right)$ above which the viscosity diverges and the only homogeneous flows possible are ones with vanishing shear rates, i.e. jammed flows. It is not obvious that the previous discussion applies to this regime, so we treat this separately here. We first consider the stability of systems at stresses $\bar{\sigma} \lessapprox \sigma_{\mathrm{J}}$. The slope $\mathrm{d}\sigma/\mathrm{d}\dot{\gamma}$ is discontinuous at σ_{J}, so Eq. 3.3.15 does not immediately imply linear stability. Instead, we use the instability criterion in the form $\mathrm{Tr}[\boldsymbol{W}_k] > 0$, where it is clear that as $\dot{\gamma} \longrightarrow 0$ from above, $\mathrm{Tr}[\boldsymbol{W}_k] \longrightarrow -\infty$ for any mode k. This shows that, for any finite α, the system is linearly stable within some neighbourhood of σ_{J}. Taking $\dot{\gamma} \longrightarrow 0$ in Eq. 3.3.14 also gives us insight into the linear stability of the system for $\bar{\sigma} \geq \sigma_{\mathrm{J}}$. We see that in this limit, perturbations δf neither shrink nor grow, while

$$\delta\phi = -\left(\phi_{\mathrm{J}}^{0} - \phi_{\mathrm{J}}^{\mu}\right)\delta f. \tag{3.3.16}$$

Small perturbations will not change $\bar{\eta}$, and thus $\dot{\gamma}$, up to first order. A small non-zero $\dot{\gamma}$ might, however, be created by higher-order effects, so we must consider whether this would lead to the growth or shrinkage of the otherwise frozen δf. Applying Eq. 3.3.16 to the top row of Eq. 3.3.14 for each mode k, we obtain the result

$$\partial_t \delta f = -\dot{\gamma}\delta f, \tag{3.3.17}$$

allowing us to conclude that the jammed homogeneous state is always linearly stable.

3.3.2 Large-strain behaviour

We numerically solve Eqs. 3.2.8, and report the details of the numerical method in §3.6. Evolving systems whose initial conditions are homogeneous states subject to small perturbations at linearly-unstable points on the constitutive curve leads to the identification of two limiting ($t \longrightarrow \infty$) unsteady behaviours. In the most common case, field-variable profiles consist of pulses of fixed shape travelling at a constant speed c in a given direction (Fig. 3.4, left). We call this a "travelling band"

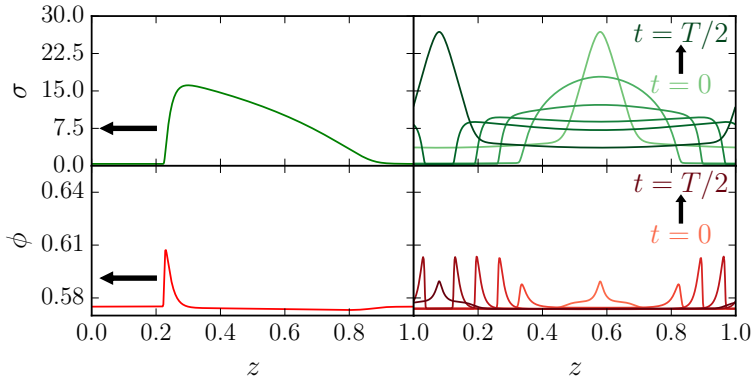

Figure 3.4: Large-strain stress (green) and volume fraction (red) profiles of the model (Eqs. 3.2.8) at $\left(\alpha, \bar{\sigma}, \bar{\phi}\right) = (9 \times 10^8, 3, 0.575)$ (left) and $\left(\alpha, \bar{\sigma}, \bar{\phi}\right) = (9 \times 10^8, 7, 0.575)$ (right). The left-hand plots show a travelling band (TB) state, in which a pulse travels at a constant speed in a spontaneously chosen direction. The right-hand plots show a locally oscillating band (LOB) state, in which two pulses seem to travel in opposite directions, leading to an interference pattern in which a peak oscillates between two points half a box-width apart every $T/2$ time units, where T is the period.

(TB) state. This state necessarily has a steady shear rate, since $\dot{\gamma} = \bar{\sigma} / \int_0^1 \eta \mathrm{d}z$ and the viscosity profile $\eta\left(z\right)$ does not change shape over time. We also characterise a second large-strain behaviour in which profiles correspond to two pulses travelling in opposite directions to one another and interfering, creating a standing pattern with a peak that oscillates between two points half a box-width apart from one another (Fig. 3.4, right). Systems in this second state, which we refer to as a "locally oscillating band" (LOB) state, have an oscillating shear-rate, a behaviour that has also been seen in experiments [95, 96].

TB and LOB states are also usefully characterised by the behaviours of the Fourier modes $\hat{\phi}_k$ and $\hat{f}_k$. In the case of TB states, any scalar field A in our model, such as σ, f or ϕ, will satisfy $A\left(z,t\right) = A\left(z - ct, 0\right)$. This in turn satisfies the transport equation $\partial_t A + c\partial_z A = 0$ and we see that $\hat{A}_k\left(t\right) = \hat{A}\left(0\right) e^{-2\pi i c k t}$, so that $\left|\hat{\phi}_k\right|$ and $\left|\hat{f}_k\right|$ must be constant for each k. For LOB states, by contrast, we find that $\left|\hat{\phi}_k\right|$ and $\left|\hat{f}_k\right|$ oscillate in time, but that $\arg\left(\hat{\phi}_k\right)$ and $\arg\left(\hat{f}_k\right)$ are constant. Of note, too, is that the difference in phase angle between subsequent k-modes is

also constant. By looking at the time-evolution of the amplitudes and phases of the Fourier modes $\hat{\phi}_k$ and $\hat{f}_k$, these characteristics, illustrated in Fig. 3.5, provide a convenient way to determine how close a system is to its limiting TB or SB state.

Choosing a representative $\alpha = 10^9$, we obtain metastable flow curves, shown in Fig. 3.6, for stress sweeps of TB and LOB states at two volume fractions, $\bar{\phi} = 0.575$ and $\bar{\phi} = 0.582$, chosen so as to straddle the frictional jamming fraction $\phi_{\mathrm{J}}^{\mu} = 0.58$. These show that at certain values of the bulk parameters $\bar{\phi}$ and $\bar{\sigma}$, the system is able to support both TB and LOB states, depending on the initial conditions used when evolving Eqs. 3.2.8. To obtain these curves, we start by finding a TB or LOB state with which to begin our sweep. By selecting appropriate values of $\bar{\sigma}$, we are able to do this by perturbing a state on the constitutive curve and evolving it until the dynamic long-time state is reached. Specifically, TB states are found by perturbing the homogeneous systems at $\left(\bar{\phi}, \bar{\sigma}\right) = (0.575, 3)$ and $\left(\bar{\phi}, \bar{\sigma}\right) = (0.582, 3)$, while LOB states are found by perturbing $\left(\bar{\phi}, \bar{\sigma}\right) = (0.575, 7)$ and $\left(\bar{\phi}, \bar{\sigma}\right) = (0.582, 8)$. Starting from a profile obtained in this way, we quasi-statically sweep $\bar{\sigma}$ both up and down from these starting values, waiting at each step for the long-time state to be attained before incrementing the stress again. We characterise the state in Fourier space, as per the previous paragraph. By choosing sufficiently small stress increments, we hope to explore the maximum range in $\bar{\sigma}$ at which TB states and LOB states can exist. The points at which the black and turquoise curves in Fig. 3.6 collapse onto the grey homogeneous curve occur after a stress increment $\Delta\bar{\sigma}/\bar{\sigma} \sim 10^{-2}$, at which point the state was judged to have reached the limit of its metastability range. We do not find any significant differences in the behaviours below and above frictional jamming, in contrast to experiments, which have found chaotic strain-rate dynamics in the $\bar{\phi} > \phi_{\mathrm{J}}^{\mu}$ regime [95].

The profiles of the TB and LOB states, shown in Fig. 3.7, provide some insight into what determines the limits of the metastability ranges for TB and LOB states shown in Fig. 3.6. For TB profiles, we see that the high-stress band widens with increasing $\bar{\sigma}$, with the width of the flat low-stress band almost vanishing at the highest $\bar{\sigma}$ in which TB states are still metastable. At the lowest metastable $\bar{\sigma}$, we see that the high-stress band is becoming narrow. LOB states show similar behaviour,

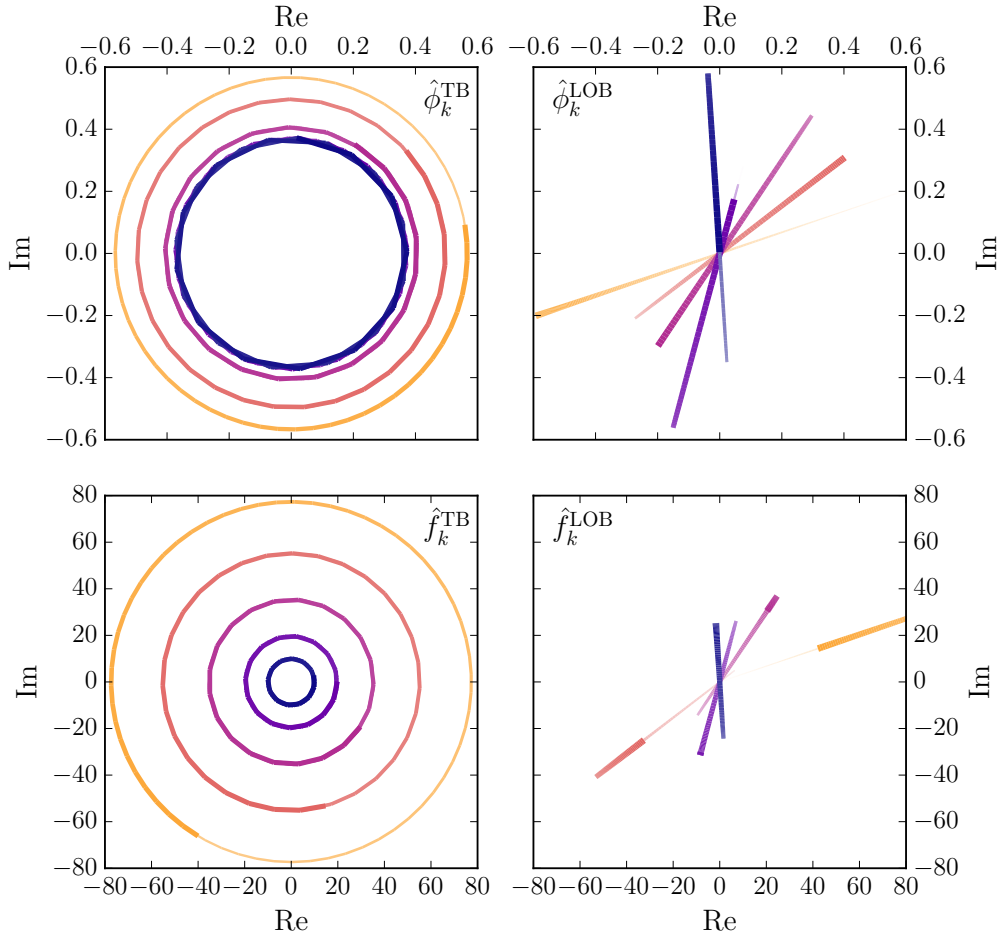

Figure 3.5: Trajectories in the Argand plane of $\hat{\phi}_k$ (top row) and $\hat{f}_k$ (bottom row) for $k = 1, \cdots, 6$ (darker colour denotes higher k) for a TB state (left column) and an LOB state (right column) at the same $\left(\bar{\phi}, \bar{\sigma}\right) = (0.575, 10)$. For a given trajectory, the curve gets thicker and less faded with increasing strain. We see that travelling bands are characterised by Fourier modes that attain a constant amplitude, while locally oscillating bands are characterised by Fourier modes that attain a constant phase.

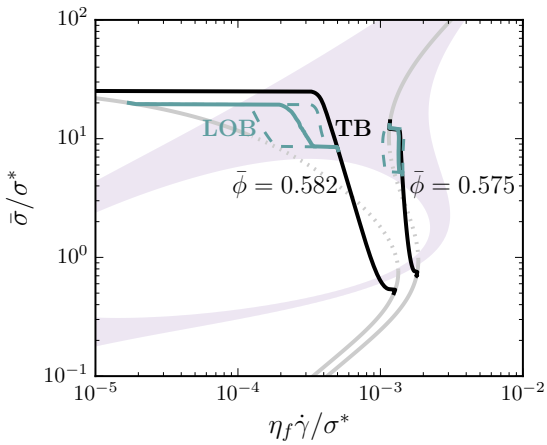

Figure 3.6: Black (blue) curves: metastable flow curves showing the maximum extent in $\bar{\sigma}$ at which the TB (LOB) state can exist for $\alpha = 10^9$ at $\bar{\phi} = 0.575$ and $\bar{\phi} = 0.582$. Solid blue: mean shear rate. Dashed blue: shear rate extrema. Grey curves: the underlying constitutive curves at those volume fractions; dotted sections correspond to linearly unstable regimes. Shaded region: region in which the $k = 1$ mode has eigenvalues with non-vanishing imaginary components.

with vanishing low-stress band widths at shear rate maxima and narrowing high-stress band widths at shear-rate minima. This suggests that band width as a fraction of box size is the constraint that determines the metastability range of both TB and LOB states. We also note that the entire dynamics of the LOB state lies within the region in which the most unstable mode, $k = 1$, has eigenvalues with a non-zero imaginary part, and thus an oscillatory component to the growth of perturbations, which may form an additional constraint for LOB states.

3.4 Comparison with particle simulations

We test the predictions of our model against a particle simulation of 8000 bi-disperse spheres of radius a and $1.4a$, with both species taking up an equal total volume. These are contained within a triperiodic box with size $L_x = 10.2a$ in the x-direction, $L_y = 10.2a$ in the y-direction, and $L_z = 815a$ in the z-direction, so that the bulk volume fraction of particles is $\bar{\phi} = 0.58$. In these simulations, Dr. Mari imposes a simple shear flow using Lees-Edwards periodic boundary conditions [111] and

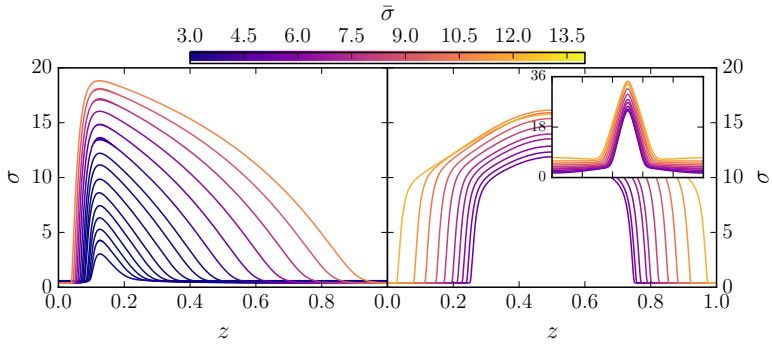

Figure 3.7: Profiles of TB and LOB states on the metastable flow curve at $\bar{\phi}$ shown in Fig. 3.6 for bulk stresses $\bar{\sigma}$ spanning the full metastability range of the given state. Left: TB stress profiles. Right: LOB stress profiles at shear rate minima. Right, inset: LOB stress profiles at shear rate maxima. Lighter colour means a higher imposed $\bar{\sigma}$. [We note that numerical artifacts are evident at the peaks of certain TB profiles, a consequence of the finite size of our grid spacing (c.f. §3.6). These are small enough not to impact our conclusions about the TB profiles, and do not have a noticeable effect on the flow curves in Fig. 3.6.]

control the bulk shear stress $\bar{\Sigma}$. While the model controls for $\bar{\sigma}$ rather than $\bar{\Sigma}$, these behave similarly and so this should not matter. Particles interact through short-ranged lubrication forces as well as contact forces modelled using the Critical Load Model [36], in which contacts are frictionless below a critical normal force F_*, and frictional with coefficient μ above it. The simulations use $\mu = 1$, a value that leads to steady-state homogeneous behaviour consistent with Eq. 3.2.8c for the same choices of $\phi_J^\mu = 0.58$ and $\phi_J^0 = 0.64$ as we use when exploring our model [112]. A regularisation length $\delta = 10^{-3}$ is chosen to cut off the divergence of the lubrication forces between particles (c.f. §2.4). We set $\gamma_0 = 0.023$, based on a simulation study for the stress relaxation of a homogeneous system [93]. Finally, because the particle simulations only consider short-ranged lubrication (c.f. §2.4), the appropriate choice of drag coefficient ζ is that of the dilute limit (i.e. the limit in which many-body hydrodynamics is neglected), $\zeta = \frac{9}{2}\eta_f a^{-2}$. Thus, $\alpha = L^2\eta_f^{-1}\gamma_0^{-1}\bar{\phi}^{-1}\zeta = 1.3 \times 10^8$.

These parameter values are, according to our model, capable of supporting TB and LOB states. Our particle simulations confirm this prediction, finding TBs at

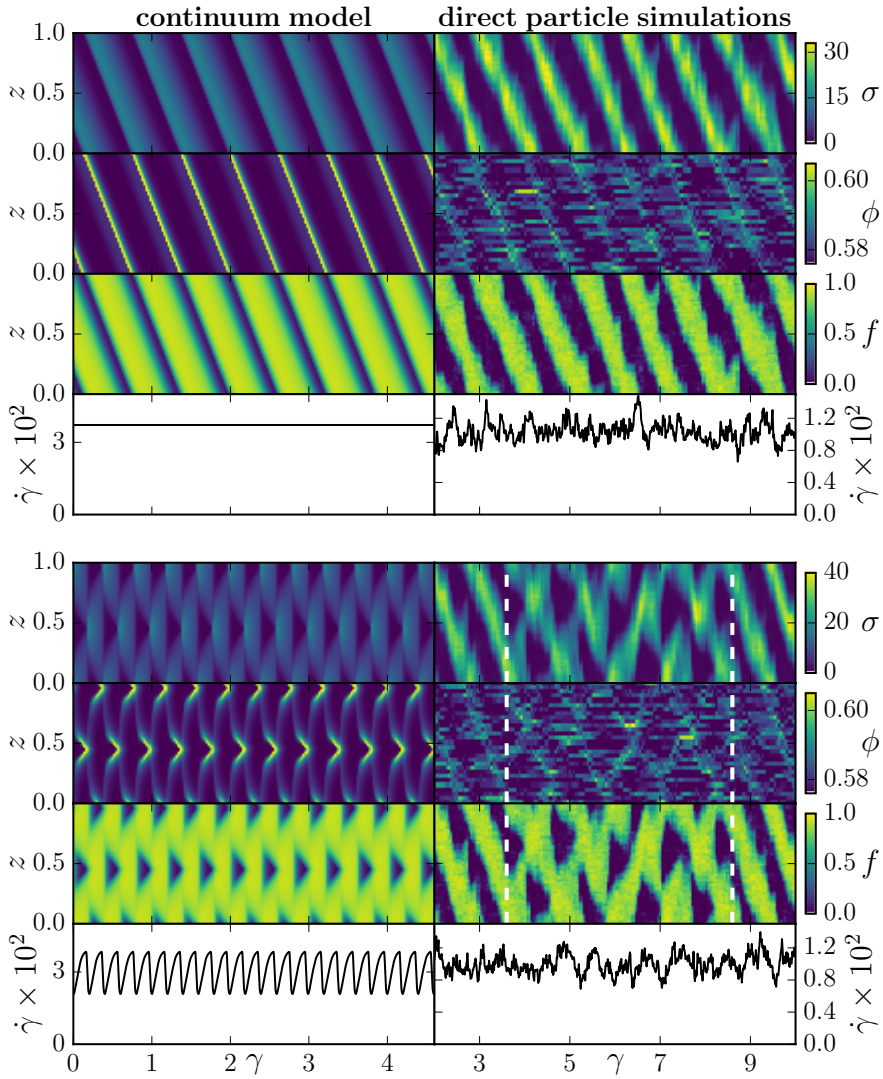

Figure 3.8: Space-strain colour plots of local stress and local volume fraction against strain at a bulk volume fraction $\bar{\phi} = 0.58$ and rescaled drag parameter $\alpha = 1.3 \times 10^8$ for the inhomogeneous large-strain states of the continuum model (left) and direct particle simulations (right). We show a TB generated from our model for $\bar{\sigma} = 6.525$ (bottom left), and a LOB generated from our model for $\bar{\sigma} = 7.25$ (top left). We compare this to particle simulation data for $\bar{\sigma} = 11.8$ (top right), which show TB behaviour, and particle simulation data for $\bar{\sigma} = 13.2$ (bottom right), which transiently show LOB behaviour between strains $\gamma = 2.75$ and $\gamma = 9.35$ (dashed white lines). We also plot the strain rates (line graphs, bottom row of each block) during this evolution.

$\bar{\sigma} = 11.8$, and, transiently, LOBs at $\bar{\sigma} = 13.2$. We show the space-strain plots of the σ, ϕ and f profiles that we find at these $\bar{\sigma}$ values in Fig. 3.8 (right), and compare them with TB and LOB profiles generated from our model in Fig. 3.8 (left). We also compare their shear rate dynamics (bottom row). We use different $\bar{\sigma}$ for evolving our model than were used in the particle simulations to obtain the TB and LOB states: at $\left(\alpha, \bar{\phi}\right) = (1.3 \times 10^8, 0.58)$, the bulk stresses $\bar{\sigma} = 11.8$ and $\bar{\sigma} = 13.2$ are well outside the linearly unstable region predicted by our model. Indeed, our metastability study at the more unstable $\alpha = 10^9$ (Fig. 3.6) suggests that these stresses are outside the metastable TB and LOB regions too. We instead use $\bar{\sigma} = 6.525$ to obtain a TB state in our model, and $\bar{\sigma} = 7.25$ to obtain a LOB state. We see that at $\bar{\sigma} = 11.8$, our particle simulations show σ, ϕ and f profiles that are similar in shape to the TB state we find in our model, and likewise travel at a constant speed in a given direction. At $\bar{\sigma} = 13.2$, the behaviour between strains $\gamma = 2.75$ and $\gamma = 9.35$, though transient, has dynamics that are clearly similar to what is seen in the LOB states of our model. The $\dot{\gamma}$ dynamics, by contrast, do not show the steady or oscillatory behaviour seen in TB or LOB states produced by our model, though this may be due to the large amount of noise in the shear rate signal, masking any such behaviour. We nonetheless have, overall, strong qualitative evidence that we have found our predicted instabilities in our particle simulations, albeit not at the values of $\bar{\sigma}$ we expected.

The successful prediction of TB and LOB states, as well as the differences between the TB and LOB states predicted in the model and seen in the particle simulations, are likely to be a consequence of the minimal nature of our model. One might hope that behaviour generated from a simplified model will be due to generic, underlying physics which should still be present in a more sophisticated model. In the case of our model, we have built it out of ingredients which are generic in themselves. The Wyart-Cates model, for instance, should hold to some extent in any suspension which undergoes a transition between non-frictional and frictional particle interactions as stress is increased. Our frictional state dynamics provide a second example, as they could be considered a leading-order description of a more general dynamics $\dot{f} = -\dot{\gamma}\, g(f)$, expanded around the fixed point f^*. However, the minimal

nature of the model means that factors that could have a significant impact on the observed behaviour in our particle simulations are not taken into account. Most significantly, we take no account of shear plane details. These include features linked to the thickening transition, such as the appearance of local stress fluctuations [53] or force-chain networks [36, 39, 113] which may buckle [114] with an out-of-plane component, thus coupling shear-plane physics to the vorticity axis. Finite-size effects in the shear plane caused by the small area of this plane in our particle simulations constitute another example of shear plane physics our model cannot account for.

One important source of error to consider is our proximity to the critical volume fraction in the Wyart-Cates model [112]. Consider the Wyart-Cates viscosity in its general form [56], $\eta = \eta_0 \left[(1-f)\,\phi_{\mathrm{J}}^0 - f\phi_{\mathrm{J}}^\mu - \phi\right]^{-\nu}$. Any error in the values of η_0, ϕ, ϕ_{J}^μ, or ϕ_{J}^0, or an underestimate of ν, leads to a relative error $|\delta\eta/\eta| \sim 1$ as $\eta \longrightarrow \infty$. (An overestimate of ν by an amount ϵ induces a relative error that scales as η^ϵ.) Thus, even a best case scenario in which the form of our model is correct would not guarantee a viscosity accurate to better than an order of magnitude. This could explain the factor-two discrepancy in the $\bar{\sigma}$ values at which TB and LOB states were found in the model and simulations. This would, in turn, explain the shear rate and strain scale mismatch between the particle simulations and model in Fig. 3.8.

We can gain further insight into the potential sources of disagreement between our model and the particle simulations by testing the equations that comprise the model separately in Fig. 3.9, using the particle simulation data of Fig. 3.8 for a TB state and an LOB state at a representative strain $\gamma = 6$. This figure directly tests Eqs. 3.2.5, 3.2.8b, 3.2.8a and 3.2.8c, though the second row tests Eq. 3.2.8b only after integrating both sides from 0 to z in order to avoid noise from differentiating σ twice. The first two rows of Fig. 3.9 provide strong support for the concentration dynamics we adopt in our model, justifying the simplifications in Eqs. 3.2.5 and 3.2.6 that neglect variations in ϕ. We also see, in the third row of Fig. 3.9, remarkable qualitative similarities between the profiles of $\partial_t f$ and $-\frac{\dot{\gamma}}{\gamma_0}\left[f - e^{-1/\sigma}\right]$. However, variations in $-\frac{\dot{\gamma}}{\gamma_0}\left[f - e^{-1/\sigma}\right]$ are larger than those in $\partial_t f$, which is also shifted to lower values as compared to $-\frac{\dot{\gamma}}{\gamma_0}\left[f - e^{-1/\sigma}\right]$, and able to change sign (e.g. in the trough at $z \approx 0.55$). Thus, Eq. 3.2.8a appears to be approximately an affine trans-

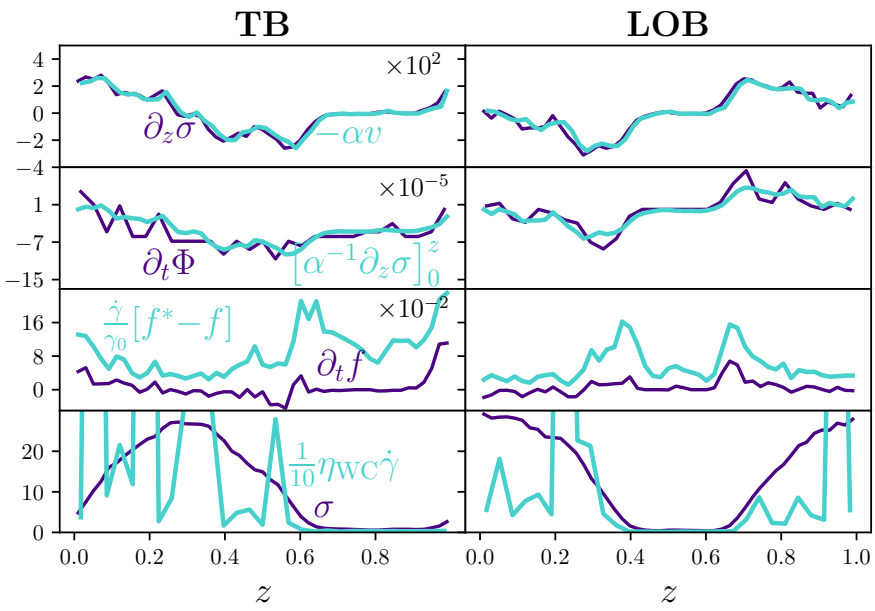

Figure 3.9: Direct testing of Eqs. 3.2.5, 3.2.8b, 3.2.8a and 3.2.8c using particle simulation data exhibiting TB behaviour at $\bar{\sigma} = 11.8$ (left column) and LOB behaviour at $\bar{\sigma} = 13.2$ (right column), as in Fig. 3.8, at a representative strain $\gamma = 6$. First row: $\partial_z \sigma$ (violet) and $-\alpha v$ (turquoise). Second row: $\partial_t \Phi$ (violet) and $[\partial_z \sigma]_0^z$ (turquoise), where $\Phi(z) := \int_0^z \phi(z')\,\mathrm{d}z'$ and $[\partial_z \sigma]_0^z := \partial_z \sigma(z) - \partial_z \sigma(0)$. Third row: $\partial_t f$ (violet) and $-\frac{\dot{\gamma}}{\gamma_0}[f - f^*]$, where $f^* := e^{-1/\sigma}$ (turquoise). Fourth row: σ (violet) and $\frac{1}{10}\eta_{\mathrm{WC}}\dot{\gamma}$ (turquoise), where $\eta_{\mathrm{WC}} := [(1-f)\,\phi_{\mathrm{J}}^0 - f\phi_{\mathrm{J}}^{\mu} - \phi]^{-2}$. Annotation "$\times 10^{\nu}$": scale factor for the corresponding row (e.g. the TB snapshot has $\partial_z \sigma(0) \approx 2 \times 10^2$).

formation away from the true equation for the dynamics of f, suggesting a tweak to our estimate of γ_0 and the form of $f^*(\sigma)$ could improve our description. When testing Eq. 3.2.8c in the fourth row of Fig. 3.9, however, we see little correspondence between the local Wyart-Cates viscosity, $\eta_{\mathrm{WC}} := (\phi_{\mathrm{J}} - \phi)^{-2}$, and the true viscosity $\eta(z) = \sigma(z)/\dot{\gamma}$. This discrepancy is likely exaggerated by the fact that since we are near jamming, a small amount of noise in f and ϕ can lead to arbitrarily large overestimates of η_{WC}.

One assumption of our model is that, aside from the volume fraction dynamics, variables depend only on a local description of the system. This is reasonable if all variables depend on microstructural details at the same scale, which can then be taken as the infinitesimal length of a coarse-grained system, but works less well if this is not the case. One important large-scale phenomenon known to play a role in the thickening of suspensions is, as previously mentioned, the formation of force chains. These are composed of particles in frictional contact with each other, making f a strong candidate for inducing non-local effects on the suspension behaviour. We therefore consider an extended model which accounts for small non-local effects due to f,

$$\partial_t f = -\dot{\gamma}\left[f - e^{-\sigma^{-1}} - l^2\partial_z^2 f\right], \tag{3.4.18a}$$

$$\partial_t \phi = \alpha^{-1}\partial_z^2 \sigma, \tag{3.4.18b}$$

$$\sigma = \left[(1-f)\,\phi_{\mathrm{J}}^0 + f\phi_{\mathrm{J}}^{\mu} - m^2\partial_z^2 f - \phi\right]^{-2}\dot{\gamma}. \tag{3.4.18c}$$

Eqs. 3.4.18a and 3.4.18c may be viewed as minimal phenomenological implementations of physics that shrinks local extrema in f (Eq. 3.4.18a) and reduces their effect on η (Eq. 3.4.18c). More explicitly, the modifications can arise by taking f in $\phi_{\mathrm{J}}(f)$ and $f^*(\sigma(f,\phi))$ to the non-local $(w * f)(z) := \int_0^L w(z-\zeta)\, f(\zeta)\,\mathrm{d}\zeta$ for a zero-centred weight function w. Assuming w to be highly peaked and step-like, we can approximate

$$\begin{aligned}(w * f)(z) &\approx \frac{1}{2\delta}\int_{z-\delta}^{z+\delta} f(\zeta)\,\mathrm{d}\zeta \\ &\approx f(z) + \frac{1}{3}\delta^2\partial_z^2 f(z)\end{aligned}$$

for $\delta \ll 1$, where the second approximation comes from Taylor expanding around

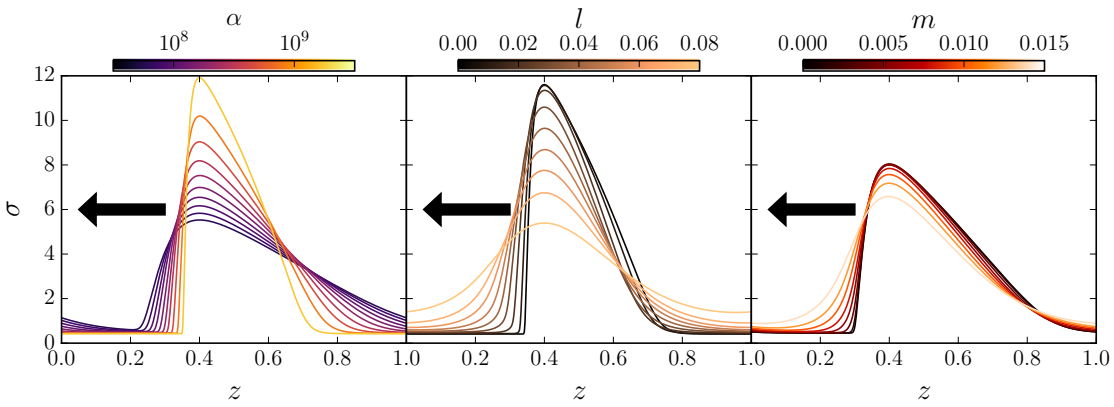

Figure 3.10: TB profiles for a system with $\phi_{\mathrm{J}}^{\mu} = 0.585$, $\phi_{\mathrm{J}}^{0} = 0.646$, $\phi = 0.58$ and $\bar{\sigma} = 2.9$. Left: TB profiles for varied α, $l = m = 0$. Centre: TB profiles for varied l, $\alpha = 9 \times 10^8$, $m = 0$. Right: TB profiles for varied m, $\alpha = 9 \times 10^8$, $l = 0$.

$\delta = 0$. We then see that

$$\phi_{\mathrm{J}}\left(w * f\right) \approx \phi_{\mathrm{J}}\left(f\right) + \frac{\mathrm{d}\phi_{\mathrm{J}}}{\mathrm{d}f}\left(f\right)\delta f,$$
$$f^*\left(\sigma\left(w * f, \phi\right)\right) \approx f^*\left(\sigma\left(f, \phi\right)\right) + \frac{\partial f^*}{\partial f}\left(f, \phi\right)\delta f,$$

where in this case $\delta f = \frac{1}{3}\delta^2 \partial_z^2 f\left(z\right)$. This leaves us with modifications

$$f^* \mapsto f^* + \frac{2}{3}\left(\phi_{\mathrm{J}}^{0} - \phi_{\mathrm{J}}^{\mu}\right)\delta^2 \sigma^{-\frac{1}{2}} \dot{\gamma}^{-\frac{1}{2}} f^* \partial_z^2 f$$
$$\phi_{\mathrm{J}} \mapsto \phi_{\mathrm{J}} - \frac{1}{3}\delta^2\left(\phi_{\mathrm{J}}^{0} - \phi_{\mathrm{J}}^{\mu}\right)\partial_z^2 f.$$

Following the simplifying assumption that for any given system we can treat the coefficients of $\partial_z^2 f$ as approximately constant during the evolution, we can finally absorb these coefficients into the parameters l^2 and m^2 of Eqs. 3.4.18.

We summarise the effect on our stress profile of our non-local parameters l and m, as well as that of α (which is also a non-local parameter), in Fig. 3.10. This shows how TB profiles generated by our model (coloured curves) at $\left(\bar{\phi}, \bar{\sigma}\right) = (0.58, 2.9)$ vary as each parameter is separately varied, with the unchanged parameters being set to zero in the cases of l and m, and 9×10^8 in the case of α. We see that, as expected, increasing l or m reduces the height and curvature of the stress peak. Increasing α, by contrast, localises the stress peak within an increasingly narrow region of the box, resulting in a higher and sharper peak. This makes physical sense, since a higher

value of α means a slower migration of particles in response to stress gradients which are therefore able to build up more easily. This discussion leads us to expect that l^2 and m^2 have the effect of stabilising homogeneous states. Indeed, the effect of m in the linear stability analysis of Eqs. 3.4.18 is to take $(\phi_{\mathrm{J}}^0 - \phi_{\mathrm{J}}^\mu) \mapsto (\phi_{\mathrm{J}}^0 - \phi_{\mathrm{J}}^\mu - m^2k^2)$ in Eq. 3.3.14, while that of l is to add a term $-l^2k^2$ to W_k^{11}, where $\boldsymbol{W}_k$ is the matrix in Eq. 3.3.14. Increasing l or m therefore strictly decreases the trace of $\boldsymbol{W}_k$ without affecting the sign of its determinant, thus stabilising the homogeneous state.

3.5 Conclusion

In this chapter, we have presented a model that predicts dynamic instabilities at negatively-sloped regions on the constitutive curve, so long as the flow cell is large enough along the vorticity direction. Using Dr. Mari's particle simulations, we were able to successfully confirm this prediction, although significant quantitative discrepancies between, e.g., the bulk stress $\bar{\sigma}$ at which the model predicts one should find TB and LOB states, and the $\bar{\sigma}$ at which particle simulations actually find these states, exist. Direct testing of the ingredients of our model on particle simulation data shows that our model captures ϕ dynamics extremely well, and f dynamics qualitatively well. We see less support for the Wyart-Cates expression for the stress itself, though this might be due to proximity to the jamming point, which can amplify the effects of noise by an arbitrarily large amount. More generally, the quantitative mismatch between our model predictions and the particle simulations could be due to our proximity to the jamming point, coupled with the uncertainty inherent in the values chosen for constants such as frictional jamming, ϕ_{J}^μ. Nonetheless, our ability to predict and find TB and LOB states in a particle simulation suggests that our model successfully captures the generic physics that underlies shear thickening. This provides further support for the Wyart-Cates model of shear thickening, and further emphasises and clarifies the role of particle migration in the DST regime: small concentration fluctuations play a significant role in the rheology of suspensions close to jamming, something previously reported for colloidal glasses in pipe flow [115].

Experimental evidence of instabilities provided part of the motivation for this chapter. This consisted, in particular, of observations of unsteady shear rates [95,96]. The shear rate dynamics of the LOB state is consistent with one kind of unsteady flow observed in such experiments, in which $\dot{\gamma}$ is seen to oscillate periodically [95,96]. However, stress profiles in the LOB state evolve in a manner suggestive of a pair of solitons travelling in opposite directions at constant speed and interfering with one another, a behaviour dependant on the adoption of periodic boundary conditions. It is therefore unlikely that LOB states could exist in an experimental system. We are also unable to obtain with our model the chaotic flow seen above ϕ_{J}^{μ} and σ_{J} by Hermes *et al.*, even by considering the effect of non-zero inertia in the system (see §3.7). Part of the explanation for this could lie in coupling between the inertia of the rheometer and the suspension [96]. More fundamentally, suspensions can jam into a solid, particularly at the high volume fractions and stress at which Hermes *et al.* find chaos, but our model is only able to approach jamming asymptotically. If chaos involves, for instance, coupling between a jammed and a flowing band, this could explain our inability to find it with our model.

Encouragingly, a recent paper by Saint-Michel *et al.* [97] describes observations strongly suggestive of TB behaviour in a suspension of cornstarch. Using ultrasound imaging, they observe inhomogeneous behaviour in the flow-component v_x of the particle-phase velocity, with low-velocity bands travelling at a constant speed along the vorticity axis. This is reminiscent of the v_z behaviour seen in our model and in particle simulations (Fig. 3.11), and could be interpreted as a consequence of coupling between a v_z band and the boundary of the suspension. Furthermore, we see in the top-right of Fig. 3.8 that bands cross the simulation box, of size 815.34 particle radii, six times between strains $\gamma \approx 2.75$ and $\gamma \approx 9.35$. This corresponds to a band speed $c_{\mathrm{sim}} = 741$ particle radii per units of strain. At applied shear stress $\bar{\Sigma} = 12\,\mathrm{Pa}$, Saint-Michel *et al.* [97] find a band with velocity $c \approx 14\,\mathrm{mm\,s^{-1}}$ at a shear rate $\dot{\gamma} \approx 1.5\,\mathrm{s^{-1}}$. With particle radii of size 0.015 mm, this corresponds to a speed of $c_{\mathrm{exp}} \approx 622$ particle radii per units of strain, a value similar to that of c_{sim}. Saint-Michel *et al.* [97] also find evidence of weak concentration banding, further strengthening the argument that their observations correspond to the TB states we

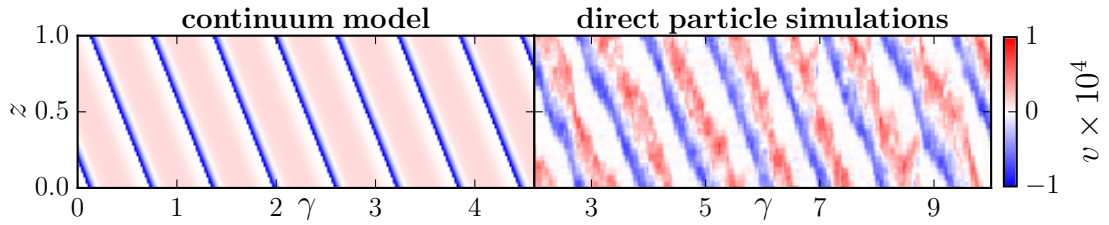

Figure 3.11: Vorticity component v of the particle-phase velocity from the model and particle simulations for the TB data shown in Fig. 3.8.

see in our model and simulation data.

The work in this chapter raises a number of interesting questions. Perhaps the most urgent of these, if we wish to relate this work to experimental systems, is the need to understand what the consequences of more realistic boundary conditions would be for the instabilities we find. It is not clear what such conditions would be, and whether it would be possible to implement them without needing a constitutive model for the full three-dimensional system, the development of which is still an open problem for dense suspensions [116], as discussed in the next two chapters. As such, particle simulations may be a more promising approach to tackling this question than further modelling.

Another open question concerns gradient banding. Static gradient banding is not expected to be possible in dense suspensions [95], but experimental evidence [117] exists of gradient banding involving particle migration. Due to the large system sizes required for linear instability, such questions may be difficult to address through particle simulations, particularly if coupling between the vorticity axis and shear plane is involved. As such, continuum models could prove useful for exploring this question, building on previous work [68] for the high-inertia regime.

It might also be worth considering a recent extension to the Wyart-Cates model that allows for more complicated constitutive behaviour [55], particularly involving shear thinning at low and high stresses. By extending that model in the same way as we extended the Wyart-Cates model in this chapter, it might be possible to find dynamical behaviours not seen in the current study.

3.6 Appendix I: Time integration of the continuum model

We numerically solve Eqs. 3.2.8 using the forward Euler method [118] on 512 regularly-spaced gridpoints. Our time-stepping is done in real space, except for that due to the $\partial_z^2\sigma$ term in Eq. 3.2.8b, which is done in Fourier space. The discrete Fourier transform was performed using the FFTW package [119]. We set an initial time-step $\Delta t = 10^{-6}$, and determine subsequent time-steps using step-doubling [118] with an error term $\epsilon := \max_{z_i \in \text{grid}} |\eta_2(z_i) - \eta_1(z_i)| \,/\, \langle\eta\rangle$, where the $\eta_2(z_i)$ (resp. $\eta_1(z_i)$) is the viscosity at gridpoint z_i after a single forward Euler step across a time interval $2\Delta t$ (resp. two forward Euler steps across a time interval Δt). We choose a parameter-dependent upper bound on ϵ such that halving the error tolerance does not change the $t \longrightarrow \infty$ profiles. For TB states, we check this by shifting the final state in z to get a best match between the two profiles, and for LOB states we check this by shifting in both z and t.

All numerical results presented in this chapter adopted values $\phi_{\mathrm{J}}^{\mu} = 0.58$ and $\phi_{\mathrm{J}}^{0} = 0.64$. When preparing the initial condition for a system on the constitutive curve at time $t = 0$, perturbations to homogeneous states were of the form $\delta f = 10^{-3} \sum_{k=1}^{2} \cos\left(2\pi\left[kz + \chi_k\right]\right)$ and $\delta\phi = 10^{-4} \sum_{k=1}^{2} \cos\left(2\pi\left[kz + \xi_k\right]\right)$, where the χ_k and ξ_k are uniformly distributed random numbers in $[0, 1)$.

Finally, we note that the numerical artifacts seen in Fig. 3.7 are a consequence of our finite grid size. Time-series of $\dot{\gamma}$, $\hat{f}_k$ and $\hat{\phi}_k$ show these states to be steady, implying that they do not result from a lack of convergence in time. As seen in Fig. 3.7, the artifacts are not systematically present at all points on a given stress sweep. Since they have no visible impact (e.g. adding noise) on our results in Fig. 3.6, we are confident in the reliability of our results despite the occasional presence of the artifacts.

3.7 Appendix II: Inertial model

As seen in §3.3.1, homogeneous flow is linearly stable in our model for all (finite) parameter values as we approach or pass the jamming stress σ_{J}. We check here if including inertia in our model allows us to find a Reynolds number above which homogeneous jamming is linearly unstable, in line with some other models of unsteady flow [68, 96]. We do this by adding an inertial term to Eq. 3.2.5,

$$\mathrm{Re}\left(\partial_t v + v\partial_z v\right) = -\left(\partial_z \sigma + \alpha\phi v\right), \tag{3.7.19}$$

where $\mathrm{Re} := \frac{\rho L^2 \sigma_c}{\gamma_0^2 \eta_0^2}$ is the Reynolds number, which corresponds to the non-dimensionalised particle density. This gives us an inertial model in the form

$$\partial_t \phi = -\left[\phi\partial_z v + v\partial_z \phi\right], \tag{3.7.20}$$

$$\partial_t f = -\dot{\gamma}\left[f - f^*\left(\sigma\right)\right], \tag{3.7.21}$$

$$\partial_t v = -\left[\mathrm{Re}^{-1}\left(\partial_z \sigma + \alpha\phi v\right) + v\partial_z v\right]. \tag{3.7.22}$$

We perturb this system and linearise our evolution equations, yielding the dispersion relation

$$\partial_t \begin{pmatrix} \delta\hat{f}_k \\ \delta\hat{\phi}_k \\ \delta\hat{v}_k \end{pmatrix} = \begin{pmatrix} -\dot{\gamma} + 2\bar{\sigma}^{-\frac{1}{2}}\dot{\gamma}^{\frac{1}{2}} e^{-\bar{\sigma}^{-1}}\left(\phi_{\mathrm{J}}^0 - \phi_{\mathrm{J}}^{\mu}\right) & 2\bar{\sigma}^{-\frac{1}{2}}\dot{\gamma}^{\frac{1}{2}} e^{-\bar{\sigma}^{-1}} & 0 \\ 0 & 0 & -2\pi i k\bar{\phi} \\ -4\pi i k\left(\phi_J^0 - \phi_J^{\mu}\right)\bar{\sigma}^{\frac{3}{2}}\dot{\gamma}^{-\frac{1}{2}}\mathrm{Re}^{-1} & -4\pi i k\bar{\sigma}^{\frac{3}{2}}\dot{\gamma}^{-\frac{1}{2}}\mathrm{Re}^{-1} & \mathrm{Re}^{-1}\alpha\bar{\phi} \end{pmatrix} \begin{pmatrix} \delta\hat{f}_k \\ \delta\hat{\phi}_k \\ \delta\hat{v}_k \end{pmatrix}. \tag{3.7.23}$$

To see if this modification allows us to destabilise a jammed state, we take the limit $\dot{\gamma} \longrightarrow 0$, leaving us with the system of equations

$$\partial_t \delta f = 0, \tag{3.7.24}$$

$$\partial_t \delta\phi = -\bar{\phi}\partial_z \delta v, \tag{3.7.25}$$

$$0 = \left[\left(\phi_J^0 - \phi_J^{\mu}\right)\delta f + \delta\phi\right]. \tag{3.7.26}$$

We see that Eq. 3.3.16 holds, as in the non-inertial case, and that therefore Eq. 3.3.17 holds. The system is still linearly stable above jamming when inertia is included in this way.

Chapter 4

Fabric tensor dynamics of dense non-Brownian suspensions: phenomenological modelling

4.1 Introduction

In the previous chapter, we were able to develop a one-dimensional model for the dynamics of shear-thickening suspensions that, at least qualitatively, held up well when tested against a particle simulation. It is therefore natural to ask what the scope is for a more general, three-dimensional suspension model. Such a model would require one to account for features that are necessarily absent in a model of the vorticity axis physics, particularly the evolution and impact of microstructural anisotropy. In suspensions under shear or extension, this anisotropy shows up in the pair-distribution of particles, which has a peak near contact along the compressional axis and a trough near contact along the extensional axis [36, 120–127]. This has consequences for the constitutive behaviour of suspensions [24, 124, 128–130], such as the presence of non-zero normal stresses [21, 90, 131–137], or the mechanical tunability of viscosity [138, 139]. Frictional contact and short-ranged repulsion between particles, which play a crucial role in shear thickening (c.f. Ch. 3), also affect the microstructure, leading, for instance, to fore-aft asymmetry [36, 122, 124, 140, 141]. Further influences on the microstructure include finite temperatures [77, 130, 142]

and mismatching between the particle and suspending fluid densities [143, 144].

Many of these complicating effects can be avoided by considering a neutrally-buoyant non-Brownian hard-sphere suspension with neither inertia nor repulsive forces keeping particles apart, so that particles interact only through hydrodynamics or frictional contact. Such a system lacks any intrinsic time scale, so that material variables such as viscosity evolve as a function of material deformation only [24, 70, 123, 145–147]. This system also lacks the concentration coupling and frictional state dynamics that enabled the instabilities seen in Ch. 3, and so should remain homogeneous under flow. In simple shear, the same dimensional constraint implies that the stress tensor, $\mathbf{\Sigma}$, must have shear stress proportional to the shear rate, $\dot{\gamma}$, and normal stresses N_1 and N_2 proportional to $|\dot{\gamma}|$. (The sign dependence is determined by the requirement of symmetry under simultaneous reflection along the flow and flow gradient axes.) This does not imply a Newtonian rheology: experiments [131–135,148–150] and simulations [87,137] find N_2 to be large and negative in sufficiently dense systems of this type. For its part, the sign of N_1 remains controversial, with experimental evidence existing for $N_1 < 0$ [131,132,134,148], $N_1 \approx 0$ [133], and $N_1 > 0$ [135], all for a similar volume fraction range, $0.2 < \phi < 0.55$. Fewer simulation measurements of N_1 in non-Brownian hard-sphere suspensions exist, but two studies [87, 151] find $N_1 < 0$, while a third [137] finds the sign of N_1 to vary with ϕ.

In the absence of friction, Hinch and Leal [152] have shown how the sparsity of ingredients in this system can be harnessed to develop phenomenological constitutive models [152]. By releasing the constraint of linearity, which is broken by the existence of frictional contacts, we might similarly hope to model frictional suspensions. Successfully applied constitutive models of polymer solutions and melts [153] provide instructive examples. Typically, such models (e.g. the Johnson-Segalman [154] or Giesekus [155] models) are directly or implicitly composed of a model for the evolution of the polymer microstructure paired with an expression for the polymer stress as a function of said microstructure. Finite time scales in these models lead to a continuous response of the polymer stress to changes in the imposed flow. Non-Brownian suspensions of hard particles, by contrast, have contact chains that can break instantly if the direction of shear changes [24, 89, 145, 146, 156], and an im-

plicit relationship is unlikely to capture the resulting particle stress discontinuities. Accordingly, constitutive models of this system [152, 157–162] follow instead the explicit route, encoding the microstructure in a symmetric rank-2 "fabric tensor" $\boldsymbol{Q}$ representing the distribution of near-contacts.

The proposed microstructural models are rarely tested against experimental or simulated suspensions (with Stickel *et al.* [159] a notable exception [159, 163]). Instead, usually only the resulting stress tensor is tested, or even just the shear component of the stress [158, 161, 162]. Experimentally, one explanation for this lies in the difficulty of obtaining data on the near-contact distribution of dense non-Brownian suspensions. Such data requires imaging suspensions under viscometric flows at high spatial resolution, a task made difficult at high density due to opacity of the suspension. For confocal imaging, this requires accurate refractive index matching [124, 164]. Alternatively, Deboeuf *et al.* [165] have recently obtained detailed measurements of the pair-distribution function using X-ray tomography. Particle simulations, for their part, can test the assumptions of a model if the microscopic assumptions upon which they are built are consistent with the assumptions of the model, but cannot test the validity of the model unless these microscopic assumptions have themselves been shown to be valid. As discussed in Ch. 3, only recently has the importance of frictional contacts to the rheology of dense suspensions been appreciated [166], and have simulations capable of quantitatively matching experiments on dense suspensions been developed [78, 87, 93].

In this chapter, we harness these new numerical capabilities to test the suitability of fabric models for the evolution of dense non-Brownian suspension microstructure. Using a general result due to Hand [167] for the evolution of a tensor as a function of itself and the velocity gradient tensor, we build a series of increasingly high-order polynomial models for the fabric tensor evolution. We then fit these models against data generated by Dr. Mari for nearly-hard, frictional, non-Brownian particles with no particle-particle interactions other than short-ranged lubrication and frictional contact.

The simulated suspension is equivalent to a CLM suspension with a vanishing critical load $F_* = 0$, as described in §2.4. Dr. Mari simulates 500 particles in a

periodic cube of volume fraction-dependent edge length. As before, the simulated suspension is bi-disperse, with particle populations of radius a and $1.4a$ taking up an approximately equal total volume of suspension. The results presented here are averaged over 250 realisations of the flow reversal. This system, lacking the size and interpolating frictional state that generated the instabilities in Ch. 3, is homogeneous.

We adopt shear reversal as our flow protocol, imposing a velocity vector field $\boldsymbol{v} = (\dot{\gamma}y, 0, 0)$ for $\dot{\gamma} > 0$ on an initially isotropic suspension until steady-state is reached (requiring in practice five units of strain in our particle simulation), then instantaneously inverting the direction of shear, $\dot{\gamma} \mapsto -\dot{\gamma}$, at a time we define as $t = 0$. Shear reversal preserves the simplicity of shear flow, such as the linear dependence of the microstructural evolution on $\dot{\gamma}$ and $|\dot{\gamma}|$ imposed by dimensional constraints, or the vanishing of xz and yz components of rank-2 tensors due to $(x, y, z) \mapsto (-x, -y, z)$ symmetry. Shear reversal is also, however, a severe test of the ability of a given model to capture the microstructural response to flow. As hydrodynamic forces instantaneously change direction upon reversal, some frictional contacts will immediately break, leading to a rebalancing of load in the frictional contact networks formed in steady state [36, 39, 168]. There will therefore be a corresponding instantaneous change in the contribution of interparticle contacts to the total stress [168]. A suspension under shear reversal will experience both lubrication-dominated and friction-dominated regimes, since the contact network requires a finite amount of strain to rebuild in response to the new direction of shear, during which period hydrodynamic interactions dominate [78, 89, 168]. Shear reversal is also a prototype for more common rheological set-ups. In our system with no intrinsic time scale, smooth oscillatory shear, for instance, is fully equivalent as a function of strain to a series of shear reversals. Studying shear reversal may also shed light on other, more complicated flows, such as biaxial shear [138, 139] or the flow around a sphere sinking into a sheared dense suspension [54, 169, 170]. Shear reversal therefore constitutes a simultaneously simple, stringent and generic flow protocol with which to test microstructural models.

In this chapter, we find that no linear model can fit our particle simulation data

for shear reversal, and that, though higher-order polynomial models can succeed, such models are unlikely to be physically meaningful. We discuss the implications of our result for fabric tensor models of dense suspension microstructure and stress. A detailed interrogation of the microstructural assumptions inherent in fabric tensor models of the microstructure follows in Ch. 5.

4.2 Fabric tensor

The divergence of hydrodynamic lubrication forces between particles at vanishing separation and the long-range decay of perturbations to the velocity field induced by the presence of a hard sphere [33] mean that, even allowing for lubrication breakdown and a regularising cut-off of the lubrication forces [38], pair-wise interactions—contact and lubrication—will dominate the dynamics of the suspension. Indeed, our particle simulations neglect long-range interactions for this reason, cutting off the lubrication interaction when the normalised interparticle gap size h is above 0.2 (c.f. §2.4), where $h := 2r/(a_i + a_j) - 2$ for a pair of particles with radii a_i and a_j a centre-to-centre distance r apart. The pair-distribution $g(\boldsymbol{r})$ is therefore the key microstructural characteristic. In a dense suspension, $g(\boldsymbol{r})$ is sharply peaked at or near contact [36, 142, 165, 168, 171, 172], so we expect the forces due to particle pairs close to or within contact to dominate. Indeed, the median gap size $\tilde{h}$ for pairs with separation within the lubrication cut-off in Dr. Mari's particle simulation stays roughly below 10% of mean particle radius across the reversal for the representative volume fractions we will use in this study, $\phi = 0.4$, 0.5 and 0.55, as shown in Fig. 4.1. Given the high density of pairs near contact, and the fact that the closest of these dominate the forces in the system, we may reasonably hope that the distribution $P(\boldsymbol{p})$ of near-contact orientations $\boldsymbol{p} \in S^2$ contains all the microstructural information needed to describe the rheology and dynamics of a dense suspension.

Directly modelling the evolution of $P(\boldsymbol{p})$ (let alone $g(\boldsymbol{r})$ [142, 172]) is difficult. It is also likely to be more than is necessary to describe the stress tensor $\boldsymbol{\Sigma}$, which, as a symmetric rank-2 tensor, contains far less information than $P(\boldsymbol{p})$. Instead, we follow the lead of previous researchers, both in the context of suspensions [152,

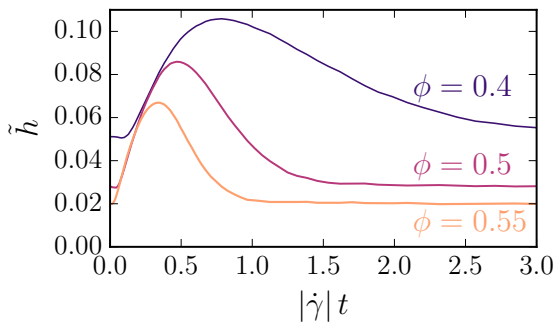

Figure 4.1: Median interparticle gap $\tilde{h}$ as a function of post-reversal strain $|\dot{\gamma}|t$ for three volume fractions $\phi = 0.4$, 0.5 and 0.55, from numerical simulations.

157–160] and more broadly (e.g. in granular [173–175], polymeric [153] or liquid crystalline [176, 177] contexts), who instead model the de-traced second moment of the orientational distribution, $\boldsymbol{Q} := \langle \boldsymbol{p} \otimes \boldsymbol{p} \rangle - \frac{1}{3}\boldsymbol{I}$, or an equivalent object. In suspensions and granular contexts where $\boldsymbol{p}$ is a (near-)contact orientation, $\boldsymbol{Q}$ is called a fabric tensor. Since every pair with normalised centre-to-centre vector $\boldsymbol{p}$ also has centre-to-centre vector $-\boldsymbol{p}$, $P(\boldsymbol{p}) = P(-\boldsymbol{p})$ and all odd moments of the orientational distribution vanish. The second moment is therefore the lowest non-trivial moment of the distribution, so one may interpret $\boldsymbol{Q}$ as a measure of the lowest-order anisotropy of $P(\boldsymbol{p})$. In line with this interpretation, $\boldsymbol{Q}$ appears as the second-order term in the spherical harmonic expansion of $P(\boldsymbol{p})$ in tensor form [178] (see also Appendix 4.5),

$$P(\boldsymbol{p}) = \frac{1}{4\pi}\left(1 + \frac{15}{2}\boldsymbol{Q} : \boldsymbol{p}\boldsymbol{p} + \dots\right). \tag{4.2.1}$$

Having chosen our structure tensor [152] with which to encode the microstructure, we can apply symmetric and dimensional constraints to build a general phenomenological model for the microstructural evolution. Frame indifference (c.f. §2.3) implies that any function F of a tensor $\boldsymbol{T}$ and the velocity gradient $\nabla\boldsymbol{v}$ with symmetric and anti-symmetric parts $\boldsymbol{D}$ and $\boldsymbol{\Omega}$ respectively must be of the the form [37]

$$F(\nabla\boldsymbol{v}, \boldsymbol{T}) = \boldsymbol{\Omega}\cdot\boldsymbol{T} - \boldsymbol{T}\cdot\boldsymbol{\Omega} + \tilde{F}(\boldsymbol{D}, \boldsymbol{T}), \tag{4.2.2}$$

where $\tilde{F}$ corresponds to F in a frame in which $\boldsymbol{\Omega} \equiv \boldsymbol{0}$. Pairing this result with a generalisation of the Cayley-Hamilton theorem to pairs of symmetric tensors [179],

Hand [167] showed that one can write a general equation for the evolution of a tensor $\boldsymbol{T}$ whose rate of change is a function of itself and $\nabla\boldsymbol{v}$,

$$\begin{aligned}\dot{\boldsymbol{T}} = \boldsymbol{\Omega}\cdot\boldsymbol{T} - \boldsymbol{T}\cdot\boldsymbol{\Omega} + \alpha_0\boldsymbol{I} + \alpha_1\boldsymbol{T} + \alpha_2\boldsymbol{D} + \alpha_3\boldsymbol{T}^2 + \alpha_4\boldsymbol{D}^2 \\ + \alpha_5\left(\boldsymbol{D}\cdot\boldsymbol{T} + \boldsymbol{T}\cdot\boldsymbol{D}\right) + \alpha_6\left(\boldsymbol{D}\cdot\boldsymbol{T}^2 + \boldsymbol{T}^2\cdot\boldsymbol{D}\right) \\ + \alpha_7\left(\boldsymbol{D}^2\cdot\boldsymbol{T} + \boldsymbol{T}\cdot\boldsymbol{D}^2\right) + \alpha_8\left(\boldsymbol{D}^2\cdot\boldsymbol{T}^2 + \boldsymbol{T}^2\cdot\boldsymbol{D}^2\right), \qquad (4.2.3)\end{aligned}$$

where the scalar coefficients α_i are analytic functions of the joint invariants $I_1 := \mathrm{Tr}[\boldsymbol{T}]$, $I_2 := \mathrm{Tr}[\boldsymbol{T}^2]$, $I_3 := \mathrm{Tr}[\boldsymbol{T}^3]$, $I_4 := \mathrm{Tr}[\boldsymbol{D}]$, $I_5 := \mathrm{Tr}[\boldsymbol{D}^2]$, $I_6 := \mathrm{Tr}[\boldsymbol{D}^3]$, $I_7 := \mathrm{Tr}[\boldsymbol{T}\cdot\boldsymbol{D}]$, $I_8 := \mathrm{Tr}[\boldsymbol{T}^2\cdot\boldsymbol{D}]$, $I_9 := \mathrm{Tr}[\boldsymbol{T}\cdot\boldsymbol{D}^2]$, and $I_{10} := \mathrm{Tr}[\boldsymbol{T}^2\cdot\boldsymbol{D}^2]$.

We apply Hand's result to our system, supplemented by the additional constraints of tracelessness and proportionality of rates-of-change to $\dot{\gamma}$ and $|\dot{\gamma}|$. We then non-dimensionalise our model, choosing $|\dot{\gamma}|^{-1}$ as our time unit, so that the strain $\gamma := |\dot{\gamma}|t$ is our non-dimensionalised time variable. We obtain, in these units,

$$\begin{aligned}\dot{\boldsymbol{Q}} = \hat{\boldsymbol{\Omega}}\cdot\boldsymbol{Q} - \boldsymbol{Q}\cdot\hat{\boldsymbol{\Omega}} + \hat{\alpha}_1\boldsymbol{Q} + \hat{\alpha}_2\hat{\boldsymbol{D}} + \hat{\alpha}_3\boldsymbol{Q}^2 + \hat{\alpha}_4\hat{\boldsymbol{D}}^2 \\ + \hat{\alpha}_5\left(\hat{\boldsymbol{D}}\cdot\boldsymbol{Q} + \boldsymbol{Q}\cdot\hat{\boldsymbol{D}}\right) + \hat{\alpha}_6\left(\hat{\boldsymbol{D}}\cdot\boldsymbol{Q}^2 + \boldsymbol{Q}^2\cdot\hat{\boldsymbol{D}}\right) \\ + \hat{\alpha}_7\left(\hat{\boldsymbol{D}}^2\cdot\boldsymbol{Q} + \boldsymbol{Q}\cdot\hat{\boldsymbol{D}}^2\right) + \hat{\alpha}_8\left(\hat{\boldsymbol{D}}^2\cdot\boldsymbol{Q}^2 + \boldsymbol{Q}^2\cdot\hat{\boldsymbol{D}}^2\right) \\ - \frac{1}{3}\left(\hat{\alpha}_3\hat{I}_2 + \hat{\alpha}_4\hat{I}_5 + 2\hat{\alpha}_5\hat{I}_7 + 2\hat{\alpha}_6\hat{I}_8 + 2\hat{\alpha}_7\hat{I}_9 + 2\hat{\alpha}_8\hat{I}_{10}\right)\boldsymbol{I}, \qquad (4.2.4)\end{aligned}$$

where $\hat{\boldsymbol{\Omega}} := \boldsymbol{\Omega}/|\dot{\gamma}|$ and $\hat{\boldsymbol{D}} := \boldsymbol{D}/|\dot{\gamma}|$, and where the $\hat{\alpha}_i$ and $\hat{I}_j$ are to $\hat{\boldsymbol{D}}$ what the α_i and I_j are to $\boldsymbol{D}$. This is a general equation, in our reference frame where $\boldsymbol{v} = (\dot{\gamma}(t)\,y, 0, 0)$, for the rate-independent fabric evolution $\dot{\boldsymbol{Q}}$ as a function of $\boldsymbol{Q}$ and $\nabla\boldsymbol{v}$ analytic in its arguments. Eq. 4.2.4 is not analytic about $\dot{\gamma} = 0$. This is unavoidable. Taking $\dot{\gamma} \mapsto -\dot{\gamma}$ in our reference frame is equivalent to taking $x \mapsto -x$, which doesn't affect the T_{xx} component of any second-order tensor $\boldsymbol{T}$, or taking $y \mapsto -y$, which doesn't affect the T_{yy} component. This, combined with the proportionality constraint, implies that $\dot{Q}_{xx}$ and $\dot{Q}_{yy}$ are proportional to $|\dot{\gamma}|$. This is acceptable, however, because $\dot{\gamma}$ is the only source of a time scale in our system. Thus, $\dot{\gamma} = 0$ corresponds to a singular regime in which nothing evolves, and it is reasonable to define analyticity on a domain that excludes this point. Finally, we

note that Eq. 4.2.4 can be written in component form (see §4.6) as

$$\begin{aligned}
\dot{Q}_- &= P_- \left[Q_+, \operatorname{sgn}(\dot{\gamma})Q_{xy}, Q_-^2\right] Q_- + 2\operatorname{sgn}(\dot{\gamma})Q_{xy}, \\
\dot{Q}_+ &= P_+ \left[Q_+, \operatorname{sgn}(\dot{\gamma})Q_{xy}, Q_-^2\right], \\
\dot{Q}_{xy} &= P_{xy} \left[Q_+, \operatorname{sgn}(\dot{\gamma})Q_{xy}, Q_-^2\right] \operatorname{sgn}(\dot{\gamma}) - \frac{1}{2}\operatorname{sgn}(\dot{\gamma})Q_-,
\end{aligned} \tag{4.2.5}$$

for functions P_-, P_+ and P_{xy} analytic in their arguments, where $Q_\pm := Q_{11} \pm Q_{22}$. From Eqs. 4.2.5, one sees that (Q_-, Q_+, Q_{xy}) is the natural basis in which to examine models for the evolution of $\boldsymbol{Q}$ [160].

We have at this point defined the fabric tensor $\boldsymbol{Q}$ in terms of a distribution of near-contacts $P(\boldsymbol{p})$. To complete the definition, we must specify what particle pairs are included in the set of near-contacts that $P(\boldsymbol{p})$ describes. One might, for instance, adopt the set of orientations of edges in a Delaunay triangulation connecting the centres of particles. We instead use the computationally simpler criterion that near-contacts are within a gap $h \leq \epsilon$ for some "coarse-graining length" $\epsilon \geq 0$. The dominant forces are due to pairs at or near contact. We might therefore hope to find a value of ϵ large enough to include these dominant pairs, but small enough to exclude pairs that contribute little to the total stress of the suspension and mask the orientational distribution of the pairs that contribute a lot. Given such an ϵ, we should arrive at a microstructural object capable of describing the stress in the suspension and, by the same token, informing its own evolution.

Writing $\boldsymbol{Q}^\epsilon$ for the fabric tensor corresponding to a given choice of ϵ, we further illustrate the connection between the fabric tensor and the stress in Fig. 4.2, in which we plot the stress $\boldsymbol{\Sigma}$ against the contact fabric $\boldsymbol{Q}^0$ as seen in our particle simulations at volume fraction $\phi = 0.5$ across the reversal at $t = 0$. We see qualitative similarities between the two, such as the discontinuities in all components at the moment of reversal. (Strictly speaking, because we are simulating nearly-hard spheres, rather than true hard spheres, the discontinuities are rapid continuous changes over a strain of roughly 1%, as seen in the insets to Fig. 4.2.) We also see that the sign reversal of the xy component occurs over a similar strain scale for $\boldsymbol{\Sigma}$ and $\boldsymbol{Q}^0$.

Though these qualitative similarities are encouraging, modelling discontinuities in the components of $\boldsymbol{Q}$ upon reversal through ODEs such as Eqs. 4.2.5 is not possible. so we must instead consider a finite coarse-graining length $\epsilon > 0$ which,

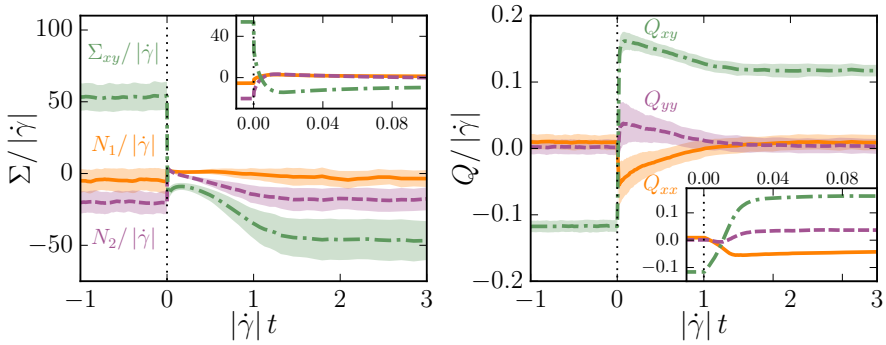

Figure 4.2: Stress and fabric data from numerical simulations for a shear reversal from a shear rate $\dot\gamma > 0$ before reversal at $t = 0$ to a post-reversal shear-rate $-\dot\gamma < 0$ at volume fraction $\phi = 0.5$. Left: Stress tensor components Σ_{xy} (green, dash-dotted), $N_1 = \Sigma_{xx} - \Sigma_{yy}$ (orange, solid) and $N_2 = \Sigma_{yy} - \Sigma_{zz}$ (purple, dashed) divided by $|\dot\gamma|$. Thick dark-shaded lines are the averaged data, while the light shaded area around each curve is the standard deviation obtained from the individual shear reversals. Right: Components of the contact fabric tensor $\boldsymbol{Q}^0$, with averages in thick lines and standard deviation in shaded areas. Insets: zoom in on strains near the point of reversal.

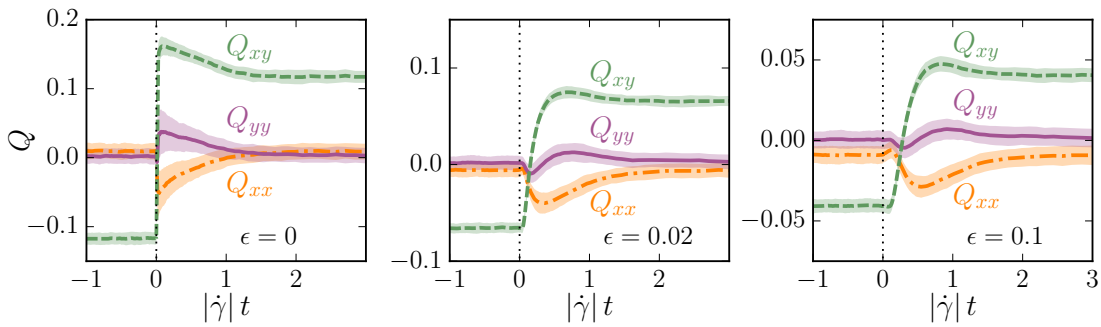

Figure 4.3: Evolution of the fabric $\boldsymbol{Q}^\epsilon$ for the same data as in Fig. 4.2, but for a variety of coarse-graining lengths $\epsilon = 0$ (left), 0.02 (centre) and 0.1 (right), demonstrating how choosing $\epsilon > 0$ removes the discontinuity in $\boldsymbol{Q}^\epsilon$ at the moment of shear reversal.

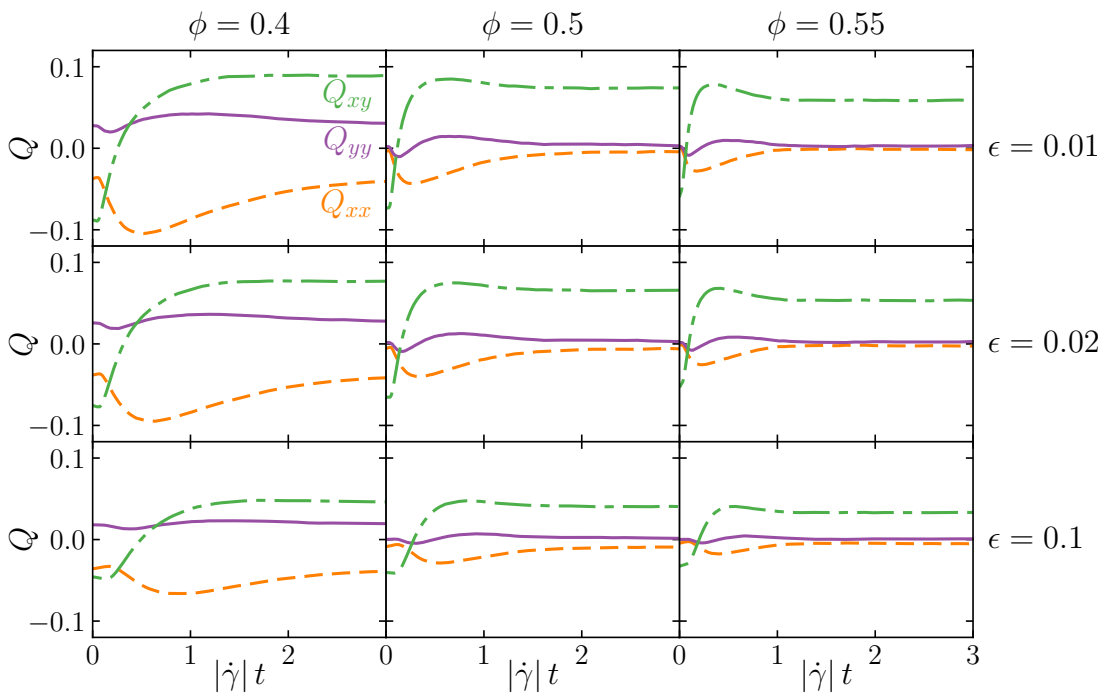

Figure 4.4: Post-reversal (at $t = 0$) evolution of the fabric tensor components Q_{xx} (orange, dashed), Q_{yy} (violet, solid) and Q_{xy} (green, dash-dotted) for three volume fractions $\phi = 0.4$ (left), 0.5 (centre) and 0.55 (right) and for three coarse-graining lengths $\epsilon = 0.01$ (top), 0.02 (middle) and 0.1 (bottom), from numerical simulations.

as shown in Fig. 4.3, removes the discontinuity. In the limit of hard particles, few particles will remain in contact an instant after reversal, so we in any case require a finite ϵ to account for the dominant lubrication interactions due to particles just out of contact. The stress, which is necessarily discontinuous upon reversal [168], might then be modelled as a function $\boldsymbol{\Sigma}(\boldsymbol{Q}, \nabla \boldsymbol{v})$, with discontinuities arising via instantaneous changes in $\nabla \boldsymbol{v}$. In principle, modelling the stress in this way will involve experimenting with the value of ϵ. However, as shown in Fig. 4.4 for three volume fractions $\phi = 0.4$, 0.5 and 0.55, varying ϵ across an order of magnitude does not lead to significant qualitative changes in the post-reversal evolution of $\boldsymbol{Q}^{\epsilon}$. We therefore choose a representative value $\epsilon = 0.02$ in the rest of this chapter, except where explicitly stated.

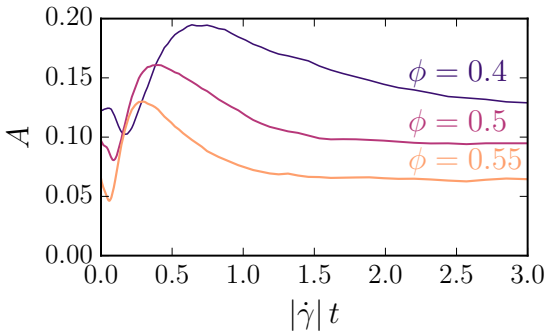

Figure 4.5: Anisotropy A as a function of post-reversal strain for three volume fractions $\phi = 0.4$, 0.5 and 0.55, from numerical simulations.

4.3 Polynomial Hand equations

We consider dense suspensions at volume fractions ϕ not too far below the jamming point ϕ_{J} at which particles are unable to move due to overcrowding. Above ϕ_{J}, motion in any direction is prevented by contact with a particle. Since our suspension is amorphous, we would expect the limiting microstructure at jamming to be isotropic or near-isotropic, and that volume fractions close to jamming should be at most weakly anisotropic. We confirm this expectation by quantifying the anistropy as $A := (4\pi)^{-1} \int_{S^2} \left[4\pi P(\boldsymbol{p}) - 1\right]^2 \mathrm{d}\Omega$, whose post-reversal evolution we show in Fig. 4.5.

From Eq. 4.2.1, we also see that $\boldsymbol{Q}$ is a measure of the anisotropy of $P(\boldsymbol{p})$. We thus expect our weakly anisotropic suspension to have a correspondingly small size of $\boldsymbol{Q}$. This is supported by Fig. 4.4, which shows that larger coarse-graining lengths (which correspond to more isotropic near-contact orientation distributions) have fabric tensor components of smaller magnitude. More precisely, we see that the norm $|\boldsymbol{Q}| := \sqrt{\mathrm{Tr}[\boldsymbol{Q}^2]}$ has approximate values 0.01, 0.048 and 0.0022 at respective volume fractions $\phi = 0.4$, 0.5 and 0.55, for the most anisotropic coarse-graining length shown, $\epsilon = 0.01$. This is in comparison to the maximal value $|\boldsymbol{Q}| = \sqrt{2/3} \approx 0.816$, calculated for a unaxial distribution, such that e.g. $\langle \boldsymbol{pp} \rangle = \hat{\boldsymbol{x}} \otimes \hat{\boldsymbol{x}}$. We therefore expect that the analytic functions P_-, P_+ and P_{xy} in Eqs. 4.2.5 are well-approximated by low-order Taylor expansions in their arguments. This in turn suggests a modular approach of building phenomenological models for the evolution of $\boldsymbol{Q}$, taking the

analytic functions in Eqs. 4.2.5 to be polynomials of increasingly high degree until a satisfactory model is obtained.

4.3.1 Linear models

Expanding the analytic functions in Eqs. 4.2.5 to linear order, we obtain

$$\begin{aligned} P_- &= a_-, \\ P_+ &= a_+ + b_+ Q_+ + c_+ \operatorname{sgn}(\dot\gamma) Q_{xy}, \\ P_{xy} &= a_{xy} + b_{xy} Q_+ + c_{xy} \operatorname{sgn}(\dot\gamma) Q_{xy}, \end{aligned} \tag{4.3.6}$$

where the a's, b's and c's are fitting parameters. Adopting this choice for the dynamics of P_-, P_+ and P_{xy} in Eqs. 4.2.5 yields the 7-parameter general (for our choice of reference frame) linear model for $\dot{\boldsymbol{Q}}$ as a function of itself and $\nabla \boldsymbol{v}$,

$$\begin{aligned} \dot Q_- &= a_- Q_- + 2 \operatorname{sgn}(\dot\gamma) Q_{xy}, \\ \dot Q_+ &= a_+ + b_+ Q_+ + \operatorname{sgn}(\dot\gamma) c_+ Q_{xy}, \\ \dot Q_{xy} &= \operatorname{sgn}(\dot\gamma) a_{xy} + \operatorname{sgn}(\dot\gamma) b_{xy} Q_+ + c_{xy} Q_{xy} - \frac{1}{2} \operatorname{sgn}(\dot\gamma) Q_-. \end{aligned} \tag{4.3.7}$$

We adopt a method, described in an article by Cheng *et al.* [180], to obtain fits of this model to data from Dr. Mari's simulations. We calculate $\dot Q_-$, $\dot Q_+$ and $\dot Q_{xy}$ from numerical data via numerical differentiation, and then use linear least squares [118] on our model with $\boldsymbol{Q}$ data taken from the particle simulation to obtain a set of coefficients that minimise the cost function

$$\begin{aligned} X_1 := \int_{\gamma=0}^{\gamma=3} \Bigg[& \left(\dot Q_-^{\text{data}} - P_- \left[Q_+^{\text{data}}, \operatorname{sgn}(\dot\gamma) Q_{xy}^{\text{data}}, Q_-^{2\,\text{data}} \right] - 2 \operatorname{sgn}(\dot\gamma)\, Q_{xy}^{\text{data}} \right)^2 \\ & + \left(\dot Q_+^{\text{data}} - P_+ \left[Q_+^{\text{data}}, \operatorname{sgn}(\dot\gamma) Q_{xy}^{\text{data}}, Q_-^{2\,\text{data}} \right] \operatorname{sgn}(\dot\gamma) \right)^2 \\ & + \left(\dot Q_{xy}^{\text{data}} - P_{xy} \left[Q_+^{\text{data}}, \operatorname{sgn}(\dot\gamma) Q_{xy}^{\text{data}}, Q_-^{2\,\text{data}} \right] + \frac{1}{2} Q_-^{\text{data}} \right)^2 \Bigg] \mathrm{d}\gamma, \end{aligned} \tag{4.3.8}$$

where $\gamma := |\dot\gamma| t$. Increasing the upper limit of the integral in the definition of X_1 decreases the weighting of the early post-reversal regime in the fit while increasing that of the steady state. We choose the value $\gamma = 3$ for this upper limit as a compromise capable of yielding accurate fits to both regimes. Having obtained an initial

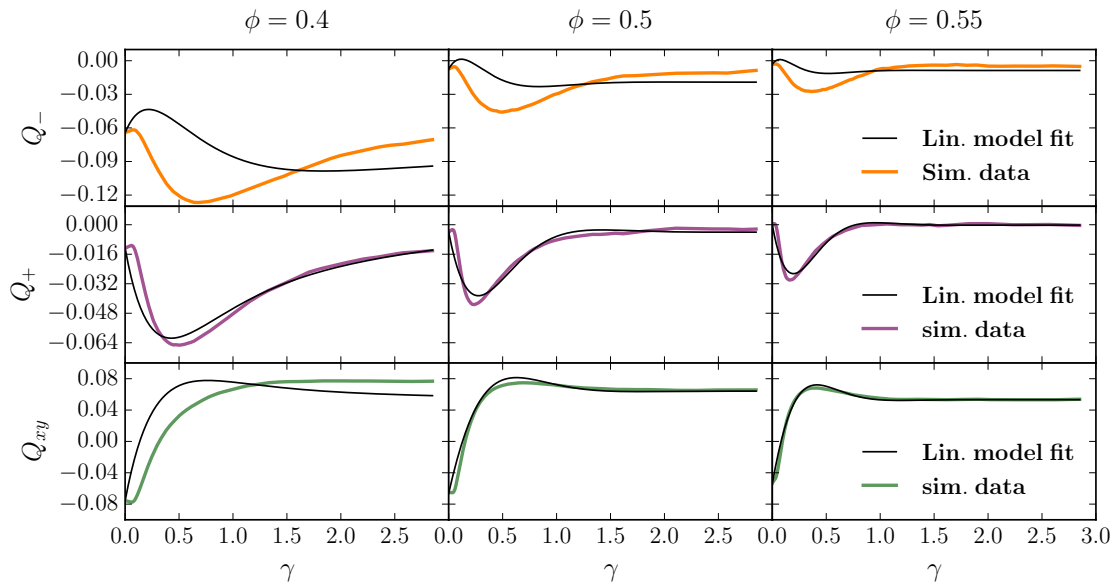

Figure 4.6: Fit of the linear model described by Eq. 4.3.6 to simulation data for the three components of $\boldsymbol{Q}$ (respectively Q_-, Q_+ and Q_{xy} from top to bottom) against post-reversal strain for $\phi = 0.4$ (left), $\phi = 0.5$ (center) and $\phi = 0.55$ (right).

set of coefficients in this way, we perform a gradient descent, minimising the cost function

$$X_2 = \int_{\gamma=0}^{\gamma=3} \left[\left(Q_-^{\text{fit}} - Q_-^{\text{data}}\right)^2 + \left(Q_+^{\text{fit}} - Q_+^{\text{data}}\right)^2 + \left(Q_{xy}^{\text{fit}} - Q_{xy}^{\text{data}}\right)^2 \right] \mathrm{d}\gamma, \tag{4.3.9}$$

where the $Q_{ij}^{\text{fit}}(\gamma)$ data are obtained for each set of coefficients by numerically integrating the resulting ODE. The set of fit parameters obtained from the gradient descent are at least a local minimizer of X_2, and we adopt these as our "best fit" parameters.

Fig. 4.6 shows the fit thus obtained of Eqs. 4.3.7 to particle simulation data for three volume fractions $\phi = 0.4$, 0.5 and 0.55. It is clear from Fig. 4.6 that the linear model does a poor job of fitting the evolution of Q_-, even if it yields good fits to Q_+ and Q_{xy}. This is not a product of our fitting methodology, but a consequence of the highly-constrained form of P_- in the linear model, as we now show.

Eqs. 4.3.7 give us

$$\dot{Q}_- = a_- Q_- + 2\,\mathrm{sgn}(\dot{\gamma}) Q_{xy}. \tag{4.3.10}$$

We write $\boldsymbol{Q}^{-\text{SS}}$ and $\boldsymbol{Q}^{+\text{SS}}$ for the pre- and post-reversal steady-state fabric tensor

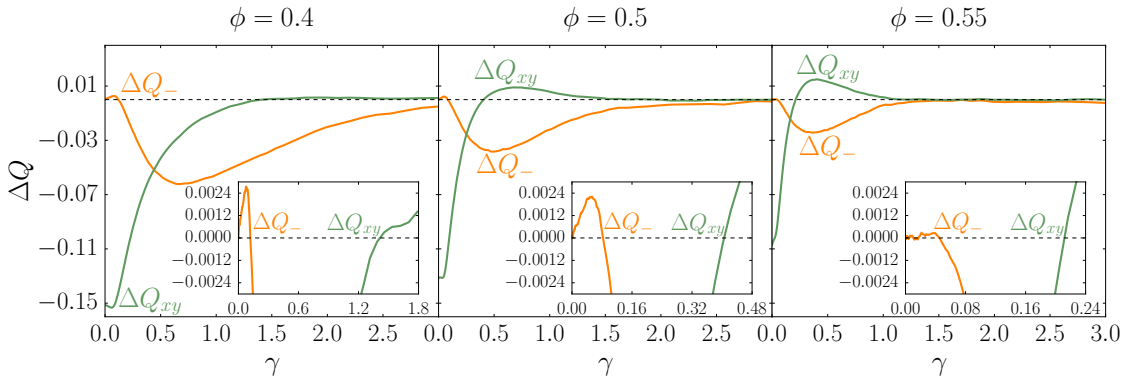

Figure 4.7: Simulation data for ΔQ_- and ΔQ_{xy} against post-reversal strain for volume fractions $\phi = 0.4$ (left), $\phi = 0.5$ (centre) and $\phi = 0.55$ (right). Eq. 4.3.14 implies that ΔQ_- cannot change sign after reversal until ΔQ_{xy}. This condition is unambiguously violated for all of our simulation data. Insets: zoom in on the region where the condition is violated.

$\boldsymbol{Q}$ respectively, and note that Eq. 4.3.10 implies that

$$0 = a_- Q_-^{+\mathrm{SS}} + 2\,\mathrm{sgn}(\dot{\gamma}) Q_{xy}^{+\mathrm{SS}}. \tag{4.3.11}$$

We then define $\Delta\boldsymbol{Q} := \boldsymbol{Q} - \boldsymbol{Q}^{+\mathrm{SS}}$ and subtract the RHS of Eq. 4.3.11 from Eq. 4.3.10 to get

$$\Delta\dot{Q}_- = a_- \Delta Q_- + 2\,\mathrm{sgn}(\dot{\gamma}) \Delta Q_{xy}. \tag{4.3.12}$$

Since $Q_-(\gamma = 0) = Q_-^{-\mathrm{SS}} = Q_-^{+\mathrm{SS}}$, we see that $\Delta Q_-(\gamma = 0) = 0$ so that Eq. 4.3.12 has solution

$$\Delta Q_-(\gamma) = 2\,\mathrm{sgn}(\dot{\gamma}) \int_0^\gamma e^{a_-[\gamma - \gamma']} \Delta Q_{xy}(\gamma')\, \mathrm{d}\gamma'. \tag{4.3.13}$$

Writing $\gamma_* := \inf\{\gamma : \Delta Q_{xy}(\gamma) = 0\}$, and noticing that $\Delta Q_{xy}(0) = 2Q_{xy}^{-\mathrm{SS}}$, we obtain the result

$$\mathrm{sgn}(\Delta Q_-) = \mathrm{sgn}(\dot{\gamma})\,\mathrm{sgn}\big(Q_{xy}^{-\mathrm{SS}}\big) \quad \forall\, \gamma \in (0, \gamma_*)\,. \tag{4.3.14}$$

Eq. 4.3.14 gives us a necessary criterion for the ability of linear fabric tensor models to fit shear reversal data: ΔQ_- cannot change sign after reversal until ΔQ_{xy} does so. In Fig. 4.7, we see that this criterion is unmet for all three volume fractions we consider. This yields the first important conclusion of this chapter: *no linear model for $\dot{\boldsymbol{Q}}$ as a function of $\boldsymbol{Q}$ and $\nabla\boldsymbol{v}$ can fit the simulation data for shear reversal.*

4.3.2 Sources of non-linearity

One common source of non-linearity in models of microstructural evolution, seen for instance in the liquid crystals literature [177], is the "closure approximation" used to express $\langle \boldsymbol{pppp} \rangle : \boldsymbol{D}$ as a function of $\langle \boldsymbol{pp} \rangle$ (or, equivalently, $\boldsymbol{Q}$). This term arises from the fact that two points advecting in a velocity gradient $\nabla \boldsymbol{v}$ with vector $\boldsymbol{r}$ pointing from one to the other have squared separation growing at a rate (in Einstein notation) $2r_i\dot{r}_i = 2r_iD_{ij}r_j$. Subtracting this term off for the case of a unit vector $\boldsymbol{p}$ pointing from one advecting point to another, we note that $-p_iD_{ij}p_j = -p_ip_ip_jp_kD_{jk}$, which corresponds to an evolution equation

$$\dot{\boldsymbol{p}} = \nabla \boldsymbol{v} \cdot \boldsymbol{p} - \boldsymbol{ppp} : \boldsymbol{D}, \tag{4.3.15}$$

so that advection contributes a term $\langle \boldsymbol{pppp} \rangle : \boldsymbol{D}$ to the evolution of $\langle \boldsymbol{pp} \rangle$. The closure approximation is then required so that the evolution of $\langle \boldsymbol{pp} \rangle$ can be described without the need for an additional equation for the evolution of $\langle \boldsymbol{pppp} \rangle$. (In general, the evolution of the nth moment of the distribution of $\boldsymbol{p}$ will depend on the $n+2$th moment, so some type of closure approximation will inevitably be required in order to obtain a closed set of equations for the evolution of a finite list of moments.)

We consider four closures for the rheology of rigid oriented particles, a subset of those considered in the detailed study by Feng *et al.* [181] in the context of liquid crystals. The first of these is the linear closure proposed by Hinch and Leal [182],

$$\langle \boldsymbol{pppp} \rangle : \boldsymbol{D} \approx \frac{2}{15}\boldsymbol{Q} + \frac{2}{7}\left(\boldsymbol{Q} \cdot \boldsymbol{D} + \boldsymbol{D} \cdot \boldsymbol{Q}\right) + \frac{1}{7}\left(\boldsymbol{Q} : \boldsymbol{D}\right)\boldsymbol{I}. \tag{4.3.16}$$

This is obtained by taking the lowest-anisotropic-order spherical harmonic expansion of $P(\boldsymbol{p})$,

$$P(\boldsymbol{p}) \approx \frac{1}{4\pi}\left(1 + \frac{15}{2}\boldsymbol{Q} : \boldsymbol{p} \otimes \boldsymbol{p}\right), \tag{4.3.17}$$

when calculating $\langle \boldsymbol{pppp} \rangle$. Hinch and Leal [182] provide two more closures,

$$\langle \boldsymbol{pppp} \rangle : \boldsymbol{D} \approx \frac{1}{5}\left[6\langle \boldsymbol{pp} \rangle \cdot \boldsymbol{D} \cdot \langle \boldsymbol{pp} \rangle - \left(\langle \boldsymbol{pp} \rangle : \boldsymbol{D}\right)\langle \boldsymbol{pp} \rangle - 2\left(\left[\langle \boldsymbol{pp} \rangle^2 - \langle \boldsymbol{pp} \rangle\right] : \boldsymbol{D}\right)\boldsymbol{I}\right] \tag{4.3.18}$$

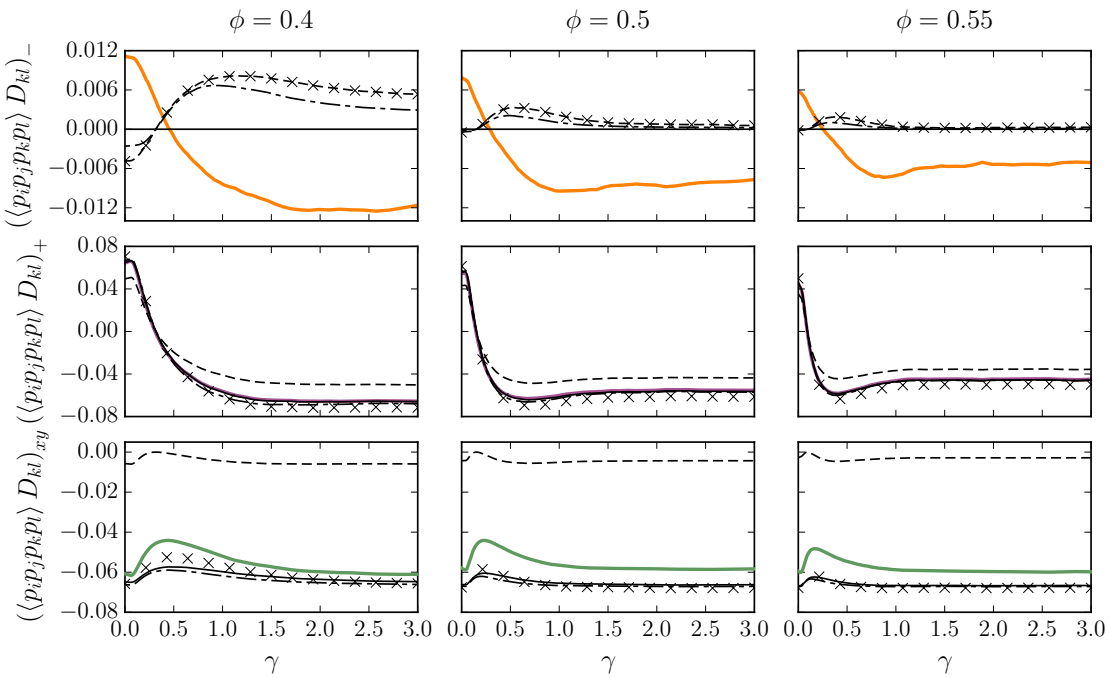

Figure 4.8: Post-reversal evolution of $\langle \boldsymbol{pppp} \rangle : \boldsymbol{D}$ from simulation data (thick, coloured) compared against closure approximations from the literature (thin, black) for volume fractions $\phi = 0.4$ (left), 0.5 (centre) and 0.55 (right). Solid: Eq. 4.3.16. Cross-hatched: Eq. 4.3.18. Dash-dotted: Eq. 4.3.19. Dashed: Eq. 4.3.20.

and

$$\begin{aligned}\langle \boldsymbol{pppp} \rangle : \boldsymbol{D} \approx (\langle \boldsymbol{pp} \rangle : \boldsymbol{D}) \langle \boldsymbol{pp} \rangle + 2 \left[\langle \boldsymbol{pp} \rangle \cdot \boldsymbol{D} \cdot \langle \boldsymbol{pp} \rangle - \frac{\langle \boldsymbol{pp} \rangle^2 : \boldsymbol{D}}{\mathrm{Tr}[\langle \boldsymbol{pp} \rangle^2]} \langle \boldsymbol{pp} \rangle^2 \right] \\ + \exp \left[\frac{2 \left(1 - 3\,\mathrm{Tr}[\langle \boldsymbol{pp} \rangle^2]\right)}{1 - \mathrm{Tr}[\langle \boldsymbol{pp} \rangle^2]} \right] \left[\frac{52}{315} \boldsymbol{D} - \frac{8}{21} \left(\boldsymbol{D} \cdot \langle \boldsymbol{pp} \rangle + \langle \boldsymbol{pp} \rangle \cdot \boldsymbol{D} \right) \right. \\ \left. - \frac{16}{63} \left(\langle \boldsymbol{pp} \rangle : \boldsymbol{D} \right) \boldsymbol{I} \right],\end{aligned} \tag{4.3.19}$$

based on interpolating between $\langle \boldsymbol{pppp} \rangle : \boldsymbol{D}$ calculated for a highly-isotropic and highly-uniaxial distribution $P(\boldsymbol{p})$ expanded up to lowest (Eq. 4.3.18) and second-to-lowest (Eq. 4.3.19) order. Finally, we also consider a closure due to Doi [183],

$$\langle \boldsymbol{pppp} \rangle : \boldsymbol{D} \approx (\boldsymbol{Q} : \boldsymbol{D}) \left(\boldsymbol{Q} + \frac{1}{3} \boldsymbol{I} \right), \tag{4.3.20}$$

obtained through "trial and error" in the context of liquid crystals.

In Fig. 4.8, we plot the evolution of $\langle \boldsymbol{pppp} \rangle : \boldsymbol{D}$ after shear reversal from our particle simulations, and compare it to the closures found in the literature, with $\langle \boldsymbol{pp} \rangle$ also obtained from simulation data. We see that the linear approximation provides excellent quantitative agreement with the $(p_i p_j p_k p_l D_{kl})_+$ data and qualitative agreement with the $(p_i p_j p_k p_l D_{kl})_{xy}$ data, but yields $(p_i p_j p_k p_l D_{kl})_- \equiv 0$, in disagreement with the simulation data. This is similar to the situation seen in Fig. 4.6, and reinforces the significance of the Q_- component as the hardest-to-fit component of $\boldsymbol{Q}$. That said, $(p_i p_j p_k p_l D_{kl})_-$ is of small magnitude, and the linear closure, Eq. 4.3.16, provides the best agreement with the simulation data of the closures we consider in this chapter. A linear closure might thus be "good enough" to capture the advection of near-contact orientations.

We can test this claim directly, using the simulation data to show that advection is not the source of non-linearities in our fabric evolution. The fabric tensor $\boldsymbol{Q}$ evolves between γ and $\gamma + \mathrm{d}\gamma$ through three distinct processes: the advection of near-contacts, consisting of particle pairs with separation $h(\gamma) \leq \epsilon$ and $h(\gamma + \mathrm{d}\gamma) \leq \epsilon$; the birth of near-contacts when a pair of particles has $h(\gamma) > \epsilon$ but $h(\gamma + \mathrm{d}\gamma) \leq \epsilon$; and the death of near-contacts when $h(\gamma) \leq \epsilon$ but $h(\gamma + \mathrm{d}\gamma) > \epsilon$. Writing r^{b} and r^{d} for the number of near-contact births and deaths per near-contact per unit strain respectively, $\boldsymbol{Q}^{\mathrm{b}}$ and $\boldsymbol{Q}^{\mathrm{d}}$ for the near-contact birth and death fabric tensors, and $\dot{\boldsymbol{Q}}^{\mathrm{a}}$ for the advective contribution to $\dot{\boldsymbol{Q}}$ from near-contacts neither instantaneously being born nor dying, we have (see §4.6)

$$\dot{\boldsymbol{Q}} = \dot{\boldsymbol{Q}}^{\mathrm{a}} + r^{\mathrm{b}} \boldsymbol{Q}^{\mathrm{b}} - r^{\mathrm{d}} \boldsymbol{Q}^{\mathrm{d}}. \tag{4.3.21}$$

We can then attempt to fit (using linear least squares) the linear model, Eq. 4.2.5, separately to each of $\dot{\boldsymbol{Q}}^{\mathrm{a}}$, $r^{\mathrm{b}} \boldsymbol{Q}^{\mathrm{b}}$ and $r^{\mathrm{d}} \boldsymbol{Q}^{\mathrm{d}}$. The fit to $\dot{\boldsymbol{Q}}^{\mathrm{a}}$, shown in the top three rows of Fig. 4.9, is excellent. This confirms our expectation that advection of near-contact orientations, and specifically the choice of a closure approximation, is not the reason for the unsuitability of linear fabric models. Instead, the bottom two blocks of Fig. 4.9 show that it is the birth and death of near-contacts that are responsible for this. A particularly poor correspondence between fit and data is seen when the birth and death contributions take their largest values in amplitude, which is precisely when good accuracy matters most.

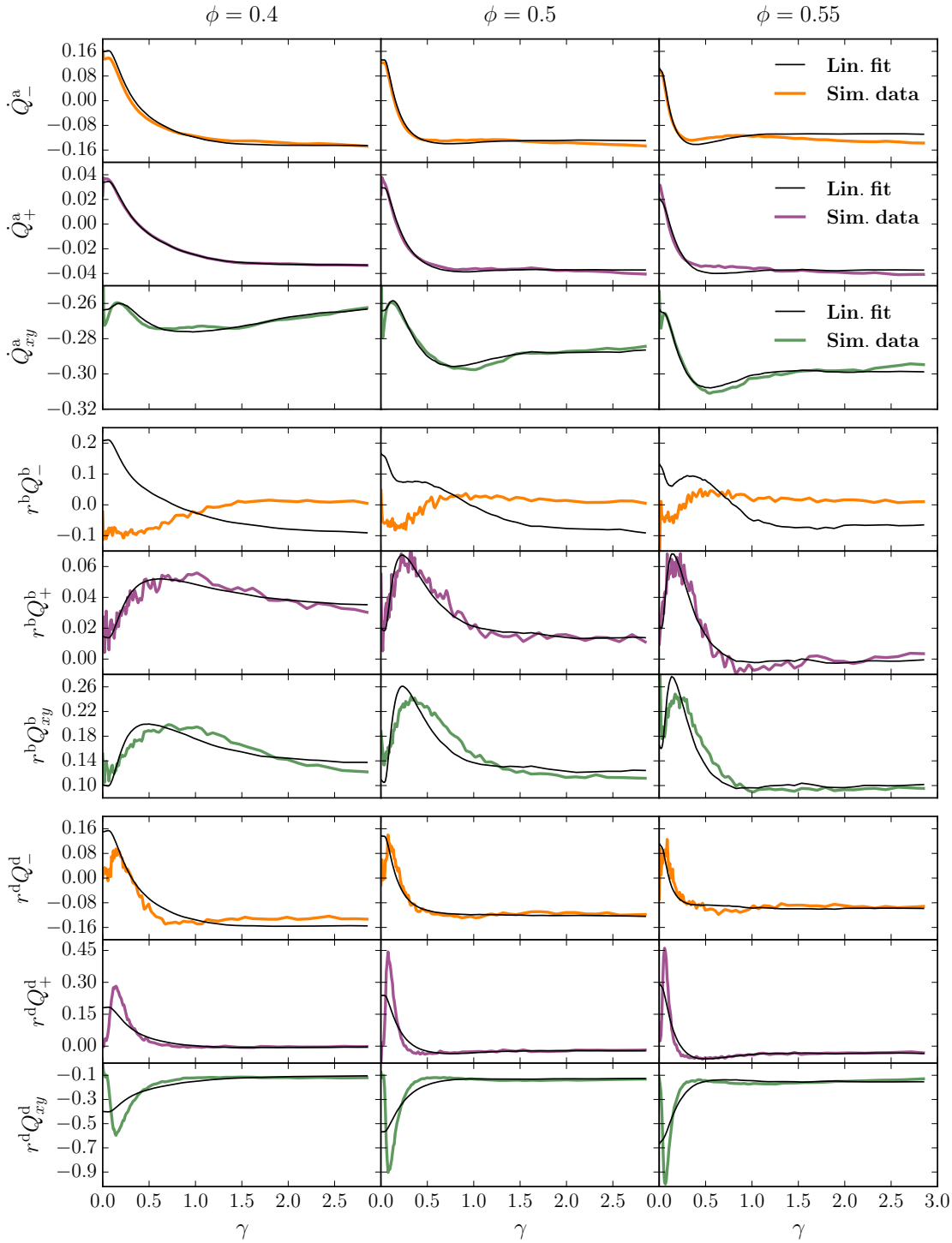

Figure 4.9: Fit (coloured lines) of the linear model, Eq. 4.3.6, to simulation data (black lines) for the components of $\dot{\boldsymbol{Q}}^{\mathrm{a}}$ (top row), $r^{\mathrm{b}}\boldsymbol{Q}^{\mathrm{b}}$ (middle row) and $r^{\mathrm{d}}\boldsymbol{Q}^{\mathrm{d}}$ (bottom row) for volume fractions $\phi = 0.4$ (left column), 0.5 (middle column) and 0.55 (right column).

4.3.3 Higher-order Hand equations

Having shown that linear models cannot fit the reversal data, we consider the 15-parameter general quadratic model

$$\begin{aligned} P_- &= a_- + b_- Q_+ + c_- \operatorname{sgn}(\dot\gamma) Q_{xy}, \\ P_+ &= a_+ + b_+ Q_+ + c_+ \operatorname{sgn}(\dot\gamma) Q_{xy} + d_+ Q_+^2 + e_+ Q_{xy}^2 + f_+ Q_-^2, \\ P_{xy} &= a_{xy} + b_{xy} Q_+ + c_{xy} \operatorname{sgn}(\dot\gamma) Q_{xy} + d_{xy} Q_+^2 + e_{xy} Q_{xy}^2 + f_{xy} Q_-^2. \end{aligned} \tag{4.3.22}$$

Our previous approach to obtaining fits to simulation data, using linear least squares to minimise Eq. 4.3.8 and obtain an initial set of best-fitting parameters from which to launch a gradient-descent and minimise Eq. 4.3.9, frequently fails for the general quadratic model described by Eqs. 4.3.22. The initial parameter sets obtained from minimising Eq. 4.3.8 can cause $\boldsymbol{Q}$ to grow unbounded when used to evolve $\boldsymbol{Q}$ from its initial condition. This can be understood by viewing the general quadratic model through the prism of the overdamped dynamics of a three-dimensional vector $\boldsymbol{s} := \{Q_-, Q_+, Q_{xy}\}$ in a cubic potential, $\dot{s}_i = -\partial_{s_i}[A_{jkl} s_j s_k s_l + B_{jk} s_j s_k + C_k s_k]$, with tensors $\boldsymbol{A}$, $\boldsymbol{B}$ and $\boldsymbol{C}$ determined by the coefficients in Eq. 4.3.22. A cubic potential is generically non-confining, so unless the initial conditions lie within the basin of attraction of a local potential minimum, $\boldsymbol{s}$ will grow unbounded. Finding a well-behaved quadratic fabric evolution model then involves identifying parameters such that $\{Q_-^{\text{-SS}}, Q_+^{\text{-SS}}, Q_{xy}^{\text{-SS}}\}$ lies within such a basin, an unsatisfactory approach at best.

By setting some parameters of Eq. 4.3.22 to zero, we can restrict the parameter space enough to find a model with a bounded evolution, for which our fitting methodology succeeds. The best quadratic model we could find in this manner takes the 11-parameter form

$$\begin{aligned} P_- &= a_- + b_- Q_+ + c_- \operatorname{sgn}(\dot\gamma) Q_{xy}, \\ P_+ &= a_+ + b_+ Q_+ + c_+ \operatorname{sgn}(\dot\gamma) Q_{xy} + e_+ Q_{xy}^2, \\ P_{xy} &= a_{xy} + b_{xy} Q_+ + c_{xy} \operatorname{sgn}(\dot\gamma) Q_{xy} + e_{xy} Q_{xy}^2. \end{aligned} \tag{4.3.23}$$

As seen in Fig. 4.10, this model yields for the most part excellent fits, though we observe a decreasing quality of fit for Q_- as ϕ increases. This may be due to lower

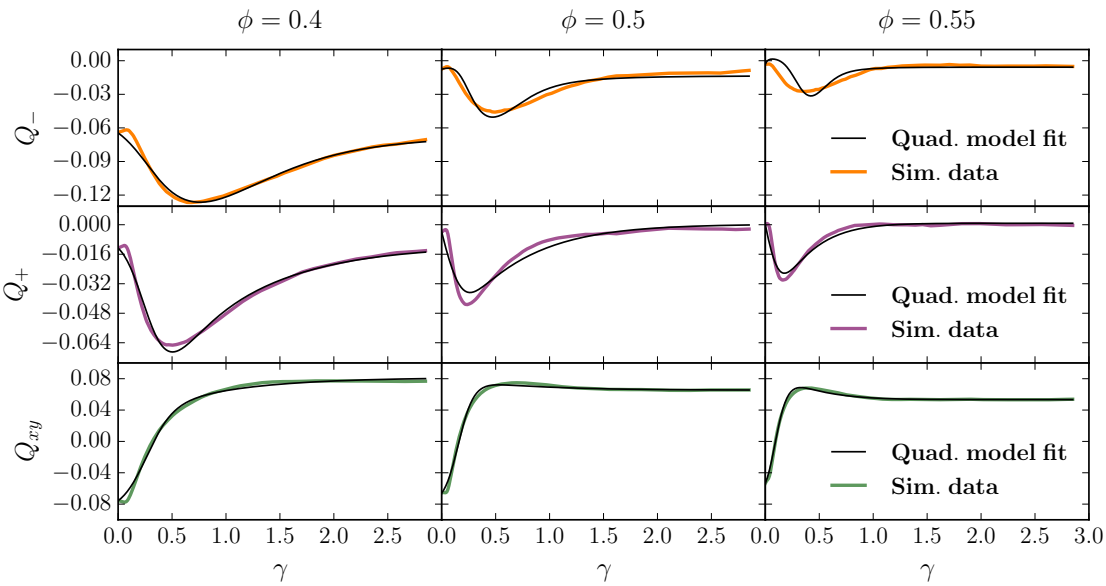

Figure 4.10: Fit to simulation data of the quadratic model described by Eqs. 4.3.23 for Q_- (top), Q_+ (middle) and Q_{xy} (bottom) against post-reversal strain for $\phi = 0.4$ (left), $\phi = 0.5$ (centre) and $\phi = 0.55$ (right).

volume fractions having smaller r^b and r^d values across the evolution (see Fig. 4.11), yielding flatter, easier-to-fit curves.

We have had to constrain our parameter space in order to find a model for which our fitting methodology works, and so it is likely that a quadratic model allowing for better fits than that represented by Eq. 4.3.23 exists. We can nonetheless conclude that quadratic models are capable of being well-fit to the shear-reversal fabric evolution data from particle simulations. However, the generic blow-up we have seen raises doubts concerning the physical content of such a model.

These doubts are reinforced when we consider the post-reversal fabric evolution of a two-dimensional suspension. In two dimensions, the tensorial spherical harmonic expansion of $P(\boldsymbol{p})$ is (c.f. §4.5)

$$P(\boldsymbol{p}) = \frac{1}{2\pi}\left(1 + 4\boldsymbol{Q} : \boldsymbol{p}\boldsymbol{p} + \cdots\right). \tag{4.3.24}$$

We can adapt the three-dimensional rate-independent Hand model for simple shear to cover the two-dimensional case by enforcing the tracelessness condition for a two-dimensional fabric, $Q_+ \equiv 0$, in Eqs. 4.2.5 (see also §4.7 for a more rigorous

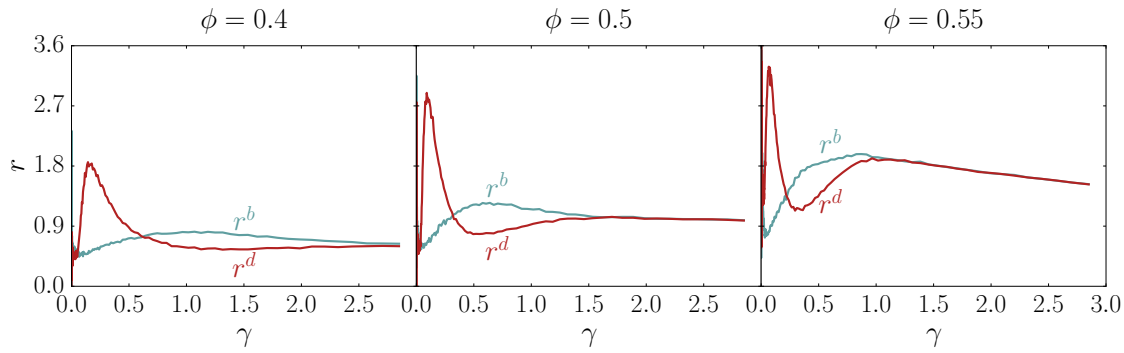

Figure 4.11: Simulation data for the fractional birth rate r^b (blue) and death rate r^d (red) against post-reversal strain for $\phi = 0.4$ (left), 0.5 (centre) and 0.55 (right).

derivation). The two-dimensional equivalent of Eqs. 4.2.5 is

$$\begin{aligned} \dot{Q}_- &= P_- \left[\mathrm{sgn}(\dot{\gamma})Q_{xy}, Q_-^2\right] Q_- + 2\,\mathrm{sgn}(\dot{\gamma})Q_{xy} \\ \dot{Q}_{xy} &= P_{xy} \left[\mathrm{sgn}(\dot{\gamma})Q_{xy}, Q_-^2\right] \mathrm{sgn}(\dot{\gamma}) - \frac{1}{2}\,\mathrm{sgn}(\dot{\gamma})Q_-, \end{aligned} \tag{4.3.25}$$

where $\boldsymbol{Q} := \langle \boldsymbol{pp} \rangle - \frac{1}{2}\boldsymbol{I}$ and P_- and P_{xy} are analytic in their arguments. We see that the linear criterion of Eq. 4.3.14 still holds.

We test such hand-type models against particle simulation data for shear reversal provided by Dr. Mari for a two-dimensional square monolayer of 4000 discs at area fractions $\phi = 0.65$, 0.7 and 0.75. The particles are bi-disperse with equal-area populations of radius 1 and 1.4. These simulations otherwise share the specifications of the three-dimensional simulations. The data presented here are averaged over 100 realisations.

The evolution of the independent components of $\boldsymbol{Q}$ are presented in Fig. 4.12. The qualitative similarities with the three-dimensional case presented in Fig. 4.4 are clear: Q_{xy} flips over a strain interval $\gamma \sim 1$ and overshoots its steady-state value, Q_{xx} is negative and has a post-reversal trough, and $|\boldsymbol{Q}|$ shrinks with increasing ϕ. We therefore expect the same underlying physics to determine the fabric evolution in both two and three dimensions. Since in two dimensions, tracelessness implies that $Q_- = 2Q_{xx}$, we already see that the data violate the criterion of Eq. 4.3.14, so cannot be fit by linear fabric models. We therefore instead consider the general

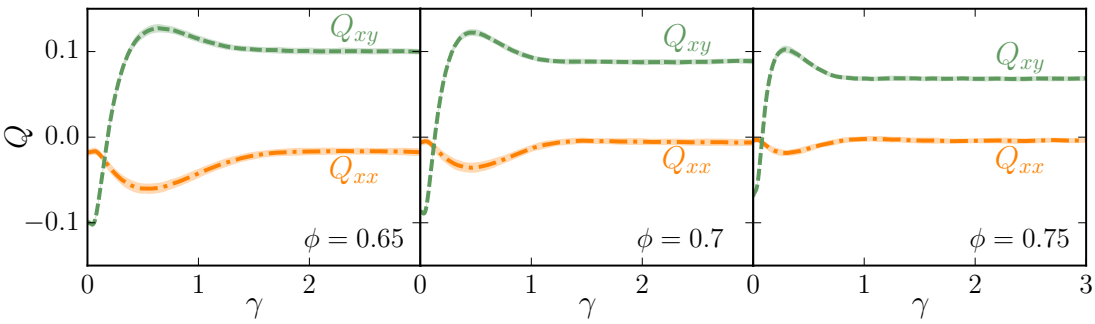

Figure 4.12: Shear-reversal data from particle simulations of a two-dimensional system at area fractions $\phi = 0.65$ (left), 0.7 (centre) and 0.75 (right) $\phi = 0.75$, with $\dot{\gamma} < 0$ for $\gamma < 0$ and $\dot{\gamma} > 0$ when $\gamma > 0$.

quadratic model, in which

$$\begin{aligned} P_- &= a_- + c_- \operatorname{sgn}(\dot{\gamma}) Q_{xy}, \\ P_{xy} &= a_{xy} + c_{xy} \operatorname{sgn}(\dot{\gamma}) Q_{xy} + e_{xy} Q_{xy}^2 + f_{xy} Q_-^2. \end{aligned} \tag{4.3.26}$$

This 6-parameter model is far more constrained than its 15-parameter three-dimensional counterpart, Eqs. 4.3.22. This model escapes the generic blow-up seen in three dimensions, and we are able to apply our linear-least-squares-plus-gradient-descent strategy to obtain fits to the particle simulation data, which we show in Fig. 4.13. We see that while the quadratic model is able to capture certain qualitative features, such as the existence of a trough in Q_- and, when $\phi > 0.65$, the overshoot in Q_{xy}, the fit is quantitatively poor. The trough in Q_- in particular is of the wrong amplitude and occurs at the wrong strain. This strongly suggests that the success of the three-dimensional quadratic model, Eqs. 4.3.23, does not reflect any physical mechanism whose effects might be contained within that model. Such a mechanism would be expected to apply equally well in two dimensions, particularly given the strong qualitative resemblance in the fabric evolution in the two- and three-dimensional cases. We instead conclude that the successful fits seen in Fig. 4.10 are due to the large number of free parameters in Eqs. 4.3.23.

We are able to obtain a near-quantitative fit for the two-dimensional data using

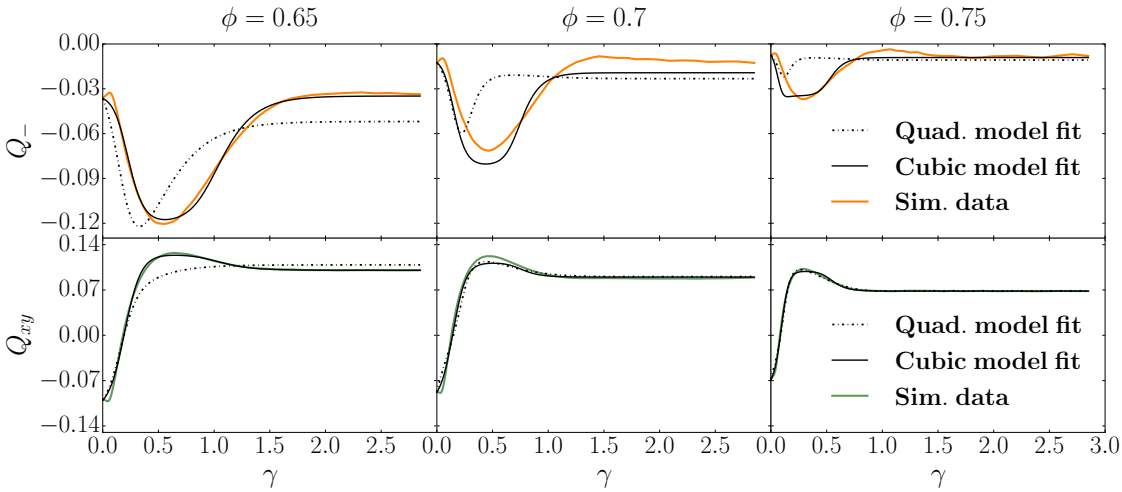

Figure 4.13: Fits to two-dimensional simulation data for shear reversal of the quadratic model described by Eqs. 4.3.26 and the cubic model described by Eqs. 4.3.27 for volume fractions $\phi = 0.65$ (left), 0.7 (centre) and 0.75 (right).

a cubic model,

$$\begin{aligned} P_- &= a_- + c_- \operatorname{sgn}(\dot{\gamma}) Q_{xy} + e_- Q_{xy}^2 + f_- Q_-^2, \\ P_{xy} &= a_{xy} + c_{xy} \operatorname{sgn}(\dot{\gamma}) Q_{xy} + e_{xy} Q_{xy}^2 + f_{xy} Q_-^2. \end{aligned} \tag{4.3.27}$$

(The model includes the cubic terms $e_- Q_{xy}^2 Q_-$ and $f_- Q_-^3$ once P_- and P_+ in Eqs. 4.3.25 are expanded according to Eqs. 4.3.27.) Even by setting terms in the general cubic model to zero, our previously-described approach to obtaining an initial set of parameter values inevitably leads to blow-up when we evolve the components of $\boldsymbol{Q}$ according to the model. This is because higher-order polynomials are even less confining than the quadratic model described by Eqs. 4.3.22. To fit Eqs. 4.3.27, we instead use the values of a_-, c_-, a_{xy}, c_{xy}, e_{xy} and f_{xy} obtained from linear least squares on the quadratic model described by Eqs. 4.3.26, and initially set the other parameters in Eqs. 4.3.27 to zero, to obtain an initial guess from which we launch a gradient descent. This process results in the cubic model fit shown in Fig. 4.13. While the fit is quantitatively good, clear evidence of overfitting is seen in the evolution of Q_- at $\phi = 0.75$, where kinks not present in the simulation data are seen in the cubic fit at strains $\gamma \approx 0.1$ and 0.5. This, and the generic blow-up, suggests that this cubic model does not provide us with any more physical insight than the quadratic model described by Eqs. 4.3.26.

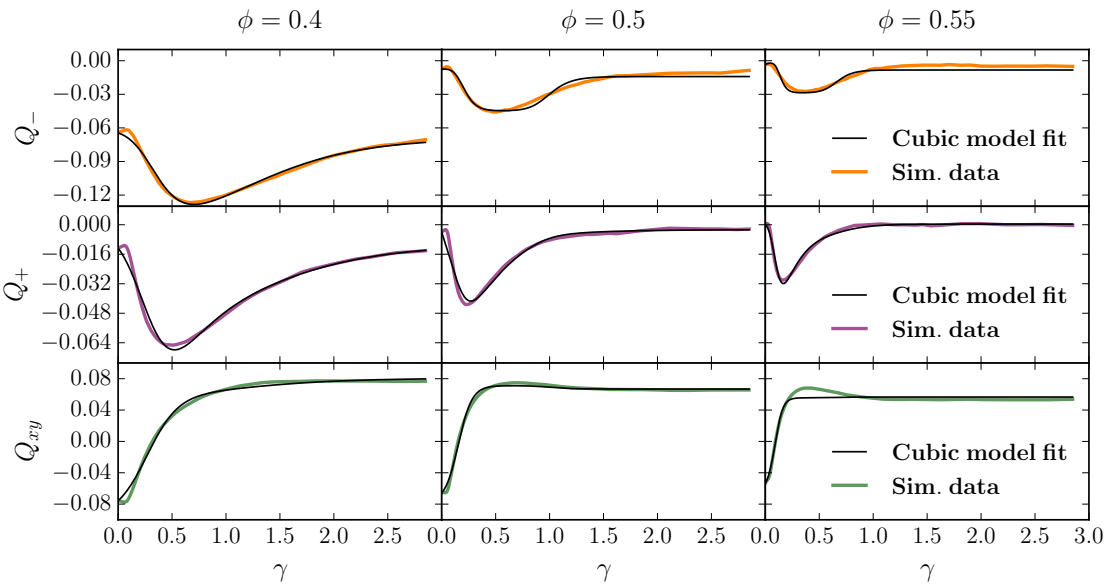

Figure 4.14: Fit to three-dimensional simulation data for shear reversal of the cubic model described by Eqs. 4.3.28 for volume fractions $\phi = 0.4$ (left), 0.5 (centre) and 0.55 (right).

We can nevertheless use Eqs. 4.3.27 to create a three-dimensional cubic model that is capable of quantitatively fitting the shear-reversal data from three-dimensional particle simulations, and that is also compatible with a two-dimensional counterpart which can fit data from two-dimensional simulations. We do this by supplementing the Q_- and Q_{xy} dynamics of Eqs. 4.3.27 with the Q_+ dynamics of Eqs. 4.3.23, resulting in the 12-parameter model with equations

$$\begin{aligned} P_- &= a_- + c_- \operatorname{sgn}(\dot{\gamma}) Q_{xy} + e_- Q_{xy}^2 + f_- Q_-^2, \\ P_+ &= a_+ + b_+ Q_+ + c_+ \operatorname{sgn}(\dot{\gamma}) Q_{xy} + e_+ Q_{xy}^2, \\ P_{xy} &= a_{xy} + c_{xy} \operatorname{sgn}(\dot{\gamma}) Q_{xy} + e_{xy} Q_{xy}^2 + f_{xy} Q_-^2. \end{aligned} \tag{4.3.28}$$

We fit this using the same methodology as was used to fit the two-dimensional cubic model, setting the same set of parameters to zero as in the two-dimensional case when using linear least squares and initiating our gradient descent. The result of this fit is shown in Fig. 4.14. Despite a decent quantitative agreement between our fit and the simulation data, we see the same signs of overfitting in the evolution of Q_- as in Fig. 4.13, and are unable to obtain overshoots in the Q_{xy} evolution of the size seen in the particle simulations. This model—which contains a large number of

free parameters, is highly susceptible to the divergence of fabric tensor components outside of a small range of parameter values, and shows qualitative evidence of overfitting (kinks in $Q_{-}(\gamma)$) while simultaneously struggling to capture qualitative features of the simulation data (the overshoot in $Q_{xy}(\gamma)$)—is unlikely to provide any physical insight.

4.4 Conclusion

In this chapter, we have looked at models that encode the microstructure into a symmetric second-rank fabric tensor $\boldsymbol{Q}$ whose evolution is prescribed by an ODE $\dot{\boldsymbol{Q}} = \boldsymbol{F}(\nabla \boldsymbol{v}, \boldsymbol{Q})$ for an analytic function $\boldsymbol{F}$ defined on a domain on which $\nabla \boldsymbol{v} \neq \boldsymbol{0}$. We have shown that no function $\boldsymbol{F}$ that is linear in the components of $\boldsymbol{Q}$ can possibly describe the fabric evolution under shear reversal. Quadratic models can fit the simulation data for a three-dimensional system, but fail in two dimensions despite the strong qualitative similarities in the fabric evolution in two and three dimensions. This suggests that the three-dimensional fit is due to the large number of fitting parameters in a three-dimensional quadratic model, and not any physical mechanism contained within the quadratic model. Fits to cubic models show signs of overfitting, while being highly non-confining for the components of $\boldsymbol{Q}$ when evolved over strain, problems that would get exacerbated with any higher-order polynomial model. We therefore conclude that any successful model for $\boldsymbol{Q}$ in dense non-Brownian suspensions must be of a different and more complicated form than many models seen for other non-Newtownian fluids [153, 184].

This chapter has also highlighted the component Q_{-} as a particularly challenging component to fit. In many models of polymer solutions or nematics [153], the non-solvent stress contains a term proportional to the conformation tensor. It might therefore not be a coincidence that the corresponding stress component, $N_1 = \Sigma_{xx} - \Sigma_{yy}$, has proved particularly challenging to accurately model, even in the steady state [112].

More fundamentally, this chapter has shown the importance of testing the assumptions of models against simulation or experimental data. Many fabric tensor

models of suspension rheology exist, including recent linear models [161,162], which model the evolution of the fabric tensor and then express the stress as a function of this fabric. However, these models are rarely tested against microstructural data, or even stress data for components other than the shear stress. Simulation data, such as those reported in this chapter, or experimental data, such as the detailed microstructural data collected by Deboeuf *et al.* [165], can directly assess the validity of the microstructural assumptions underpinning such models. It can also suggest a direction for future modelling efforts.

4.5 Appendix I: Tensorial spherical harmonic expansion

The tensorial spherical harmonic expansion of a scalar function $f(\boldsymbol{p})$, with $\boldsymbol{p}$ on the d-dimensional unit sphere, S^{d-1}, corresponds to a power series expansion

$$f(\boldsymbol{p}) = \frac{1}{A_d}\left(\alpha_0 + \sum_{k=1}^{\infty} \alpha_k^{i_1,i_2,\ldots,i_k} p_{i_1} p_{i_2} \cdots p_{i_k}\right), \tag{4.5.29}$$

where the $i_m \in \{1, 2, \cdots, d\}$ are component indices (e.g. $i_m \in \{x, y, z\}$ in three dimensions) that we are contracting over and A_d is the area of the d-dimensional unit sphere. The tensors $\boldsymbol{\alpha}_k$ are contracted over products of $\boldsymbol{p}$, and so should not have more independent components than the product with which they are contracted. This product is trivially symmetric under permutations of indices, so we require that the $\boldsymbol{\alpha}_k$ share this symmetry. Choosing a permutation of the indices of $\boldsymbol{\alpha}_k$ corresponds to choosing k indices out of a set of d symbols with replacement but without order. We furthermore have the constraint $\boldsymbol{p} \cdot \boldsymbol{p} = 1$, providing one constraining equation

$$p_{i_1} \cdots p_{i_{k-2}} p_j p_j = p_{i_1} \cdots p_{i_{k-2}}$$

per choice of $k-2$ indices out of d symbols with replacement without order. The kth order tensor in the expansion thus has $\binom{d+k-1}{k} - \binom{d+k-3}{k-2}$ independent components.

In two dimensions, this means two independent components for each k, whereas there are $2k+1$ independent components in three dimensions. There is therefore

a one-to-one correspondence between the kth order tensors in Eq. 4.5.29 and the the kth order coefficients in the Fourier series and spherical harmonic expansions in two and three dimensions respectively. Indeed, because $\sin k\theta$ and $\cos k\theta$ are sums of kth-degree mononomials in $\sin\theta$ and $\cos\theta$, the three-dimensional (scalar) real spherical harmonic expansion of f can be converted to tensorial expansions of the form of Eq. 4.5.29 by collecting into a tensor the coefficients of $p_x^k = \cos^k\theta\sin^k\phi$, $p_y^k = \sin^k\theta\sin^k\phi$, and $p_z^k = \cos^k\phi$ in the nth-order term of the expansion. In two dimensions, Fourier series coefficients can similarly be collected into tensors to get a tensorial expansion of the form of Eq. 4.5.29. Spherical harmonic expansions can be generalised to d-dimensions [185], so in principle one can calculate the d-dimensional tensorial spherical harmonic expansion on a case-by-case basis in this way for any d. It is, however, possible to calculate the d-dimensional spherical harmonic expansion directly. In this appendix, we do so for the expansion of $P(\boldsymbol{p})$ up to second order.

We consider a d-dimensional orientational distribution $P(\boldsymbol{p})$. We then assume that our tensors $\boldsymbol{\alpha}_k$ are defined such that the lth moment of P is independent of $\boldsymbol{\alpha}_k$ for any $k > l$. It is helpful at this point to define $\hat{P} := A_d\, P$ and $\langle\cdot\rangle_0 := \frac{1}{A_d}\int_{S^{d-1}}\cdot\mathrm{d}\Omega$.

It immediately follows that $\alpha_0 = 1$, since

$$1 = \int_{S^{d-1}} P\mathrm{d}\Omega = \left\langle \hat{P} \right\rangle_0 = \alpha_0,$$

where $\mathrm{d}\Omega$ is the area element on the d-dimensional sphere and where we have used the independence of the zeroth moment from higher-order α terms. Furthermore, because P is an orientational distribution, meaning $P(\boldsymbol{p}) = P(-\boldsymbol{p})$, all odd-order terms in the expansion must vanish, as well as all odd moments of P. The zeroth-order moment also gives us $\mathrm{Tr}[\boldsymbol{\alpha}_2] = 0$, since $\langle p_i p_j\rangle_0 = \frac{1}{d}\delta_{ij}$ and we must have $\boldsymbol{\alpha}_2 : \langle \boldsymbol{pp}\rangle_0 = 0$ to enforce the independence of $\left\langle \hat{P} \right\rangle_0$ from $\boldsymbol{\alpha}_2$.

In general, symmetry under permutation of indices and spherical symmetry implies that

$$\langle p_{i_1} p_{i_2} \dots p_{i_{2k}}\rangle_0 \propto \sum_{\sigma\in\mathcal{P}} \delta_{\sigma(i_1)\sigma(i_2)}\delta_{\sigma(i_3)\sigma(i_4)}\dots\delta_{\sigma(i_{2k-1})\sigma(i_{2k})} \tag{4.5.30}$$

where the sum is over distinct products of Kronecker deltas in which the indices $i_1, \dots, i_{2k}$ appear exactly once. There are $\left[\prod_{i=1}^{k}\binom{2j}{2}\right]/k!$ distinct products of Kronecker deltas ($\binom{2k}{2}$ choices of indices for the first Kronecker delta, $\binom{2k-2}{2}$ for the

second, etc., and then $k!$ ways of ordering k different Kronecker deltas). For $\langle \boldsymbol{pppp} \rangle_0$, this means three distinct products, so that

$$\langle p_{i_1} p_{i_2} p_{i_3} p_{i_4} \rangle_0 = \beta \left(\delta_{i_1 i_2} \delta_{i_3 i_4} + \delta_{i_1 i_3} \delta_{i_2 i_4} + \delta_{i_1 i_4} \delta_{i_2 i_3} \right) \tag{4.5.31}$$

for some coefficient β. We can obtain the value of β from

$$\begin{aligned}
\left\langle \left(\sum_{i=1}^{d} p_i p_i \right)^2 \right\rangle_0 &= 1 \\
&= \left\langle \sum_{i=1}^{d} p_i p_i p_i p_i + \sum_{i=0}^{d} \sum_{\substack{j=0 \\ j \neq i}}^{d} p_i p_i p_j p_j \right\rangle_0 \\
&= d \langle p_x p_x p_x p_x \rangle_0 + d (d-1) \langle p_x p_x p_y p_y \rangle_0 \\
&= 3\beta d + \beta d (d-1) \\
&= \beta d (d+2),
\end{aligned}$$

where the third line follows from the second after applying Eq. 4.5.31. We thus obtain

$$\beta = \frac{1}{d(d+2)}. \tag{4.5.32}$$

The second moment of the distribution gives us

$$\left\langle \boldsymbol{pp} \hat{P} \right\rangle_0 = \alpha_0 \langle \boldsymbol{pp} \rangle_0 + \langle \boldsymbol{pppp} \rangle_0 : \boldsymbol{\alpha}_2, \tag{4.5.33}$$

so that

$$\begin{aligned}
\left\langle \boldsymbol{pp} \hat{P} - \frac{1}{d} \boldsymbol{I} \right\rangle_0 &= \langle \boldsymbol{pppp} \rangle_0 : \boldsymbol{\alpha}_2 \\
&= \frac{1}{d(d+2)} \left(\delta_{ij} \delta_{kl} + \delta_{ik} \delta_{jl} + \delta_{il} \delta_{jk} \right) \alpha_2^{kl} \\
&= \frac{1}{d(d+2)} \left(\delta_{ij} \mathrm{Tr}[\boldsymbol{\alpha}_2] + \alpha_2^{ij} + \alpha_2^{ji} \right) \\
&= \frac{2}{d(d+2)} \alpha_2^{ij},
\end{aligned} \tag{4.5.34}$$

where we use the symmetry of $\boldsymbol{\alpha}_2$ under permutation of indices. Noting that $\left\langle \boldsymbol{pp} \hat{P} - \frac{1}{d} \boldsymbol{I} \right\rangle_0 = \boldsymbol{Q}$, we see that this yields Eq. 4.2.1.

4.6 Appendix II: Decomposition of the fabric evolution

The near-contact orientational distribution at a strain γ is defined as

$$P_\gamma(\boldsymbol{p}) = \frac{1}{N_\gamma} \sum_i \delta\left(\boldsymbol{p} - \boldsymbol{p}_i(\gamma)\right), \tag{4.6.35}$$

where the sum is over the N_γ near-contact orientations $\boldsymbol{p}_i(\gamma)$ at strain γ. Between any two successive strain steps γ and $\gamma + \mathrm{d}\gamma$, this distribution can evolve through three kinds of events. A near-contact may appear at strain $\gamma + \mathrm{d}\gamma$ that was not present at γ, a situation we refer to as a near-contact birth. Conversely, we also have near-contact deaths when near-contacts present at strain γ disappear by strain $\gamma + \mathrm{d}\gamma$. Finally, a near-contact may exist at both strains γ and $\gamma + \mathrm{d}\gamma$, having been advected by the flow in the interim. We can therefore write

$$\begin{aligned} P_{\gamma+\mathrm{d}\gamma}(\boldsymbol{p}) - P_\gamma(\boldsymbol{p}) = & \sum_{\text{advected}} \left[\frac{1}{N_{\gamma+\mathrm{d}\gamma}} \delta\left(\boldsymbol{p} - \boldsymbol{p}_i(\gamma + \mathrm{d}\gamma)\right) - \frac{1}{N_\gamma} \delta\left(\boldsymbol{p} - \boldsymbol{p}_i(\gamma)\right)\right] \\ & + \frac{1}{N_{\gamma+\mathrm{d}\gamma}} \sum_{\text{birth}} \delta\left(\boldsymbol{p} - \boldsymbol{p}_i(\gamma + \mathrm{d}\gamma)\right) - \frac{1}{N_\gamma} \sum_{\text{death}} \delta\left(\boldsymbol{p} - \boldsymbol{p}_i(\gamma)\right). \end{aligned} \tag{4.6.36}$$

Writing N^{b} and N^{d} for the number of near-contacts being born and dying across this strain interval respectively, we define

$$\dot{P}^{\mathrm{a}}(\boldsymbol{p}) := \frac{1}{\mathrm{d}\gamma} \left[\sum_{\text{advected}} \frac{1}{N_{\gamma+\mathrm{d}\gamma}} \delta\left(\boldsymbol{p} - \boldsymbol{p}_i(\gamma + \mathrm{d}\gamma)\right) - \frac{1}{N_\gamma} \delta\left(\boldsymbol{p} - \boldsymbol{p}_i(\gamma)\right)\right] \tag{4.6.37}$$

$$P^{\mathrm{b}}(\boldsymbol{p}) := \frac{1}{N^{\mathrm{b}}} \sum_{\text{birth}} \delta\left(\boldsymbol{p} - \boldsymbol{p}_i(\gamma + \mathrm{d}\gamma)\right) \tag{4.6.38}$$

$$P^{\mathrm{d}}(\boldsymbol{p}) := \frac{1}{N^{\mathrm{d}}} \sum_{\text{death}} \delta\left(\boldsymbol{p} - \boldsymbol{p}_i(\gamma)\right) \tag{4.6.39}$$

so that

$$\dot{P}_\gamma(\boldsymbol{p}) = \dot{P}^{\mathrm{a}}(\boldsymbol{p}) + r^{\mathrm{b}} P^{\mathrm{b}}(\boldsymbol{p}) - r^{\mathrm{d}} P^{\mathrm{d}}(\boldsymbol{p}), \tag{4.6.40}$$

where $r^{\mathrm{b}} := N_{\text{birth}}/(N_{\gamma+\mathrm{d}\gamma}\mathrm{d}\gamma)$ is the birth rate and $r^{\mathrm{d}} := N_{\text{death}}/(N_\gamma \mathrm{d}\gamma)$ is the death rate. This is Eq. 5.2.6 in the main text.

We obtain the corresponding decomposition of the fabric tensor $\boldsymbol{Q}$ by taking the traceless second moment of $\dot{P}^{\mathrm{a}}$, P^{b} and P^{d}:

$$\dot{\boldsymbol{Q}} = \dot{\boldsymbol{Q}}^{\mathrm{a}} + r^{\mathrm{b}} \boldsymbol{Q}^{\mathrm{b}}(\boldsymbol{p}) - \boldsymbol{Q}^{\mathrm{d}} P^{\mathrm{d}}(\boldsymbol{p}). \tag{4.6.41}$$

This is Eq. 4.3.21 in the main text.

4.7 Appendix III: Componentwise Hand equation

4.7.1 In three dimensions

We wish to simplify Eq. 4.2.4, removing any degeneracy in the equation. We first note that $\boldsymbol{Q}$ and $\hat{\boldsymbol{E}}$ are traceless in our system, due in the latter case to the incompressibility of our system. We therefore immediately find that $\hat{I}_1 = \hat{I}_4 = 0$. Furthermore, after reversing shear, $\hat{\boldsymbol{E}}$ doesn't change in our shear protocol. Consequently, neither do $\hat{I}_5$ and $\hat{I}_6$. They can therefore be absorbed into constant coefficients. Indeed, in our case of simple shear flow $\boldsymbol{v} = (\dot{\gamma}y, 0, 0)$ we have

$$\hat{\boldsymbol{E}}^2 \cdot \boldsymbol{Q} + \boldsymbol{Q} \cdot \hat{\boldsymbol{E}}^2 = \frac{1}{2}\boldsymbol{Q} + 2\hat{I}_9 \left(\boldsymbol{I} - 4\hat{\boldsymbol{E}}^2\right) \tag{4.7.42}$$

$$\hat{\boldsymbol{E}}^2 \cdot \boldsymbol{Q}^2 + \boldsymbol{Q}^2 \cdot \hat{\boldsymbol{E}}^2 = \frac{1}{2}\boldsymbol{Q}^2 - 8\hat{I}_9^2 \left(\boldsymbol{I} - 4\hat{\boldsymbol{E}}^2\right), \tag{4.7.43}$$

so the parameters α_7 and α_8 can be set to zero without any loss of generality.

The fabric tensor components Q_{xz} and Q_{yz} vanish due to $(x, y, z) \mapsto (-x, -y, z)$ symmetry. $\boldsymbol{Q}$ therefore has only three independent components, $Q_\pm := Q_{xx} \pm Q_{yy}$ and Q_{xy}. The Hand equation, Eq. 4.2.3, then yields

$$\dot{Q}_- = [\alpha_1 + \alpha_3 Q_+]\, Q_- + 2\,\mathrm{sgn}(\dot{\gamma}) Q_{xy}, \tag{4.7.44}$$

$$\begin{aligned}\dot{Q}_+ &= \frac{1}{6}\alpha_4 + \alpha_1 Q_+ + \frac{2}{3}\alpha_5\,\mathrm{sgn}(\dot{\gamma}) Q_{12} \\ &\quad + \alpha_3 \left(\frac{1}{6}Q_-^2 - \frac{1}{2}Q_+^2 + \frac{2}{3}Q_{12}^2\right) + \frac{2}{3}\alpha_6\,\mathrm{sgn}(\dot{\gamma}) Q_+ Q_{xy},\end{aligned} \tag{4.7.45}$$

$$\begin{aligned}\dot{Q}_{xy} &= \frac{1}{2}\alpha_2\,\mathrm{sgn}(\dot{\gamma}) - \frac{1}{2}\,\mathrm{sgn}(\dot{\gamma}) Q_- + \frac{1}{2}\alpha_5\,\mathrm{sgn}(\dot{\gamma}) Q_+ + \alpha_1 Q_{xy} \\ &\quad + \alpha_6\,\mathrm{sgn}(\dot{\gamma}) \left(\frac{1}{4}Q_-^2 + \frac{1}{4}Q_+^2 + Q_{xy}^2\right) + \alpha_3 Q_+ Q_{xy}.\end{aligned} \tag{4.7.46}$$

In our flow geometry,

$$\hat{I}_2 = \frac{1}{2}Q_-^2 + \frac{3}{2}Q_+^2 + 2Q_{xy}^2 \tag{4.7.47}$$

$$\hat{I}_3 = \frac{3}{4}Q_-^2 Q_+ - \frac{3}{4}Q_+^3 + 3Q_+ Q_{xy}^2 \tag{4.7.48}$$

$$\hat{I}_7 = \operatorname{sgn}(\dot{\gamma})Q_{xy} \tag{4.7.49}$$

$$\hat{I}_8 = \operatorname{sgn}(\dot{\gamma})Q_+ Q_{xy} \tag{4.7.50}$$

$$\hat{I}_9 = \frac{1}{4}Q_+ \tag{4.7.51}$$

$$\hat{I}_{10} = \frac{1}{8}Q_-^2 + \frac{1}{8}Q_+^2 + \frac{1}{2}Q_{xy}^2. \tag{4.7.52}$$

Since $\operatorname{sgn}(\dot{\gamma})Q_{xy} = \hat{I}_7$, $Q_+ = 4\hat{I}_9$ and $Q_-^2 = 8\hat{I}_{10} - \hat{I}_7^2 - 16\hat{I}_9^2$, we see that $\hat{I}_2$, $\hat{I}_3$ and $\hat{I}_8$ are polynomials in $\hat{I}_7$, $\hat{I}_9$ and $\hat{I}_{10}$, and that an analytic function in the invariants is really an analytic function in $\operatorname{sgn}(\dot{\gamma})Q_{xy}$, Q_+, and Q_-^2. It is thus clear that Eqs. 4.2.5 hold true.

The Hand equation, Eq. 4.2.3, does not constrain $\dot{Q}_-$, $\dot{Q}_+$, and $\dot{Q}_{xy}$ any further than Eqs. 4.2.5. To see this, consider Eq. 4.2.3 after enforcing tracelessness and proportionality to $\dot{\gamma}$:

$$\begin{aligned}\dot{\boldsymbol{Q}} = \hat{\boldsymbol{W}} \cdot \boldsymbol{Q} - \boldsymbol{Q} \cdot \hat{\boldsymbol{W}} + \beta_1 \boldsymbol{Q} + 2\left(\beta_2 - \beta_1 \hat{I}_7\right)\hat{\boldsymbol{E}} \\ + 6\left(\beta_4 - 4\beta_1 \hat{I}_9\right)\hat{\boldsymbol{E}}^2 - 2\left(\beta_4 - 4\beta_1 \hat{I}_9\right)\hat{I}_5 \boldsymbol{I},\end{aligned}$$

corresponding in our case to the coupled system

$$\dot{Q}_- = \beta_1 Q_- + 2\operatorname{sgn}(\dot{\gamma})Q_{12}, \tag{4.7.53}$$

$$\dot{Q}_+ = \beta_4, \tag{4.7.54}$$

$$\dot{Q}_{xy} = \beta_2 \operatorname{sgn}(\dot{\gamma}) - \frac{1}{2}\operatorname{sgn}(\dot{\gamma})Q_-. \tag{4.7.55}$$

We have previously established that the only constraint the Hand equation imposes on the tensor coefficients β_i is that they are are analytic functions (except at $\dot{\gamma} = 0$) of $\operatorname{sgn}(\dot{\gamma})Q_{12}$, Q_+ and Q_-^2. We therefore conclude that Eqs. 4.2.5 are the most general allowed in three dimensions.

4.7.2 In two dimensions

In two dimensions, the tensorial second-order spherical harmonic expansion (in this case a Fourier series expansion) of a probability density $P(\boldsymbol{p})$ for pairs with centre-to-centre orientation $\boldsymbol{p}$ is

$$P(\boldsymbol{p}) \approx \frac{1}{2\pi}\left(1 + 4\boldsymbol{Q} : \boldsymbol{p}\boldsymbol{p}\right), \tag{4.7.56}$$

where $\boldsymbol{Q} \equiv \langle \boldsymbol{p}\boldsymbol{p} \rangle - \frac{1}{2}\boldsymbol{I}$.

We need to re-derive the Hand equation Eq. 4.2.3 in two dimensions. We first note that the result from frame-indifference [37],

$$\dot{\boldsymbol{Q}} = \boldsymbol{W} \cdot \boldsymbol{Q} - \boldsymbol{Q} \cdot \boldsymbol{W} + \mathbb{F}\left(\boldsymbol{Q}, \boldsymbol{E}\right), \tag{4.7.57}$$

holds in two dimensions as it does in three. The two-dimensional case can therefore be seen as a special case of the three-dimensional case with the axis of the rigid rotation along the vorticity axis.

From equation (8.13) of Rivlin [179] (after applying equation (4.7)), any polynomial in symmetric 2×2 tensors $\boldsymbol{A}$ and $\boldsymbol{B}$ can be written in the form

$$\varphi_0 \boldsymbol{I} + \varphi_1 \boldsymbol{A} + \varphi_2 \boldsymbol{B}, \tag{4.7.58}$$

where the φ_i are polynomials in the invariants (see paragraph in Rivlin [179] below Eq. 13.3) $\mathrm{Tr}\boldsymbol{A}$, $\mathrm{Tr}\boldsymbol{B}$, $\mathrm{Tr}\boldsymbol{A}^2$, $\mathrm{Tr}\boldsymbol{B}^2$, and $\mathrm{Tr}\boldsymbol{A} \cdot \boldsymbol{B}$.

The rate-independent two-dimensional Hand equation for $\boldsymbol{Q}$ is therefore

$$\dot{\boldsymbol{Q}} = \hat{\boldsymbol{W}} \cdot \boldsymbol{Q} - \boldsymbol{Q} \cdot \hat{\boldsymbol{W}} + \alpha_1 \boldsymbol{Q} + \alpha_2 \hat{\boldsymbol{E}}, \tag{4.7.59}$$

or in component form,

$$\begin{aligned} \dot{Q}_- &= \alpha_1 Q_- + 2\,\mathrm{sgn}(\dot{\gamma}) Q_{12} \\ \dot{Q}_{xy} &= \frac{1}{2}\,\mathrm{sgn}(\dot{\gamma})\alpha_2 - \frac{1}{2}\,\mathrm{sgn}(\dot{\gamma}) Q_- + \alpha_1 Q_{xy}, \end{aligned} \tag{4.7.60}$$

with the α_i analytic functions of the invariants $\hat{I}_1 \equiv \mathrm{Tr}(\boldsymbol{Q})$, $\hat{I}_2 \equiv \mathrm{Tr}(\boldsymbol{Q}^2)$, $\hat{I}_4 \equiv \mathrm{Tr}(\hat{\boldsymbol{E}})$, $\hat{I}_5 \equiv \mathrm{Tr}(\hat{\boldsymbol{E}}^2)$, and $\hat{I}_7 \equiv \mathrm{Tr}(\boldsymbol{Q} \cdot \hat{\boldsymbol{E}})$ (The labelling here is chosen so as to be consistent with the three-dimensional case.)

For an incompressible shear flow in two dimensions $\boldsymbol{v} = (\dot{\gamma}y, 0)$, the invariants are

$$\hat{I}_1 = 0, \tag{4.7.61}$$

$$\hat{I}_2 = \frac{1}{2}Q_-^2 + 2Q_{12}^2, \tag{4.7.62}$$

$$\hat{I}_4 = 0, \tag{4.7.63}$$

$$\hat{I}_5 = \frac{1}{2}, \tag{4.7.64}$$

$$\hat{I}_7 = \operatorname{sgn}(\dot{\gamma})Q_{12}. \tag{4.7.65}$$

An analytical function of the invariants is therefore an analytical function of $\operatorname{sgn}(\dot{\gamma})Q_{xy}$ and Q_-^2, so that the most general form of the two-dimensional Hand equation for our system is

$$\dot{Q}_- = P_- \left[\operatorname{sgn}(\dot{\gamma})Q_{xy}, Q_-^2\right] Q_- + 2\operatorname{sgn}(\dot{\gamma})Q_{xy}, \tag{4.7.66}$$

$$\dot{Q}_{xy} = P_{xy} \left[\operatorname{sgn}(\dot{\gamma})Q_{xy}, Q_-^2\right] - \frac{1}{2}\operatorname{sgn}(\dot{\gamma})Q_-, \tag{4.7.67}$$

where the P_{ij} are analytical functions of their arguments.

Chapter 5

Fabric tensor dynamics of dense non-Brownian suspensions: microstructural insights

5.1 Introduction

In the previous chapter, we considered phenomenological models for the microstructural evolution of dense, athermal suspensions of hard spheres. (See previous chapter for precise definitions and specifications.) Adopting a widespread approach, we chose a "fabric tensor" $\boldsymbol{Q}$, the de-traced second moment of the orientational distribution of near-contacts, to represent the microstructure. We then explored models in which $\dot{\boldsymbol{Q}}$ is a polynomial in the components of $\boldsymbol{Q}$ and of the velocity gradient tensor, $\nabla \boldsymbol{v}$. Linear models, we discovered, cannot fit data from particle simulations of a suspension under shear reversal. We found that higher-order polynomials can fit the data, but in each case also found evidence that fits are a consequence of having many free parameters, and not of any physical mechanism contained within the equations of the model.

In this chapter, we look into why the approach of the previous chapter fails, challenging the fundamental assumptions inherent in fabric tensor models of suspension microstructure. The key assumption is that $\boldsymbol{Q}$ contains enough microstructural information to assume the role of structure tensor, i.e., for $\boldsymbol{Q}$ to serve as a proxy for the

full particle configuration when describing microstructure-dependent material variables. This includes $\boldsymbol{Q}$'s own evolution: we are assuming that $\dot{\boldsymbol{Q}}$ can be expressed as a function of $\boldsymbol{Q}$ and $\nabla\boldsymbol{v}$. If, for instance, higher-order terms in the spherical harmonic expansion of $P(\boldsymbol{p})$, or radial information in the pair distribution $g(\boldsymbol{r})$, have a significant impact on the rheology that cannot be modelled as a function of $\boldsymbol{Q}$ and $\nabla\boldsymbol{v}$, this assumption will not hold.

5.2 Lobality

It is therefore instructive to ask ourselves how good a description $\boldsymbol{Q}$ is of $P(\boldsymbol{p})$. Specifically, how valid is the approximation (c.f. Eq. 4.2.1)

$$P(\boldsymbol{p}) \approx \frac{1}{4\pi}\left(1 + \frac{15}{2}\boldsymbol{Q} : \boldsymbol{pp}\right)? \tag{5.2.1}$$

If this approximation were poor, it would imply that some coefficients of higher-order terms in the spherical harmonic expansion have a significant magnitude relative to that of the second-order term, $\frac{15}{2}\boldsymbol{Q}$. It would then be unlikely that these large higher-order terms, and their effects on the suspension rheology, can be expressed as a function of a comparatively diminutive $\boldsymbol{Q}$.

To assess this, we consider the spherical harmonic expansion of $P(\boldsymbol{p})$ up to fourth order [178],

$$P(\boldsymbol{p}) \approx \frac{1}{4\pi}\left(1 + \frac{15}{2}\boldsymbol{Q} : \boldsymbol{pp} + \frac{315}{8}\boldsymbol{C} :: \boldsymbol{pppp}\right). \tag{5.2.2}$$

Here, the rank-4 tensor $\boldsymbol{C}$ has components

$$C_{ijkl} = \langle p_i p_j p_k p_l \rangle - \frac{1}{7}H_{ijkl} + \frac{1}{35}I_{ijkl}, \tag{5.2.3}$$

where

$$H_{ijkl} = \langle p_i p_j \rangle \delta_{kl} + \langle p_i p_k \rangle \delta_{jl} + \langle p_i p_l \rangle \delta_{jk} + \delta_{ij}\langle p_k p_l \rangle + \delta_{ik}\langle p_j p_l \rangle + \delta_{il}\langle p_j p_k \rangle \tag{5.2.4}$$

$$I_{ijkl} = \delta_{ij}\delta_{kl} + \delta_{ik}\delta_{jl} + \delta_{il}\delta_{jk}. \tag{5.2.5}$$

We can quantify the relative contributions of the second- and fourth-order terms by comparing the largest eigenvalue, Λ_2, of $\frac{15}{2}\boldsymbol{Q}$ with that of $\frac{315}{8}\boldsymbol{C}$, Λ_4. (See the paper by Qi [186] for a reference on the eigenvalues of fully symmetric high-order tensors).

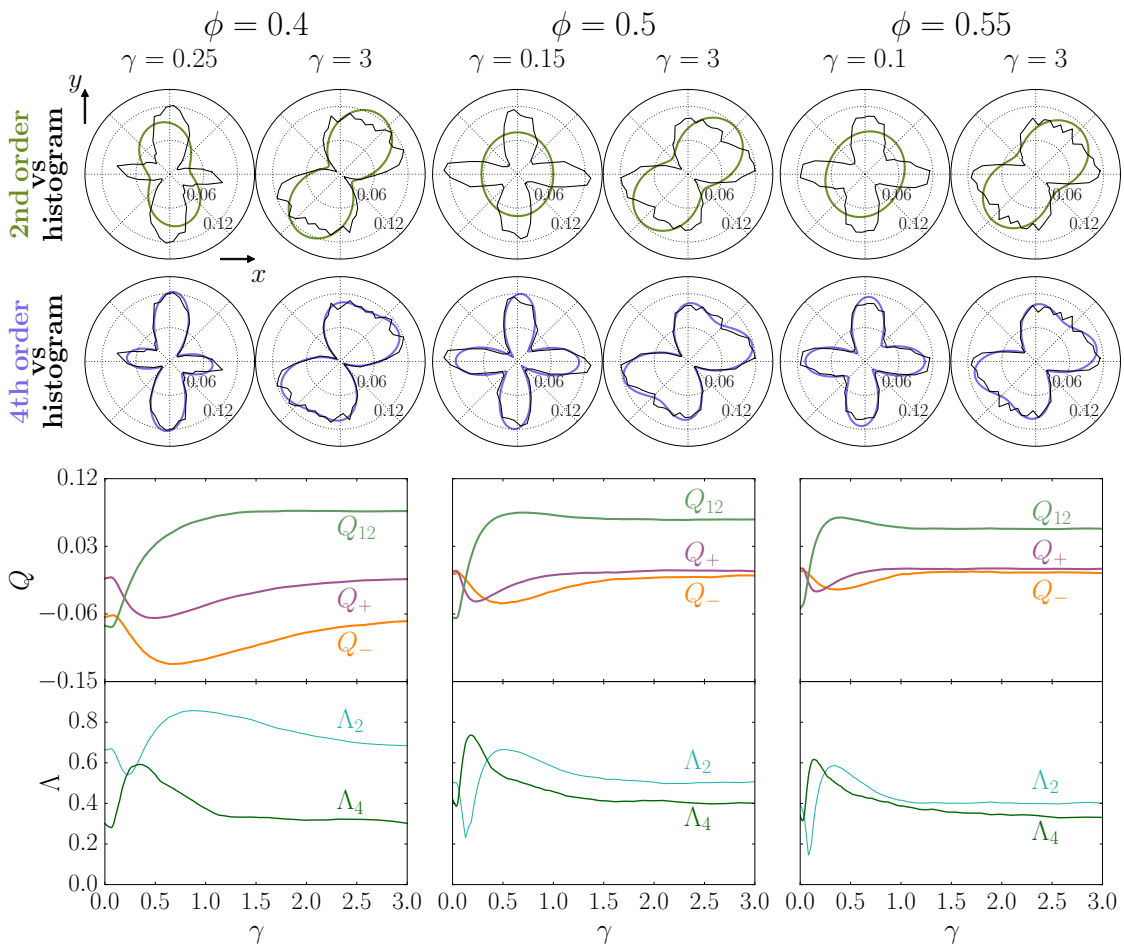

Figure 5.1: Top two rows: Snapshots of $P(\boldsymbol{p})$ and the second- (top row) and fourth-order (second row) spherical harmonic approximations of it during numerical simulations of shear reversal for volume fractions $\phi = 0.4$ (left), $\phi = 0.5$ (centre), and $\phi = 0.55$ (right). Third row: components of $\boldsymbol{Q}$ across reversal from these simulations. Fourth row: Largest eigenvalues Λ_2 and Λ_4 of resp. the second-rank $\boldsymbol{Q}$ and the fourth-rank $\boldsymbol{C}$ (see main text for the definition) spherical harmonic contributions to $P(\boldsymbol{p})$.

In the bottom row of Fig. 5.1, we show the time evolution of these eigenvalues under shear reversal for volume fractions $\phi = 0.4$, 0.5 and 0.55. In each case, we see strain intervals across which $\Lambda_4 > \Lambda_2$. Furthermore, Λ_2 and Λ_4 are of the same magnitude throughout the evolution, including at steady-state. The top two rows of Fig. 5.1 show polar plots of the shear-plane cross-section of $P(\boldsymbol{p})$ (black) at the strain, γ, which maximises $\Lambda_4 - \Lambda_2$ and at steady-state, $\gamma = 3$, for the same three volume fractions. We compare each of these with a plot of the second-order expansion, Eq. 5.2.1 (top row, green), and a plot of the fourth-order expansion, Eq. 5.2.2. We see that $P(\boldsymbol{p})$ deviates little from its expansion up to fourth order, but is poorly captured by its expansion up to second-order. This is particularly true shortly after reversal, when Λ_2 takes its smallest values, and the shear-plane cross-section of $P(\boldsymbol{p})$ is seen to take on a distinctly four-lobed structure. The ratio Λ_4/Λ_2 can be thought of as quantifying to what extent $P(\boldsymbol{p})$ is four-lobed, rather than two-lobed, in the shear plane.

The large four-lobed component of $P(\boldsymbol{p})$ strongly suggests that a constitutive model based on a closed ODE for the evolution of $\boldsymbol{Q}$ under flow cannot capture the physics of near-contact network reconstruction after shear reversal. This is one of the key outcomes of our analysis: a closed second-rank fabric evolution model, even if it leads to good fits to simulation data, will necessarily evolve the fabric according to the second-order expansion of the pair distribution, which we have shown in Fig. 5.1 to be subdominant. Indeed, where $\Lambda_4 > \Lambda_2$, we see that the principal shear-plane axis of the second-order expansion is not a maximum of $P(\boldsymbol{p})$ in this plane.

The rate of change of the pair distribution function, $\dot{P}(\boldsymbol{p})$, further reinforces the view that four-lobed structures play an important role in the evolution of the microstructure. As with $\boldsymbol{Q}$, we can decompose $\dot{P}$ into advective, birth and death contributions,

$$\dot{P}(\boldsymbol{p}) = \dot{P}^{\mathrm{a}}(\boldsymbol{p}) + r^{\mathrm{b}} P^{\mathrm{b}}(\boldsymbol{p}) - r^{\mathrm{d}} P^{\mathrm{d}}(\boldsymbol{p}), \tag{5.2.6}$$

by considering the evolution of the number of near-contacts in a surface element on the unit sphere (see §4.6 for a derivation). This allows us to separately assess the "lobality" of the evolutionary mechanisms of advection, birth and death. The distribution of orientations of near-contact births, $P^{\mathrm{b}}(\boldsymbol{p})$, and deaths, $P^{\mathrm{d}}(\boldsymbol{p})$, are

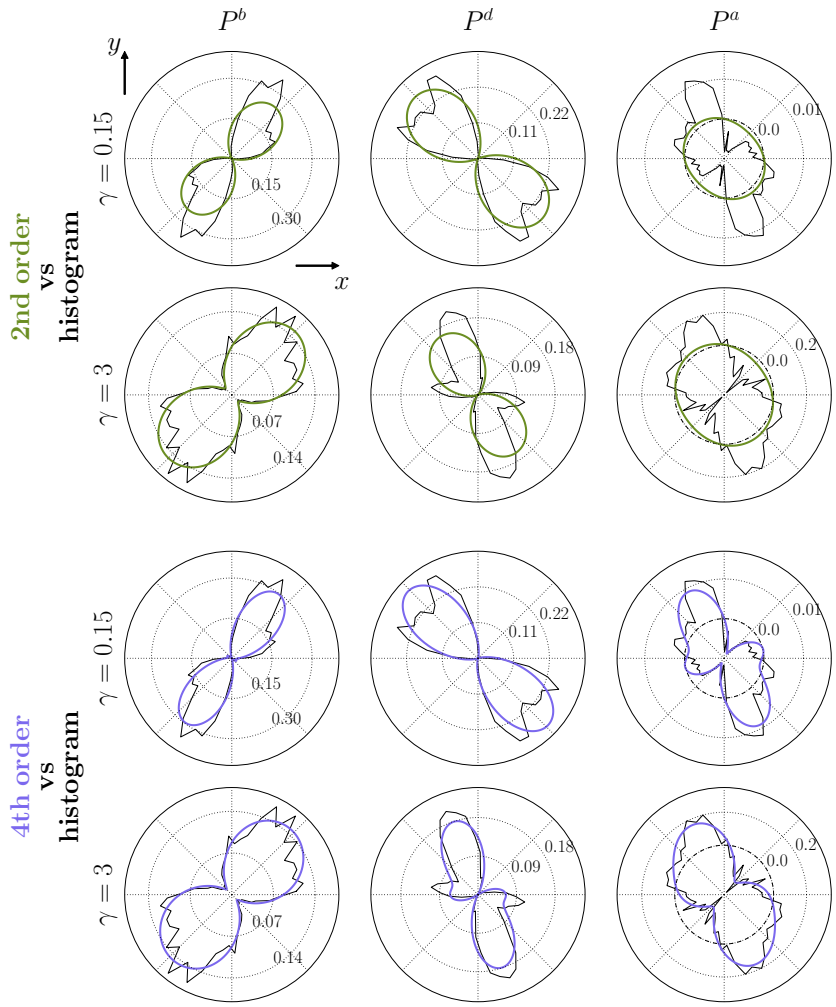

Figure 5.2: Top two rows: Polar plots of simulation data for $P^{\mathrm{b}}(\boldsymbol{p})$ (left), $P^{\mathrm{d}}(\boldsymbol{p})$ (centre) and $\dot{P}^{\mathrm{a}}(\boldsymbol{p})$ (right), as defined in Eq. 5.2.6, in the shear plane for $\phi = 0.5$ and for $\gamma = 0.15$ (top) and $\gamma = 3$ (centre), in black lines. These are compared to their second-order spherical harmonic approximations (color lines). Bottom two rows: Same $\dot{P}^{\mathrm{a}}(\boldsymbol{p})$, $P^{\mathrm{b}}(\boldsymbol{p})$ and $P^{\mathrm{d}}(\boldsymbol{p})$ data (black lines), compared to their and fourth-order spherical harmonic approximations (color lines).

positive quantities by definition. By contrast, the advective contribution, $\dot{P}^{\mathrm{a}}(\boldsymbol{p})$, will in general take positive and negative values for different $\boldsymbol{p}$. In Fig. 5.2, we show the values of $\dot{P}^{\mathrm{a}}(\boldsymbol{p})$, $P^{\mathrm{b}}(\boldsymbol{p})$ and $P^{\mathrm{d}}(\boldsymbol{p})$ along the shear plane for $\phi = 0.5$ at strains $\gamma = 0.15$ and $\gamma = 3$ (as in Fig. 5.1), alongside their second- and fourth-order spherical harmonic approximations. (The corresponding plots for $\phi = 0.4$ and $\phi = 0.55$ show similar features, and are shown in Appendix 5.4.)

Though none of these distributions, except $P^{\mathrm{d}}(\boldsymbol{p})$ at $\gamma = 3$, shows a marked four-lobed structure, this data is consistent with the four-lobed structure of $P(\boldsymbol{p})$ shortly after reversal; it is enough that the contributions to $\dot{P}(\boldsymbol{p})$ create and destroy near-contacts along different directions to get a $P(\boldsymbol{p})$ with more than two maxima in the shear plane. Moreover, the top rows of Fig. 5.2 show that key features of $P^{\mathrm{b}}(\boldsymbol{p})$, $P^{\mathrm{d}}(\boldsymbol{p})$ and $\dot{P}^{\mathrm{a}}(\boldsymbol{p})$ are not captured in the second-order spherical harmonic approximation of these quantities. Indeed, the second-order approximations correspond most poorly to the full distributions when these contributions take large amplitudes in the shear plane relative to the amplitudes of the other contributions. This occurs at early strains for $P^{\mathrm{b}}(\boldsymbol{p})$ and large strains for $P^{\mathrm{d}}(\boldsymbol{p})$ and $\dot{P}^{\mathrm{a}}(\boldsymbol{p})$.

The simulation data for $P(\boldsymbol{p})$ and $\dot{P}(\boldsymbol{p})$ therefore lead us to the unavoidable conclusion that the structure of the orientational distribution of near-contacts can only be captured by a spherical harmonic expansion of up to at least fourth order. The fabric evolution cannot be expressed in terms of only the flow and $\boldsymbol{Q}$ itself, since it depends on a microstructure which contains information from the fourth-rank tensor $\boldsymbol{C}$ in a way that cannot be approximated by an adequate closure. Such a closure would have to express $\boldsymbol{C}$ in terms of $\boldsymbol{Q}$ resulting in a two lobed outcome.

5.2.1 Bingham distributions

The success of the fourth-order spherical harmonic expansion in approximating $P(\boldsymbol{p})$ throughout its post-reversal evolution, as seen in Fig. 5.1, suggests that while $\boldsymbol{Q}$ is an inadequate description of the microstructure, a successful strategy might be to model evolution of both $\boldsymbol{Q}$ and $\boldsymbol{C}$ as functions of each other. Now, tracelessness and symmetry under permutations of indices leaves $\boldsymbol{C}$ with nine independent components (see §4.5), out of which four, e.g. C_{xzzz}, C_{yzzz}, C_{xxxz} and C_{yyyz}, must vanish due

to the $(x, y) \mapsto (-x, -y)$ symmetry of our system. It is therefore clear that an approach like that used in the previous chapter, expressing the fabric evolution as a polynomial in the three independent components of $\boldsymbol{Q}$ and five independent components of $\boldsymbol{C}$, would lead to a prohibitive proliferation of free parameters, even for low-order polynomial models.

A different approach to modelling the evolution of $\boldsymbol{Q}$ and $\boldsymbol{C}$ is therefore needed. An alternative and more explicit characterisation of the many-lobed nature of the distribution, using Bingham distributions [187], may prove useful in this context. Bingham distributions are antipodal distributions

$$f(\boldsymbol{p}) \propto e^{\boldsymbol{T}:\boldsymbol{p}\boldsymbol{p}}, \tag{5.2.7}$$

where $\boldsymbol{T}$ is a symmetric and (without loss of generality) traceless tensor. Expanding $\boldsymbol{T}$ as a function of its orthonormal eigenvectors,

$$\boldsymbol{T} = \left(\kappa - \frac{1}{2}\lambda\right) \boldsymbol{p}_{\parallel}\boldsymbol{p}_{\parallel} + \left(-\kappa - \frac{1}{2}\lambda\right) \boldsymbol{p}_{\perp}\boldsymbol{p}_{\perp} + \lambda\, \hat{\boldsymbol{z}}\hat{\boldsymbol{z}},$$

with the last term due to the $z \mapsto -z$ symmetry of our system, and where

$$\begin{aligned} \boldsymbol{p}_{\parallel} &= (\cos\mu, \sin\mu, 0) \\ \boldsymbol{p}_{\perp} &= (-\sin\mu, \cos\mu, 0) \\ \hat{\boldsymbol{z}} &= (0, 0, 1)\,, \end{aligned}$$

we see that if $\boldsymbol{p} = (\cos\theta\sin\phi, \sin\theta\sin\phi, \cos\phi)$, then

$$f(\boldsymbol{p}) = \frac{1}{Z} e^{\kappa\cos[2(\theta-\mu)]\sin^2\phi + \frac{3}{4}\lambda\cos 2\phi}. \tag{5.2.8}$$

The normalisation factor here is

$$Z(\kappa, \lambda) = 2\pi \int_0^{\pi} I_0\left(\kappa\sin^2\phi\right) e^{\frac{3}{4}\lambda\cos 2\phi} \sin\phi\, \mathrm{d}\phi, \tag{5.2.9}$$

where $I_n(x) := \pi^{-1}\int_0^{\pi} e^{x\cos\theta}\cos n\theta\, \mathrm{d}\theta$ is the modified Bessel function of order n. This form corresponds in two dimensions to the von Mises distribution [188] on the half-circle, and gives us explicit control over the width and orientation of this two-lobed distribution via the parameters κ and μ. Defining $g(\theta, \phi; \mu, \kappa, \lambda)$ as the right-hand-side of Eq. 5.2.8, we may then construct a four-lobed distribution

$$g_2(\theta, \phi; R, \mu_1, \kappa_1, \lambda_1, \mu_2, \kappa_2, \lambda_2) := \frac{1}{1+R}\left[g(\theta, \phi; \mu_1, \kappa_1, \lambda_1) + R\, g(\theta, \phi; \mu_2, \kappa_2, \lambda_2)\right]. \tag{5.2.10}$$

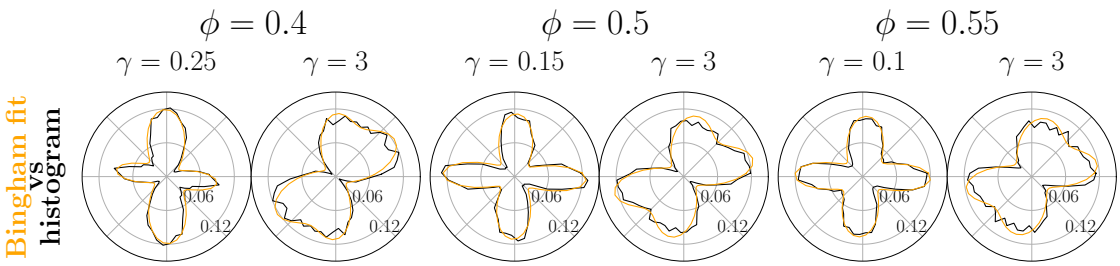

Figure 5.3: Snapshots of $P(\boldsymbol{p})$ (black) and fits of the bi-lobed Bingham distribution g_2 to $P(\boldsymbol{p})$ (orange) during numerical simulations of shear reversal for volume fractions $\phi = 0.4$ (left), $\phi = 0.5$ (centre), and $\phi = 0.55$ (right).

We illustrate this in Fig. 5.3, where we show fits of g_2 to the snapshots of Fig. 5.1, obtained by the minimising squared difference between g_2 and the snapshot, using an initial parameter set $(R, \mu_1, \kappa_1, \lambda_1, \mu_2, \kappa_2, \lambda_2) = \left(1, 0, 1, -1, \frac{\pi}{2}, 1, -1\right)$. We plot the resulting best-fit parameters in Table 5.2.1. We see that both shortly after reversal and at steady state, $P(\boldsymbol{p})$ is well described by a bi-lobed Bingham distribution. The three volume fractions show similar trends for the fit parameters shortly after reversal and, with the exception of $\phi = 0.4$, at steady state. This suggests that the Bingham fit parameters may highlight important physics, such as the importance of the flow and gradient directions: we see that one lobe is consistently roughly along the flow direction, $\mu_1 \approx 0$, and the other roughly along the gradient direction, $\mu_2 \approx \frac{\pi}{2} \approx 1.57$.

Choosing parameters such that $g_2(\boldsymbol{p}) \approx P(\boldsymbol{p})$, we can then express the second and fourth moments of the distribution, and hence $\boldsymbol{Q}$ and $\boldsymbol{C}$, as a function of these parameters. The four-lobed Bingham distribution thus provides us with a path to $\boldsymbol{Q}$ and $\boldsymbol{C}$ from an explicit specification of the angles and breadth of the lobes of $P(\boldsymbol{p})$. The function g_2 also has the advantage of describing a four-lobed distribution in terms of seven parameters, one fewer than the eight quantities needed to specify $\boldsymbol{Q}$ and $\boldsymbol{C}$. While a model explicitly couched in terms of angles μ_1 and μ_2 would violate frame indifference, Bingham distributions may prove useful in translating an intuition for the directions in which different mechanisms, such as the birth and death of contacts, affect the microstructure into a model for $\boldsymbol{Q}$ and $\boldsymbol{C}$.

ϕ	0.4	0.4	0.5	0.5	0.55	0.55
γ	0.25	3	0.15	3	0.1	3
R	3.54	1.25	2.08	1.99	2.19	2.84
μ_1	-0.123	0.016	-0.0437	0.211	-0.0265	0.149
κ_1	3.73	-1.69	3.47	2.31	3.08	2.46
λ_1	1.90	0.671	1.60	0.678	1.34	0.696
μ_2	1.59	0.525	1.54	1.36	1.50	1.32
κ_2	1.18	1.38	1.27	0.996	1.05	0.752
λ_2	0.666	0.368	0.649	0.320	0.456	0.204

Table 5.1: Best-fit parameters for the bi-lobed Bingham distribution, g_2, to the snapshots of $P(\boldsymbol{p})$ from Fig. 5.1.

5.3 Conclusion

In this section, we have tested the validity of two of the main assumptions on which fabric tensor models of suspensions, studied in the previous chapter, are based. We have shown that the orientational distribution of near-contacts (responsible for stress generation) $P(\boldsymbol{p})$, as well as its time derivative, strongly depart from the two-lobed structures that can be directly described by a second-rank tensor. The fabric tensor $\boldsymbol{Q}$ is thus neither an adequate description of $P(\boldsymbol{p})$, nor does it contain the microstrucutral information needed to inform its evolution via $\dot{P}(\boldsymbol{p})$. Indeed, our investigation shows that *no* symmetric second-rank tensor, which would necessarily have orthonormal eigenvectors, can adequately represent $P(\boldsymbol{p})$. This is particularly evident shortly after reversal during which period $P(\boldsymbol{p})$ has a highly four-lobed structure, and the fourth-order term in its spherical harmonic expansion is dominant.

On the other hand, we have also shown that $P(\boldsymbol{p})$ and the contributions to $\dot{P}(\boldsymbol{p})$ are well described by their spherical harmonic expansions up to fourth order. This suggests that they can be successfully modelled by introducing the fourth-rank tensor $\boldsymbol{C}$, defined in Eq. (5.2.2), explicitly. One might then consider developing Hand-type models for $\boldsymbol{Q}$ and $\boldsymbol{C}$, though polynomials in the eight independent components of $\boldsymbol{Q}$ and $\boldsymbol{C}$ would result in a very large number of free parameters, even

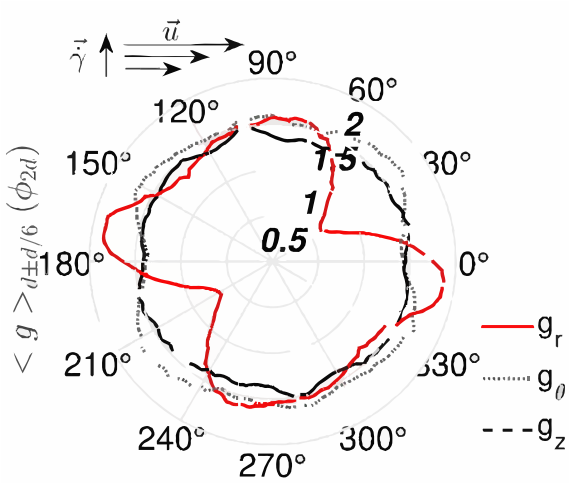

Figure 5.4: Microstructural data from Deboeuf *et al.* [165] for a suspension of non-Brownian particles in a yield stress suspending fluid under shear. Red data shows the shear plane.

at low polynomial order.

One might alternatively attempt to base a model on a simplified micromechanical 'kinetic' theory, including only the terms suggested by that theory. This may have the added benefit of avoiding the generic blowups seen in the non-linear polynomial models explored in the previous chapter, since a judicious kinetic theory would be expected to map onto parameters within a stable basin of attraction. Four-lobed Bingham distributions could then serve as an aid in obtaining from such a theory the fourth-order spherical harmonic terms that, as we have shown in this chapter, are significant in the post-reversal microstructural evolution.

If the previous chapter showed the value of particle simulations against which models may be tested, this chapter has highlighted their explorative value. Using Dr. Mari's simulation data, we were able to directly consider $P(\boldsymbol{p})$, and, via $\dot{P}(\boldsymbol{p})$, the mechanisms through which $P(\boldsymbol{p})$ evolves.

Further physical insight might be gained by simulating suspensions in other flow geometries, such as extensional flow [126, 127]. It would also, again, be beneficial to validate the conclusions of this study against experimental data for shear reversal. Encouragingly, the steady-state microstructure observed by Deboeuf *et al.* [165] for a suspension under shear, shown in Fig. 5.4, shows a striking resemblance to the

steady-state data we show in Fig. 5.1.

5.4 Appendix I: Plots of advective, birth and death components of $\dot{P}(\boldsymbol{p})$

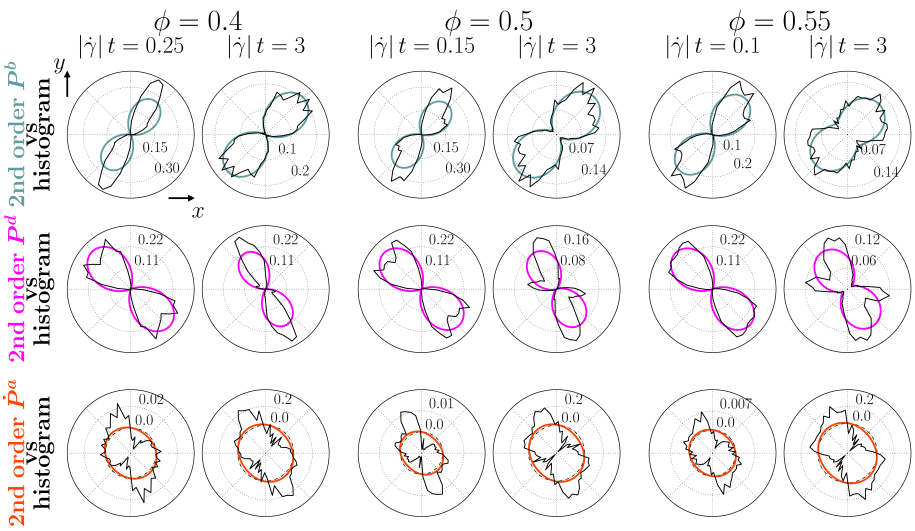

Polar plots of simulation data for $P^b(\boldsymbol{p})$ (**top**), $P^d(\boldsymbol{p})$ (**middle**) and $\dot{P}^a(\boldsymbol{p})$ (**bottom**), as defined in Eq. (5.2.6), in the shear plane (black lines) compared to their second-order spherical harmonic approximations (color lines), for $\phi = 0.4$ (left column), $\phi = 0.5$ (middle column), and $\phi = 0.55$ (right column), and for the two strain values after reversal indicated on top of each ϕ column. Below are the same data compared to their fourth-order spherical harmonic approximations.

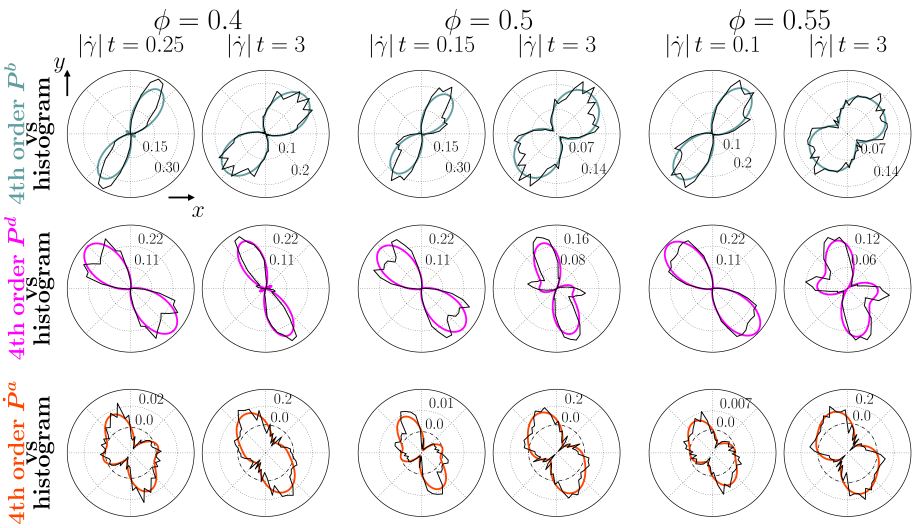

Chapter 6

Relaxation dynamics in an athermal soft suspension

6.1 Introduction

The previous three chapters have shown us how particle simulations can confirm, contradict and contest the predictions and underlying assumptions of models. In each case, the context has been non-Brownian frictional suspensions of hard particles close to but below jamming, either with or without short-ranged repulsive interactions. In this chapter, we will instead consider non-Brownian suspensions of soft particles without short-ranged interactions, particularly at concentrations above jamming. Following the theme of the previous chapters, we will show that behaviour thought to require a finite temperature or an imposed shear can in fact be found in some form in an athermal system, even in the absence of shear.

As the volume fraction ϕ of a hard non-Brownian suspension approaches the jamming fraction, ϕ_{J}, the viscosity diverges and the suspension is unable to flow at any imposed stress. For a soft suspension, this will still be true below a critical shear stress Σ_{y} called the yield stress, but a large enough stress will be able to deform or compress the particles, allowing them to flow past one another. Such materials, for which the shear stress $\Sigma \longrightarrow \Sigma_{\mathrm{y}} > 0$ as the imposed shear rate $\dot{\gamma} \longrightarrow 0^{+}$ (see Fig. 6.1), are known as yield stress materials.

Yield stress materials are an active area of research with a vast literature (see [190]

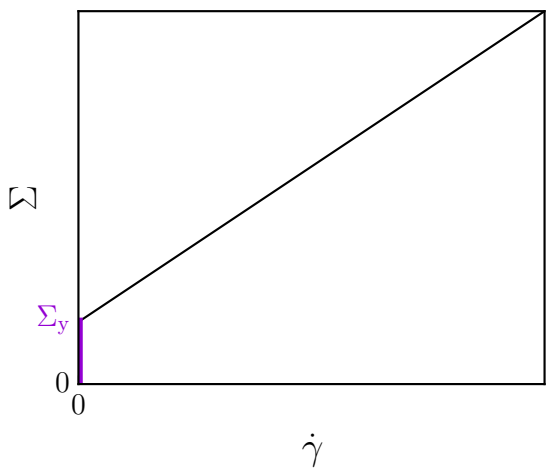

Figure 6.1: Example constitutive curve of a yield stress fluid (specifically, a Bingham fluid [189]) with yield stress Σ_y. Below the yield stress, the constitutive curve is $\dot{\gamma}(\Sigma) \equiv 0$, as shown in purple.

and the references therein). In the context of hard-sphere colloids, the yield stress is thought to emerge above a time scale-dependent volume fraction $\phi_G < \phi_J$. When $\phi > \phi_G$, particles under a small imposed stress are trapped in cages formed by neighbouring particles, and are not, on experimental time scales, able to flow. In the athermal suspensions studied in this thesis, by contrast, jamming is simply a consequence of having more constraints than degrees of freedom for particle motion [48] (e.g. an infinitely large frictionless suspension is jammed if every particle has $2d$ contacts constraining motion along each dimensional axis). A combination of these two mechanisms has then been found to inform the rheology of soft thermal suspensions [191].

Yielding has been associated with shear localisation, in which the flow of a material occurs in small, isolated regions, and thixotropy, in which the viscosity of the material is time- and strain history-dependent [192]. For glassy systems, such behaviour has been explained using a model in which small groups of particles are coarse-grained into volume elements, each with their own energy well [193,194]. Each group can rearrange so as to hop, with a probability that depends on the depth of the well, into a new energy well, randomly chosen from a given distribution. As a volume element builds strain, its probability of hopping into a new well increases. A well hop

corresponds to a local plastic rearrangement of particles within the volume element, and thus to a relaxing of the built up strain, which is reset to zero after the hop. Hops occur even in the absence of strain, and the distribution of well energies can shift over time towards ever deeper well depths. This model therefore incorporates both the shear localisation and thixotropy observed in yield stress fluids. The model, however, depends on a temperature-like parameter whose interpretation is unclear, and does not provide any mechanistic insight into the hopping events themselves.

The picture that has emerged for these local rearrangements views them as plastic events in an elastic medium [195–197]. Such events induce a long-range quadrupolar strain field in the material [195, 198], which can in turn instigate local rearrangements in other regions, leading in athermal systems to an avalanche of local yield events [196, 199, 200]. These local plastic events have also been identified in supercooled liquids [201]. The corresponding scenario in a quiescent soft athermal suspension relaxing towards the local equilibrium of the system has not been studied until now, having presumably been assumed trivial.

In this chapter, we will show evidence that even in this system with neither imposed shear nor Brownian motion to trigger rearrangements, the system exhibits non-trivial relaxation dynamics. We identify unexpected interesting behaviour, such as coarsening and slow dynamics for the relaxation towards equilibrium of the system. We also find behaviour that may hint at relaxation through local plastic rearrangements.

6.2 Methodology

We consider a d-dimensional, athermal, non-inertial system of $N = 10^6$ soft, frictionless particles suspended in a quiescent fluid. We choose a large system size because larger systems delay the onset of noise in the dynamics of the system, as shown in §6.5.3. As in the previous chapters, we consider a bi-disperse system in order to avoid crystallisation, setting half our particles' radii to a, and the other half's to $1.4a$. These reside in a periodic cube of volume fraction-dependent edge length (or the d-dimensional equivalent of this). The forces acting on a given particle i consist

of a hydrodynamic force $\boldsymbol{F}_i^{\mathrm{H}}$ due to the ambient fluid and a contact force $\boldsymbol{F}_i^{\mathrm{C}}$ from overlapping particles. The resultant force-balance condition is therefore

$$0 = \boldsymbol{F}_i^{\mathrm{H}} + \boldsymbol{F}_i^{\mathrm{C}}. \tag{6.2.1}$$

We model contact forces between overlapping soft particles using a harmonic soft repulsive potential,

$$\boldsymbol{F}_i^{\mathrm{C}} = -\sum_{j \neq i} \nabla_{\boldsymbol{r}_{ij}} V\left(\boldsymbol{r}_{ij}\right), \tag{6.2.2}$$

where the pair potential is

$$V\left(\boldsymbol{r}_{ij}\right) = \frac{1}{8}\epsilon u\left(\boldsymbol{r}_{ij}\right)^2 \Theta\left(u\left(\boldsymbol{r}_{ij}\right)\right) \tag{6.2.3}$$

given particle overlap $u\left(\boldsymbol{r}_{ij}\right) := 2 - 2r_{ij}/\left(a_i + a_j\right)$ (i.e. $u = -h$, where h is the gap size defined in §4.2) and a spring constant ϵ with dimensions of energy. Here, Θ is the Heaviside function. In this chapter, we will mainly be interested in systems with volume fractions slightly above that at which contact forces do not vanish in steady state, in regimes at which the dynamics are slow. In this regime, a system at or near equilibrium will have a distribution of particle overlaps peaked at small overlap u, so the pair potential, Eq. 6.2.3, may be considered the leading-order Taylor expansion of a more general contact interaction potential, and therefore generic. We also choose a particularly simple form for our hydrodynamics,

$$\boldsymbol{F}_i^{\mathrm{H}} = -\zeta \dot{\boldsymbol{r}}_i, \tag{6.2.4}$$

describing drag on particles travelling in a quiescent fluid.

We can then non-dimensionalise our system, choosing the small-particle radius a as our length scale, ζ/a as our viscosity scale and ϵ as our energy scale. The force scale is therefore ϵ/a, the stress scale is ϵ/a^3 and the time scale is $a^2\zeta/\epsilon$. Having non-dimensionalised in this way, $a = \zeta = \epsilon = 1$, and our equation of motion is

$$\dot{\boldsymbol{r}}_i = \sum_{j \neq i} \frac{2u_{ij}}{a_i + a_j} \Theta\left(u_{ij}\right) \hat{\boldsymbol{r}}_{ij} \quad \forall\, i. \tag{6.2.5}$$

The hydrodynamic and contact force terms, Eqs. 6.2.2 and 6.2.4, are clearly a gross simplification of a more realistic description of such terms. For instance, our

contact interactions neglect rotational degrees of freedom and allow matter to overlap rather than explicitly modelling particle deformations. Our hydrodynamic interactions, though of a commonly-chosen form [27, 191, 197, 202–205], violate Galilean invariance, neglect lubrication forces and ignore the dependence of Stokes drag on the radius of particles. We justify these simplifications because they allow us to simulate larger three-dimensional systems of particles in fluid, while still reproducing characteristic features of glassy rheology when the system sheared [202]. We have also checked that our dynamics are not qualitatively affected if we use a Galilean-invariant drag in which the drag force on particle i is calculated based on the velocity of particle i relative to those of neighbouring particles j, as seen in dissipative particle dynamics [206].

Our simulations draw the initial position of each particle from a uniform distribution on the d-dimensional cube $[0, L)^d$, where we recall that L is determined by the volume fraction ϕ we wish to impose. This volume fraction is calculated as $\phi = \left[\frac{N}{2}\mathrm{Vol}(1; d) + \frac{N}{2}\mathrm{Vol}(1.4; d)\right] / L^d$, where $\mathrm{Vol}(a; d)$ is the volume of the d-dimensional solid sphere of radius a; we do not take particle overlaps into account. From this initial configuration, we allow the system to evolve towards its local total potential energy minimum (see §6.5 for numerical details), and analyse the dynamics of this relaxation. Non-dimensionalising temperature according temperature scale ϵ/k_B, where k_B is the Boltzmann constant, this initial condition corresponds to preparing a system at temperature $T = \infty$ before instantaneously quenching to $T = 0$ at time $t = 0$.

In §6.6, we show evidence that the dynamics we obtain using this preparation protocol are consistent with those for a more experimentally-feasible protocol. Specifically, we consider a protocol in which the system is prepared at a finite temperature $T = 10^{-2}$ at a sub-jamming volume fraction $\phi = 0.5$ before the quench, at which point the particles are expanded until the target volume fraction is obtained. In practice, given L_0 such that the pre-quench volume fraction is ϕ_0 and L such that the post-quench volume fraction is ϕ, we get from ϕ_0 to ϕ by taking $\boldsymbol{r}_i \mapsto (L/L_0)\,\boldsymbol{r}_i$ for the position vector $\boldsymbol{r}_i$ of each particle i. This models experimental systems of thermo-sensitive soft particles which swell as a function of temperature [207–209].

6.3 Results

6.3.1 Relaxation Dynamics

The first result of this chapter is the discovery of evidence of slow dynamics in the relaxation of the system towards local equilibrium. In Fig. 6.2, we show the post-quench decay of the root mean squared speed (top) and the negative of the rate of change of potential energy (bottom) of a two- (left) and three- (right) dimensional system at a range of volume fractions ϕ straddling the jamming fraction ϕ_{J}, which, given a bi-disperse system of spheres of radius a and $1.4a$ at equal population, has values $\phi_{\mathrm{J}} \approx 0.842$ and $\phi_{\mathrm{J}} \approx 0.64$ in two and three dimensions respectively [47]. We see that for $\phi < \phi_{\mathrm{J}}$, the decay appears to be exponential. For $\phi > \phi_{\mathrm{J}}$, there appears to be a power-law decay after a time $t \approx 30$. We obtain approximate decays of $\sqrt{\langle v^2 \rangle} \sim t^{-0.95}$ in two dimensions and $\sqrt{\langle v^2 \rangle} \sim t^{-0.9}$ in three dimensions, significantly slower than the $\sqrt{\langle v^2 \rangle} \sim t^{-1+\frac{d}{4}}$ decay of a crystal lattice of springs (see §6.7). For the rate of change of potential energy per particle, we find power-law decays $\left\langle \dot{V} \right\rangle \sim -t^{-1.8}$ in both two and three dimensions, consistent with a decay of $\left\langle \dot{V} \right\rangle$ towards a non-zero equilibrium value.

We obtain a more detailed understanding of how this slowing dynamics occurs by plotting, in Fig. 6.3, the evolution of the distribution of the logarithm of the speed, $\log_{10} v$, over time for above-jamming volume fractions $\phi = 0.9$ in two dimensions (left) and $\phi = 0.7$ in three dimensions (right). We see that the evolution approximately corresponds to a shift of the distribution to lower speeds by a constant amount per decade, though the high-speed tail broadens slightly over time.

6.3.2 Coarsening

The slow dynamics hint at the possible existence of a growing length scale in the system [210]. To investigate this, we now explicitly consider the spatiotemporal dynamics of the microstructural evolution of the system. It is useful, in this context, to define two new particle-level quantities. We define the potential energy of particle

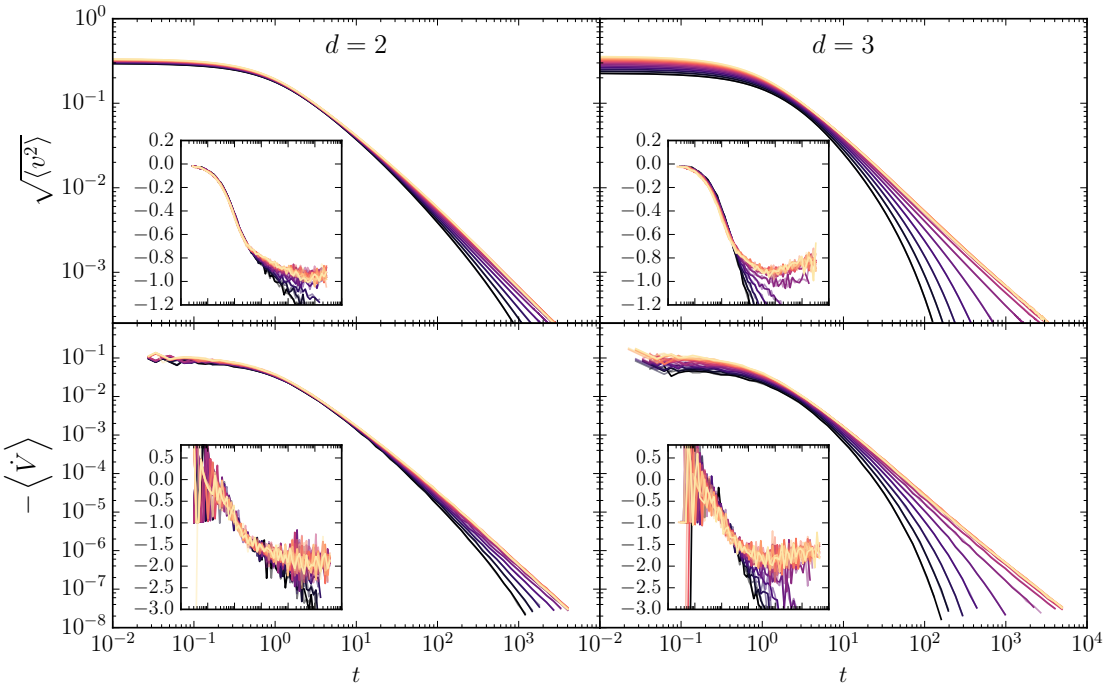

Figure 6.2: Decay of the root mean squared speed (top) and of the negative rate of change of potential energy per particle (bottom) against time t in two (left) and three(right) dimensions. Data colour-coded by value of ϕ; lighter colour implies larger ϕ. In two dimensions, $\phi \in \{0.78, 0.8, \ldots, 1\}$, while in three dimensions, $\phi \in \{0.4, 0.45, \ldots, 1\}$. Insets: slope of the data in the log-log plot into which the inset is embedded against time. The transparent and opaque curves of a given colour correspond to the same parameter set but a different random initial condition.

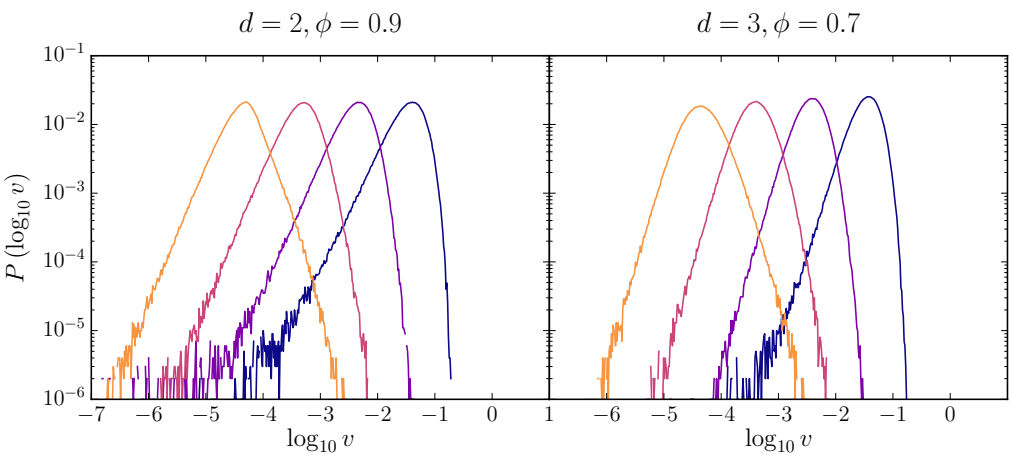

Figure 6.3: Distribution $P(\log_{10} v)$ at logarithmically-spaced times $t = 10^1, \cdots, 10^4$. Lighter colour means larger t.

i to be

$$V_i := \frac{1}{2} \sum_{j \neq i} V\left(\boldsymbol{r}_{ij}\right). \tag{6.3.6}$$

This is defined such that sum of all particle-level potential energies corresponds to the total potential energy of the system. We also define the non-affinity measure

$$D_i^2 := \min_{\boldsymbol{K}} \sum_{j \neq i} \left|\left|\dot{\boldsymbol{r}}_{ij} - \boldsymbol{K} \cdot \boldsymbol{r}_{ij}\right|\right|^2 \Theta\left(r_{\text{cut-off}} - r_{ij}\right), \tag{6.3.7}$$

where the cut-off distance $r_{\text{cut-off}} = 3$ is chosen so as to be slightly above the separation of two large particles in contact. Here, $\boldsymbol{K}$ is a rank-2 tensor representing the velocity gradient tensor of an affine motion, and we are minimising over all such tensors. This is an instantaneous version of Falk and Langer's non-affinity measure [211], D^2_{min}, and is evidence of plastic rearrangements occurring in the system. Where Falk and Langer defined

$$D^2_{\text{min}}\left(t, \Delta t; i\right) = \min_{\boldsymbol{E}} \sum_{j \neq i} \left|\left|\boldsymbol{r}_{ij}\left(t + \Delta t\right) - \boldsymbol{E} \cdot \boldsymbol{r}_{ij}\left(t\right)\right|\right|^2 \Theta\left(r_{\text{cut-off}} - r_{ij}\right) \tag{6.3.8}$$

($\boldsymbol{E}$ is a rank-2 tensor representing the strain tensor of an affine displacement), we instead have

$$D_i^2 = \lim_{\Delta t \to 0} \min_{\boldsymbol{E}} \frac{1}{\Delta t^2} \sum_{j \neq i} \left|\left|\boldsymbol{r}_{ij}\left(t + \Delta t\right) - \boldsymbol{E} \cdot \boldsymbol{r}_{ij}\left(t\right)\right|\right|^2 \Theta\left(r_{\text{cut-off}} - r_{ij}\right). \tag{6.3.9}$$

For analysing our system, we prefer this instantaneous version to the original because the lengthening time scales in our system mean that a fixed Δt would sample a decreasing slice of the microstructural evolution as t increases.

In Fig. 6.4, we plot snapshots of a two-dimensional system of particles at volume fraction $\phi = 0.9$, colouring the particles according to their speed, non-affinity measure and rate of change of potential energy. Cross-sections of a three-dimensional system show similar behaviour, as shown in Fig. 6.5. At all times shown, we see that outlier particles with large v, large D^2 and large $\left|\dot{V}\right|$ are concentrated in hotspots, which grow in size with increasing time t. This apparent coarsening provides strong evidence of spatial correlations growing in time, which may in turn help explain the slow relaxation dynamics of the system.

We also see a good correspondence between the outliers of v, D^2 and $\left|\dot{V}\right|$, so that a particle with e.g. exceptionally high speed is likely to have exceptionally rapidly

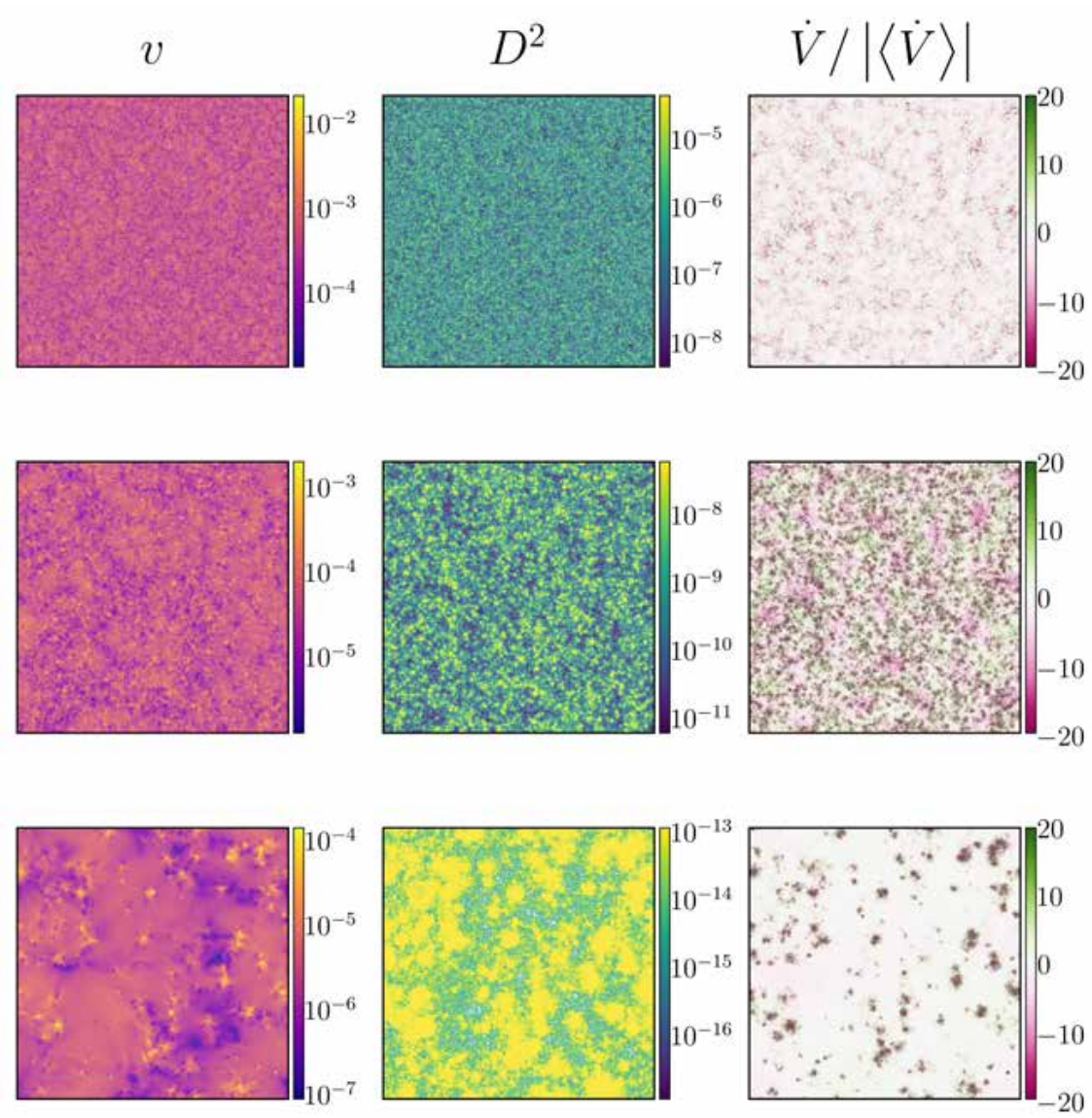

Figure 6.4: Snapshot of particles in a two-dimensional system at $\phi = 0.9$ at times $t = 10^3$ (top), $t = 10^4$ (middle) and $t = 10^5$ (bottom). Particles are coloured according to speed (left), non-affine measure D^2 (centre) and rate of change of particle energy relative to the average rate, $\dot{V}/\left|\langle\dot{V}\rangle\right|$ (right). The colour scales for v and D^2 are centred around the mode of their logarithms.

changing potential energy and live in an exceptionally non-affine neighbourhood. We confirm this correspondence in Fig. 6.6, which shows the density of particles in v-D^2 space, D^2-$\left|\dot{V}\right|$ space and v-$\left|\dot{V}\right|$ space. We see that each contour is stretched in the direction of high-magnitude v, D^2 and $\left|\dot{V}\right|$, indicating a positive correlation between these quantities in this region.

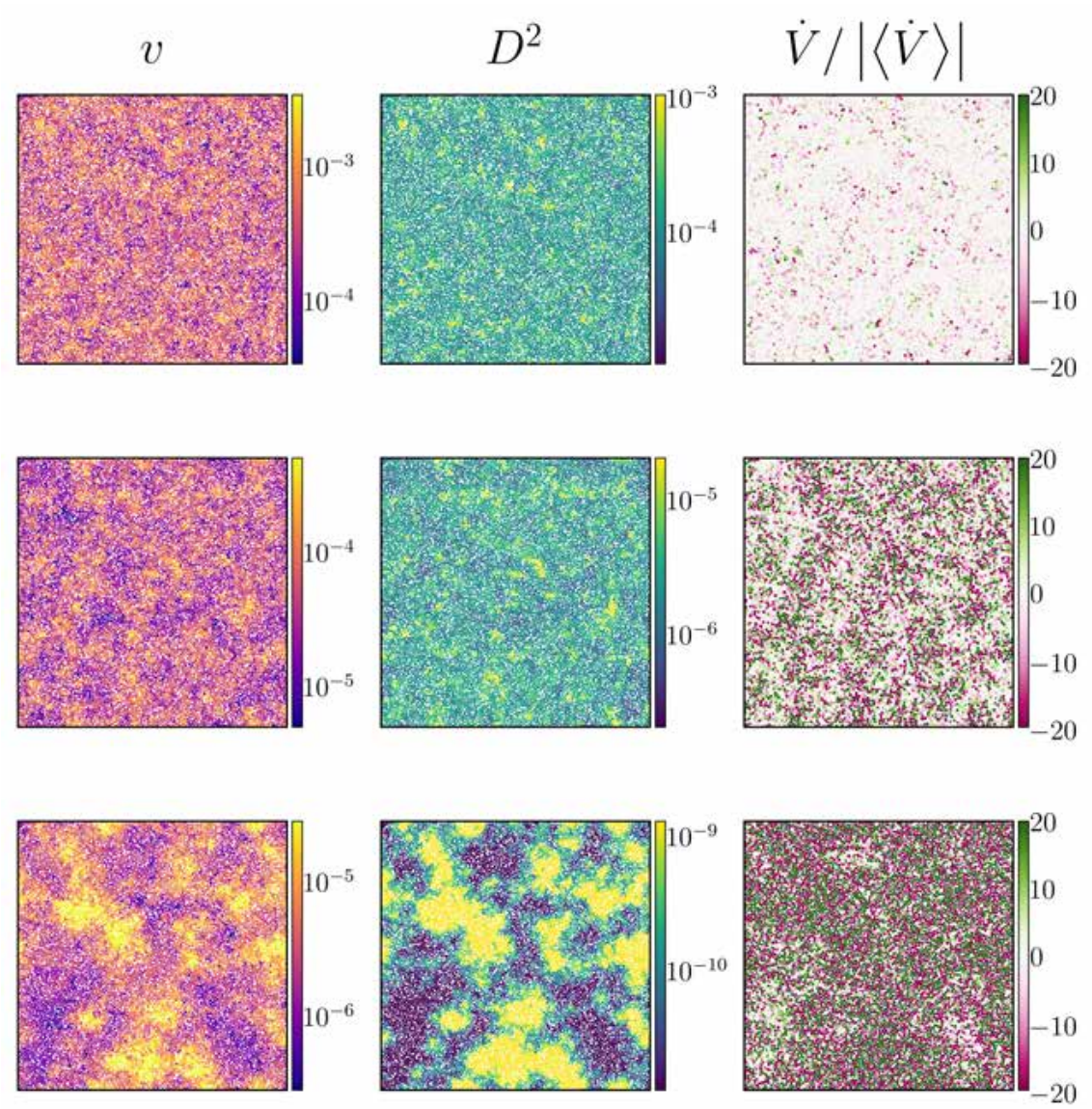

Figure 6.5: Snapshot of a cross-section of particles in the plane $\{z = L/2\}$, where L is the system width, for a three-dimensional system at $\phi = 0.7$ at times $t = 10^3$ (top), $t = 10^4$ (middle) and $t = 10^5$ (bottom). Particles are coloured according to speed (left), non-affine measure D^2 (centre) and rate of change of particle energy relative to the average rate, $\dot{V}/\left|\langle\dot{V}\rangle\right|$ (right). The colour scales for v and D^2 are centred around the mode of their logarithms.

6.3.3 Local plastic events

We have seen that the system relaxation is concentrated in hotspots in which the local velocity field is non-affine and particle speeds are high. This is potentially

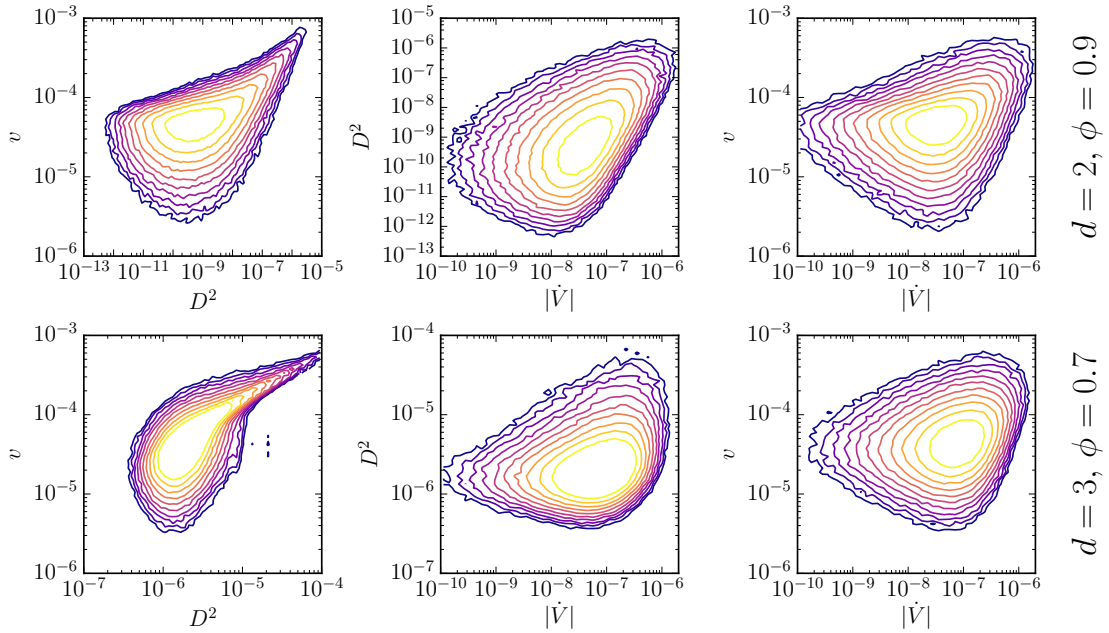

Figure 6.6: Correlations between the speed v, non-affine measure D^2 and magnitude of rate of change of particle potential energy $\left|\dot{V}\right|$ at time $t = 10^4$ for $\phi = 0.9$ in two dimensions (top) and $\phi = 0.7$ in three dimensions (bottom). Contours show level sets for the number of particles, $N = 10^{1.5}, 10^{1.7}, \cdots, 10^{3.5}$, within bins of $\log v$-width w_v, $\log D^2$-width w_D and $\log\left|\dot{V}\right|$-width $w_{\dot{V}}$ in $(\log D^2, \log v)$-space (left), in $\left(\log\left|\dot{V}\right|, \log D^2\right)$-space (centre) and $\left(\log\left|\dot{V}\right|, \log v\right)$-space (right). In two dimensions, $(w_v, w_D, w_{\dot{V}}) = (0.05, 0.05, 0.1)$, while in three dimensions, $(w_v, w_D, w_{\dot{V}}) = (0.05, 0.1, 0.1)$.

consistent with a picture in which stress in a soft particle system relaxes through local plastic events (or "shear transformation zones" [211]). In our case the zones get larger with time, suggesting that particles behave increasingly collectively to relax their potential energy as the local minimum of the system is approached. Such events have been extensively studied in the context of sheared amorphous materials [196, 212–217]. Recently, studies have also observed them in (unsheared) finite-temperature colloids [201, 218, 219] and soft amorphous solids subjected to sound [220].

In these systems, in shear, it has been found that plastic events induce a quadrupolar displacement field in the surrounding medium [196]. This is consistent with

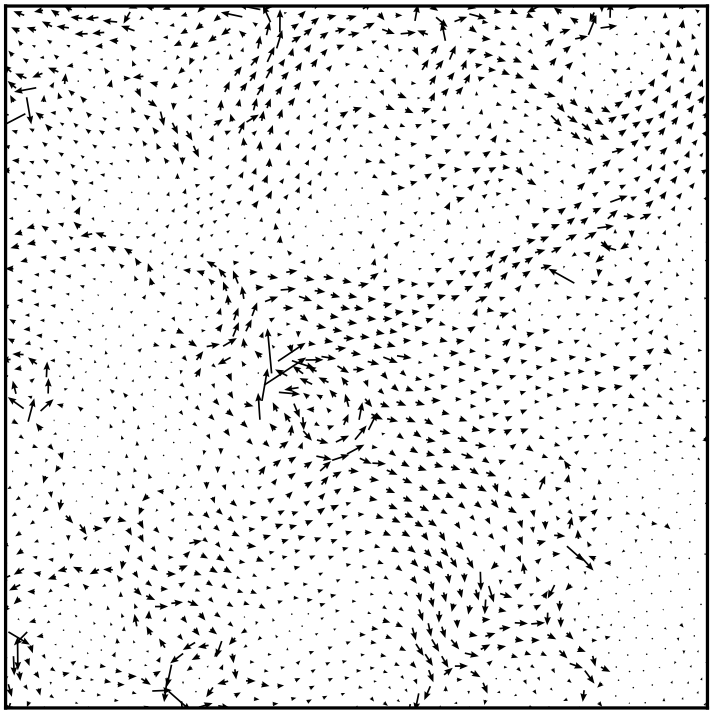

Figure 6.7: Displacement field of particles within a 100×100 particle radius box from a two-dimensional system of $N = 10^6$ particles at volume fraction $\phi = 0.9$. The displacement occurs between times $t = 1800$ and $t = 2200$. Arrows have been enlarged by a factor of ten to make them easier to see.

the expectation for a plastic event occurring within an infinite or periodic elastic medium [195, 198]. In Fig. 6.7, we show a zoom-in on a square region of area 10^4 of the displacement of particles between times $t = 1800$ and $t = 2200$ in a two-dimensional system at volume fraction $\phi = 0.9$. We see clear evidence of the characteristic swirling vortices associated with local plastic events. Indeed, Fig. 6.7 bears a striking resemblance to the displacement fields induced by plastic events in the literature, particularly the displacement fields due to multiple, closely-packed plastic events [196, 201, 212, 213].

We can relate the coarsening seen in the hot spots of Fig. 6.4 to the spatial velocity correlations evident in the swirls of Fig. 6.7 by plotting the two-dimension velocity correlation function, $\langle \mathbf{v}(\mathbf{r}) \cdot \mathbf{v}(\mathbf{r} + \Delta\mathbf{r}) \rangle$ normalised mean squared velocity in Fig. 6.8. As seen in the inset to this figure, which shows the growth of $l_* := \sup \{\Delta r : \langle \mathbf{v}(\mathbf{r}) \cdot \mathbf{v}(\mathbf{r} + \Delta\mathbf{r}) \rangle > 0.1\}$ against time, the correlation length grows

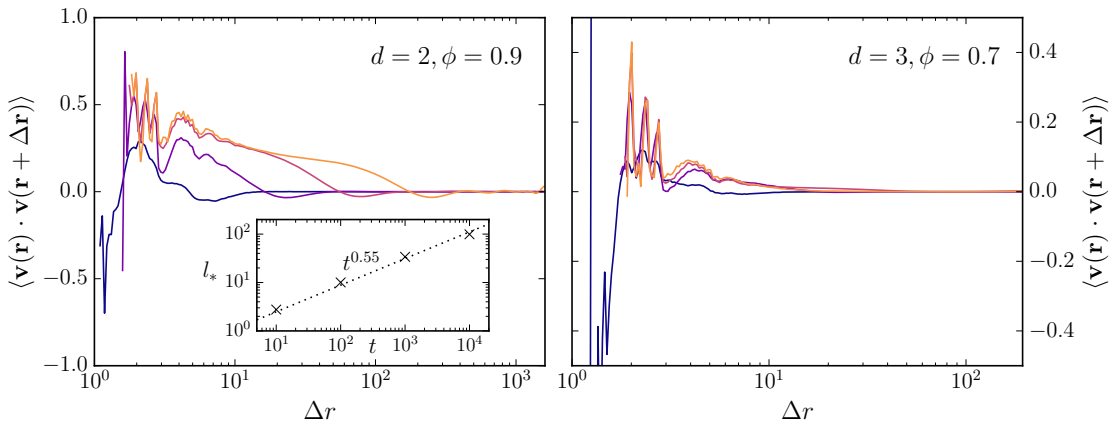

Figure 6.8: Normalised spatial correlation function of the viscosity for $\phi = 0.9$ in two dimensions (left) and $\phi = 0.7$ in three dimensions at times $t = 10^1$, 10^2, 10^3 and 10^4. The average is taken over $N/5$ choices of particle at the origin and N second particles at $\Delta\boldsymbol{r}$. Lighter colour corresponds to later time. Inset: Power-law (dotted line) fitted to data (crosses) for the correlation length $l_* := \sup\{\Delta r : \langle \mathbf{v}(\mathbf{r}) \cdot \mathbf{v}(\mathbf{r} + \Delta\mathbf{r}) \rangle > 0.1\}$ against time.

with a power law $l^* \sim t^{0.55}$. This behaviour is not seen in the velocity correlation function in three dimensions. This is likely a consequence of the additional directional degree of freedom in three dimensions leading to the decorrelation of particle velocities.

We also show one final piece of evidence that the relaxation mechanism we observe for our system is consistent with the plastic events picture proposed for thermal or sheared systems. This is the intermittency of the dynamics: a given particle will only transiently be part of a hot spot. We demonstrate this intermittency by showing the time evolution of four particles in Fig. 6.9, where we clearly see that the speed, non-affine measure and rate of change of potential energy show similar dynamics. In particular, we see spikes in these quantities for a given particle occurring around the same time.

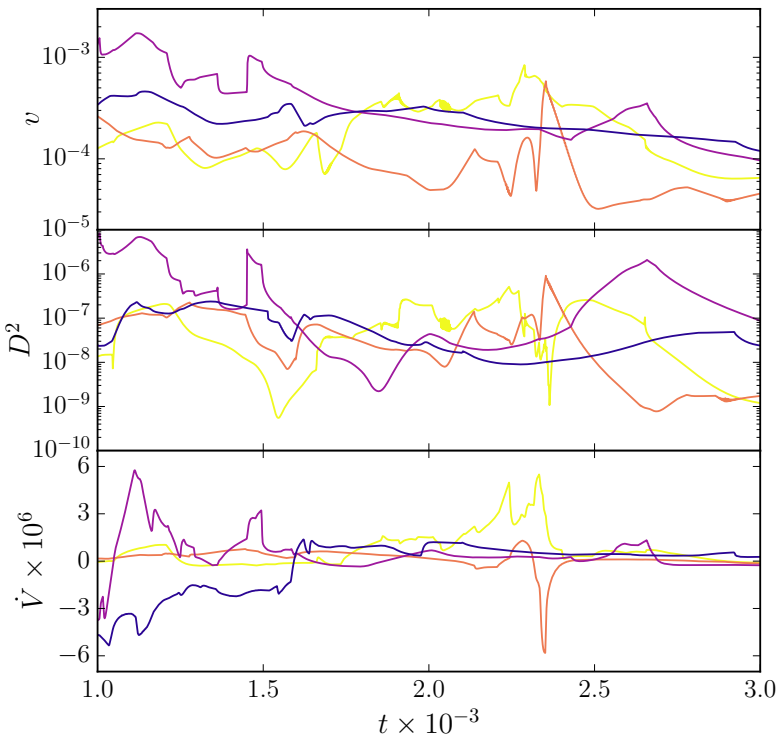

Figure 6.9: Time signal of the speed (top), non-affine measure (middle) and rate of change of potential energy (bottom) for four particles, labelled by colour. These were chosen out of one hundred randomly selected particles such that their $\dot{V}$ dynamics is of a similar scale.

6.4 Conclusion

In this chapter, we studied the relaxation of a quiescent athermal soft suspension towards the local equilibrium of the system. We have identified a slow power-law relaxation of the system, and shown that this relaxation takes place within local hotspots which grow in size as the system ages. We have also looked at the displacement field across the lifetime of a hotspot, which bears a resemblence to that seen for multiple closely-packed plastic events in soft suspensions under quasi-static shear or at a finite temperature. We believe this to be the first report of local plastic deformations, or interesting dynamics in general, in an unsheared athermal soft suspension relaxing towards its local equilibrium (of the global system).

Having identified several interesting phenomena in the relaxation of our system, the natural question is if we can identify a theoretical explanation. For instance,

could one relate the coarsening of hotspots to the need to cross energy barriers before a plastic rearrangement, given an ever-decreasing pool of potential energy per particle available for doing so? It would also be interesting to see if the slow relaxation of the microstructure has observable consequences for the rheology of the suspension given a waiting time t_w before the imposition of flow. Finally, we hope that the behaviour we have identified here will lead to a better understanding of soft glassy materials in general.

6.5 Appendix I: Numerical details

6.5.1 Evolving the system

Given a configuration for our N particles, we calculate the velocities of each particle according to Eq. 6.2.5. We use cell structures [221] to conduct this calculation in an amount of time that varies linearly with N. This involves dividing the system into a grid of boxes of width $\lfloor L/2.8 \rfloor$ and calculating the total force on particle i by iterating over particles in the same or neighbouring boxes. (The simulation was coded (by the author of this thesis) in C++, so this iteration was achieved using vectors of box objects rather than linked lists [221, 222].)

When calculating interparticle interactions, periodic boundary conditions require one to solve the "minimum image problem", determining the distance between points given the periodicity of the system. For instance, a particle i at position $\boldsymbol{r}_i = (x_0, y_0, 0)$ will overlap a particle j at position $\boldsymbol{r}_j = (x_0, y_0, L - \epsilon)$ where $0 < \epsilon < 1$, but naïvely calculating their separation as $|\boldsymbol{r}_j - \boldsymbol{r}_i| = L - \epsilon$ would lead to the erroneous conclusion that they are far from contact. For the simulations used in this chapter, we adopt a refinement due to Welling and Germano [222] of an approach due to Rapaport [223] in which we create copies of boxes at the extremities of the grid, whose coordinates (and those of the particles they contain) are shifted by L along one or more axes. In this way, particles in a cell at an edge of the grid can interact with particles in cells at opposite edges via their copies.

After determining the velocities on all particles, we evolve their positions using

a simple forward Euler method [118],

$$\boldsymbol{r}_i\left(t+\Delta t\right)=\boldsymbol{r}_i\left(t\right)+\Delta t\,\dot{\boldsymbol{r}}_i\left(t\right), \tag{6.5.10}$$

where the time-step $\Delta t = \alpha / \max_i \dot{r}_i$ grows as the system dynamics slow down. We find our results to be converged for $\alpha \gtrsim 10^{-2}$, and so use $\alpha = 10^{-2}$ when evolving our system.

6.5.2 Preparing the system

We prepare our system at $T = \infty$ by selecting the position of each component of each particle from a uniform distribution on $[0, 1)$ and multiplying each component by L. For the finite-temperature initial condition discussed in §6.6, we take this $T = \infty$ configuration of particles at $\phi_0 = 0.5$ and evolve the system using a Langevin thermostat [221] at temperature $T = 10^{-2}$. This involves adding a term $\sqrt{2T\Delta t}\,\chi$, with χ a Gaussian-distributed random number with zero mean and unit variance (obtained, in our case, using the Box-Muller algorithm [118]), to Eq. 6.5.10 when updating the particle positions. We evolve the system in this way for 1000 time units, which we find to be long enough for the mean particle velocity, coordination number and potential energy to reach their steady states. Having equilibrated our system, we quench the system to $T = 0$ and swell our particles to obtain the target post-quench volume fraction ϕ.

6.5.3 Appendix II: Effect of system size

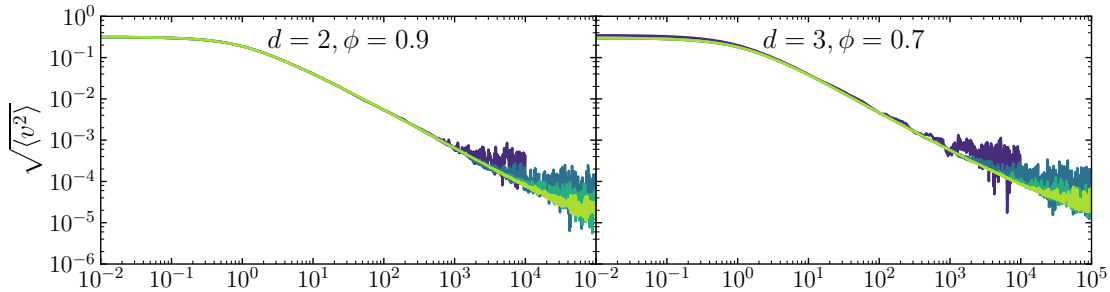

Figure 6.10: Root mean squared speed against time t for a system quenched at time $t = 0$ to temperature $T = 0$ from $T = \infty$ for particle populations $N = 10^3$, 10^4, 10^5 and 10^6. A lighter curve corresponds to a larger population.

Increasing the number of particles in our system has little effect on the dynamics except to push the time at which noise dominates the dynamics to later times, as seen in Fig. 6.10. From Figs. 6.4 and 6.5, it appears that the point at which noise begins to dominate the dynamics ($t \approx 2 \times 10^4$ for $N = 10^6$ particles in Fig. 6.10) coincides with the hotspots attaining a size of the order of the system size.

6.6 Appendix III: Robustness checks

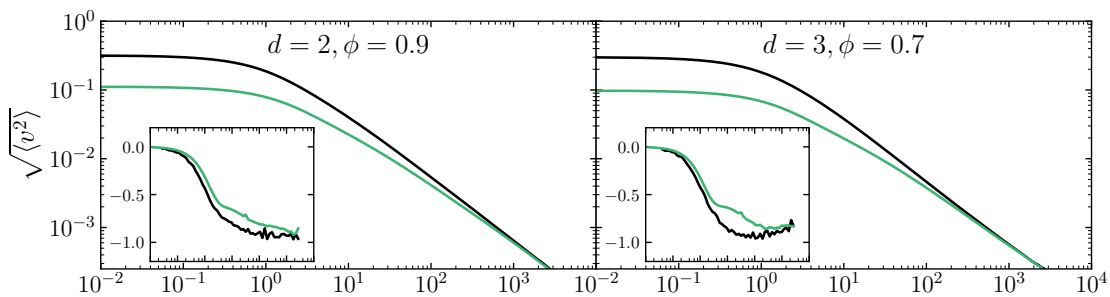

Figure 6.11: Root mean squared speed against time t for a system quenched at time $t = 0$ to temperature $T = 0$ from $T = \infty$ (black) compared to that for a system equilibrated at volume fraction $\phi_0 = 0.5$ and temperature $T = 10^{-2}$ before the $t = 0$ quench (green). We show both two-dimensional data for post-quench $\phi = 0.9$ (left) and three-dimensional data for post-quench $\phi = 0.7$.

In Fig. 6.11, we show that after a post-quench transient of around 10^2 time units, systems prepared at $T = \infty$ show (within noise) the same power-law decay as systems prepared at $T = 10^{-2}$ and $\phi = 0.5$.

6.7 Appendix IV: Velocity decay on an overdamped lattice

We consider a d-dimensional system of N^d identical particles on a periodic lattice. We take the system to be finite, with each particle labelled according to its position vector $\boldsymbol{n} = (n_1, n_2, \ldots, n_d) \in \{0, 1, \ldots, N-1\}^d$ in the primitive vector basis, i.e., each particle $\boldsymbol{n}$ has equilibrium position $\boldsymbol{x_n} = \boldsymbol{A} \cdot \boldsymbol{n}$ where $\boldsymbol{A}$ is the matrix whose columns are the primitive vectors $\boldsymbol{a}_1, \ldots, \boldsymbol{a}_d$ of the lattice. Writing $\boldsymbol{F_{n \leftarrow m}}$ for the force on particle $\boldsymbol{n}$ due to particle $\boldsymbol{m}$ and $\boldsymbol{u_n}$ for the displacement of particle $\boldsymbol{n}$ from its equilibrium position, we assume spring-like interactions

$$\boldsymbol{F_{n \leftarrow m}} = k_\mathrm{s} \left(\boldsymbol{u_m} - \boldsymbol{u_n}\right) \Theta \left(1 - |\boldsymbol{m} - \boldsymbol{n}|\right) \tag{6.7.11}$$

between particles, with k_s a spring constant. We also assume a hydrodynamic drag force

$$\boldsymbol{F}_{\boldsymbol{n}}^{\mathrm{H}} = -\zeta \dot{\boldsymbol{u}}_{\boldsymbol{n}}. \tag{6.7.12}$$

The equation of motion for our system in the overdamped limit is then

$$\begin{aligned} \boldsymbol{0} &= \sum_{\boldsymbol{m} \neq \boldsymbol{n}} \boldsymbol{F_{n \leftarrow m}} + \boldsymbol{F}_{\boldsymbol{n}}^{\mathrm{H}} \\ &= k_\mathrm{s} \left(\sum_{i=1}^{d} \left[\boldsymbol{u}_{\boldsymbol{n}+\boldsymbol{e}_i} + \boldsymbol{u}_{\boldsymbol{n}-\boldsymbol{e}_i} \right] - 2d \boldsymbol{u_n} \right) - \zeta \dot{\boldsymbol{u}}_{\boldsymbol{n}} \end{aligned} \tag{6.7.13}$$

for each $\boldsymbol{n}$, where $\boldsymbol{e}_i$ has components $e_i^j = \delta_{ij}$. Choosing ζ / k_s as our time scale, we obtain, upon non-dimensionalisation,

$$\dot{\boldsymbol{u}}_{\boldsymbol{n}} = \left(\sum_{i=1}^{d} \left[\boldsymbol{u}_{\boldsymbol{n}+\boldsymbol{e}_i} + \boldsymbol{u}_{\boldsymbol{n}-\boldsymbol{e}_i} \right] - 2d \boldsymbol{u_n} \right). \tag{6.7.14}$$

We see that the components $u_{\boldsymbol{n}}^i$ are uncoupled from one another. For notational simplicity, we will write $u_{\boldsymbol{n}}^i$ as $u_{\boldsymbol{n}}$ for a generic, unspecified component i, unless explicitly stated otherwise.

To solve eq. 6.7.14, we use the multidimensional discrete Fourier transform

$$u_{\boldsymbol{n}} = \frac{1}{\sqrt{N^d}} \sum_{\boldsymbol{k}} \hat{u}_{\boldsymbol{k}} e^{2\pi \mathrm{i} \boldsymbol{k}\cdot\boldsymbol{n}/N} \tag{6.7.15}$$

$$\hat{u}_{\boldsymbol{k}} = \frac{1}{\sqrt{N^d}} \sum_{\boldsymbol{n}} u_{\boldsymbol{n}} e^{-2\pi \mathrm{i} \boldsymbol{k}\cdot\boldsymbol{n}/N}, \tag{6.7.16}$$

where $\boldsymbol{k} := (k_1, k_2, \cdots, k_d)$, $\sum_{\boldsymbol{k}} := \sum_{k_1=0}^{N-1} \sum_{k_2=0}^{N-1} \cdots \sum_{k_d=0}^{N-1}$ and $\sum_{\boldsymbol{n}} := \sum_{n_1=0}^{N-1} \sum_{n_2=0}^{N-1} \cdots \sum_{n_d=0}^{N-1}$. Applying this to eq. 6.7.14 yields

$$\frac{1}{\sqrt{N^d}} \sum_{\boldsymbol{k}} \dot{\hat{u}}_{\boldsymbol{k}} e^{2\pi \mathrm{i} \boldsymbol{k}\cdot\boldsymbol{n}/N} = -\frac{2}{\sqrt{N^d}} \sum_{\boldsymbol{k}} \hat{u}_{\boldsymbol{k}} e^{2\pi \mathrm{i} \boldsymbol{k}\cdot\boldsymbol{n}/N} \left[d - \sum_{i=1}^{d} \cos\left(2\pi k_i/N\right) \right],$$

so that

$$\hat{u}_{\boldsymbol{k}}(t) = \hat{u}_{\boldsymbol{k}}(0) \exp\left(-2 \left[d - \sum_{i=1}^{d} \cos\left(2\pi k_i/N\right) \right] t \right). \tag{6.7.17}$$

We seek the mean squared speed, $\langle \dot{u}_{\boldsymbol{n}}^2 \rangle$. Applying the Plancherel theorem,

$$\sum_{\boldsymbol{n}} |x_{\boldsymbol{n}}|^2 = \sum_{\boldsymbol{k}} |\hat{x}_{\boldsymbol{k}}|^2, \tag{6.7.18}$$

we obtain

$$\begin{aligned} \langle \dot{u}_{\boldsymbol{n}}^2 \rangle &= \frac{1}{N^d} \sum_{\boldsymbol{n}} \dot{u}_{\boldsymbol{n}}^2 \\ &= \frac{1}{N^d} \sum_{\boldsymbol{k}} \dot{\hat{u}}_{\boldsymbol{k}}^2 \\ &= \frac{4}{N^d} \sum_{\boldsymbol{k}} |\hat{u}_{\boldsymbol{k}}(0)|^2 \left[d - \sum_{i=1}^{d} \cos\left(2\pi k_i/N\right) \right]^2 e^{-4\left[d - \sum_{i=1}^{d} \cos(2\pi k_i/N)\right] t}. \end{aligned} \tag{6.7.19}$$

We want to average this over initial conditions $\{u_{\boldsymbol{n}}(0)\}_{\boldsymbol{n}}$. Writing $\langle \cdot \rangle_0$ for this average over initial conditions, we can assume that the $u_{\boldsymbol{n}}(0)$ (and thus $u_{\boldsymbol{n}}(0)^2$) are independent and identically distributed, so that

$$\begin{aligned} \langle \langle u_{\boldsymbol{n}}^2(0) \rangle \rangle_0 &= \left\langle \frac{1}{N^d} \sum_{n=0}^{N-1} u_{\boldsymbol{n}}^2(0) \right\rangle_0 \\ &= \frac{1}{N^d} \sum_{\boldsymbol{n}} \langle u_{\boldsymbol{n}}^2(0) \rangle_0 \\ &= \frac{1}{N^d} \sum_{\boldsymbol{n}} \langle u_{\boldsymbol{n}}^2(0) \rangle \\ &= \langle u_{\boldsymbol{n}}^2(0) \rangle, \end{aligned} \tag{6.7.20}$$

where eq. 6.7.20 uses the law of large numbers, and hence an assumption of large N. We see that

$$\begin{aligned}\left\langle |u_{\boldsymbol{k}}|^2 \right\rangle_0 &= \frac{1}{N^d} \sum_{\boldsymbol{m}=0} \sum_{\boldsymbol{n}=0} \langle u_{\boldsymbol{m}} u_{\boldsymbol{n}} \rangle_0 \, e^{-2\pi i \boldsymbol{k}(\boldsymbol{m}-\boldsymbol{n})/N} \\ &= \frac{1}{N^d} \sum_{\boldsymbol{n}} \left\langle u_{\boldsymbol{n}}^2 \right\rangle_0 \\ &= \left\langle u_{\boldsymbol{n}}^2 \right\rangle ,\end{aligned} \tag{6.7.21}$$

where the second equality (eq. 6.7.21) is due to the independence of $u_{\boldsymbol{n}}$ and $u_{\boldsymbol{m}}$, and the assumption that they have zero mean. We may thus write

$$\left\langle \dot{u}_{\boldsymbol{n}}^2 \right\rangle = \frac{4\sigma^2}{N^d} \sum_{\boldsymbol{k}} \left[d - \sum_{i=1}^{d} \cos\left(2\pi k_i/N\right) \right]^2 e^{-4\left[d - \sum_{i=1}^{d} \cos(2\pi k_i/N)\right] t}, \tag{6.7.22}$$

where $\sigma^2 := \langle u_n^2 \rangle$. We convert this to an integral

$$\begin{aligned}\left\langle \dot{u}_{\boldsymbol{n}}^2 \right\rangle = 4\sigma^2 \lim_{L_1 \to \infty} \frac{1}{L^d} \int_0^L \int_0^L \cdots \int_0^L \left[d - \sum_{i=1}^{d} \cos\left(2\pi k_i a/L\right) \right]^2 \times \\ e^{-4\left[d - \sum_{i=1}^{d} \cos(2\pi k_i a/L)\right] t} \mathrm{d}k_1 \mathrm{d}k_2 \ldots \mathrm{d}k_d.\end{aligned} \tag{6.7.23}$$

in the limit $N \longrightarrow \infty$, using $N = a/L$ where $a := |\boldsymbol{a}_1|$ and $L := N\,|\boldsymbol{a}_1|$.

Approximating $d - \sum_{i=1}^{d} \cos\left(2\pi k_i/N\right) \approx 2\pi^2\, \boldsymbol{k}\cdot\boldsymbol{k}\, a^2/L^2$ and changing coordinates to $\boldsymbol{\kappa} = \boldsymbol{k}\sqrt{t}$ gives us

$$\begin{aligned}\left\langle \dot{u}_{\boldsymbol{n}}^2 \right\rangle &= 8\pi^4 \sigma^2 a^4 \lim_{L \to \infty} \frac{1}{L^{d+4}} \int_0^L (\boldsymbol{k}\cdot\boldsymbol{k})^2 \, e^{-8\pi^2 \boldsymbol{k}\cdot\boldsymbol{k}\left(a^2/L^2\right) t} \mathrm{d}k_1 \mathrm{d}k_2 \ldots \mathrm{d}k_d \\ &= 8\pi^4 \sigma^2 a^4 t^{-\left(2+\frac{d}{2}\right)} \lim_{L \to \infty} \frac{1}{L^{d+4}} \int_0^L \int_0^L \cdots \int_0^L (\boldsymbol{\kappa}\cdot\boldsymbol{\kappa})^2 \, e^{-8\pi^2 \boldsymbol{\kappa}\cdot\boldsymbol{\kappa}\, a^2/L^2} \mathrm{d}\kappa_1 \mathrm{d}\kappa_2 \ldots \mathrm{d}\kappa_d,\end{aligned} \tag{6.7.24}$$

giving us a scaling $\langle \dot{u}_{\boldsymbol{n}}^2 \rangle \sim t^{-\left(2+\frac{d}{2}\right)}$ in d-dimensions.

The full mean squared displacement velocity, $\langle \dot{\boldsymbol{u}}_{\boldsymbol{n}} \cdot \dot{\boldsymbol{u}}_{\boldsymbol{n}} \rangle$, will have an altered prefactor, but will share the same power-law decay exponent. We therefore write, for the decay of the root mean squared velocity in a crystal,

$$\sqrt{\langle v^2 \rangle} \sim t^{-1+\frac{d}{4}}. \tag{6.7.25}$$

Chapter 7

Conclusions

In this thesis, we have studied amorphous athermal suspensions with few ingredients in three different contexts, in each case with the support of particle simulations. In general, exploring simple systems helps one to identify generic physics underlying generic phenomena. For instance, the hydrocluster theory of shear thickening relies on Brownian motion, yet non-colloidal suspensions, such as cornstarch in water, also exhibit shear thickening. By considering the simpler case of a non-Brownian system, one may find a mechanism of shear thickening that applies to both the simple, non-Brownian case, and the colloidal case, such as the transition from frictionless to frictional rheology outlined in Ch. 3. In the course of this thesis, we have furthermore shown how a sparsity of ingredients can be leveraged to develop rheological models (Ch. 4 and, to some extent, Ch. 3). We also provide the example of a soft suspension where removing most ingredients, including flow, preserves a surprising amount of non-trivial dynamics (Ch. 6), further underlining the importance of considering minimal systems when studying generic behaviour. The extreme usefulness of particle simulations, for their part, has been affirmed by the evidence of the previous chapters. We have employed them to test the assumptions (Chs. 3 and 5) and predictions (Chs. 3 and 4) of models, as well as to study the microstructural dynamics of suspensions in great detail (Chs. 5 and 6).

7.1 Vorticity banding

In Ch. 3, we extended the scalar Wyart-Cates model [56] for the steady-state behaviour of a shear thickening suspension to a concentration-coupled one-dimensional dynamical model for the vorticity-axis rheology. Using this model, we predicted the linear instability of homogeneous flow for large systems at negatively sloped points on the constitutive curve. We characterised two types of long-time solution to our model, travelling bands (TBs) and locally oscillating bands (LOBs). Dr. Mari subsequently identified qualitatively similar behaviour in particle simulations of a shear-thickening suspension, though LOB behaviour was seen only transiently in the simulations. This chapter showed that the generic thickening mechanism of the Wyart-Cates model coupled with simple frictional-state and concentration dynamics is sufficient to predict and explain some aspects of the bulk behaviour of suspensions, lending further support to the shear thickening mechanism proposed by Wyart and Cates [56], if not the precise form of the equations (see Fig. 3.9, and also [224]).

Perhaps the most important direction for future work related to the results of Ch. 3 is to study how realistic boundary conditions affect the instabilities we have found, though it is not clear what such conditions would be. The difficulty of finding a three-dimensional constitutive model of suspension rheology (Ch. 4) suggests that particle simulations may be the best way of undertaking such research.

Another direction is suggested by recent work by Guy *et al.* [55], which generalises the Wyart-Cates mechanism, expressing the jamming fraction ϕ_{J} in terms of generically-defined constraints which are imposed or released as a function of stress. This generalisation, which has received recent experimental support [26], might yield new instabilities upon the development of models in the vein of those used in this chapter.

7.2 Fabric tensor dynamics: modelling

In Ch. 4, we modelled the fabric tensor evolution of a dense, non-Brownian suspension of hard particles with frictional contact and hydrodynamical interactions, but no short-ranged repulsion. We considered a flow protocol of simple shear, with

a reversal of shear at time $t = 0$. After enforcing dimensional and symmetry constraints, we used a result due to Hand [167] to systematically develop models for the evolution of the fabric tensor $\boldsymbol{Q}$ as a function of itself and the velocity gradient of increasingly high polynomial order in the components of $\boldsymbol{Q}$. We then fit these models to particle simulation data from Dr. Mari. We found that no linear fabric tensor model of this kind can fit the simulation data after reversal, a significant result in light of recently proposed linear models of this type [161, 162]. Furthermore, we found that though higher-order polynomial models can fit the simulation data, such models are unlikely to contain any physical insight.

The most important conclusion of this chapter is that thoroughly testing microstructural models against data is important when attempting to model suspensions. One immediate direction for further work would be to see if experiments can confirm the conclusions of our study with respect to the fabric tensor.

7.3 Fabric tensor dynamics: microstructure

This conclusion was reinforced in Ch. 5, where we found that the distribution $P(\boldsymbol{p})$ of near-contacts is strongly four-lobed in the shear plane shortly after reversal, and is thus poorly described by an implicitly two-lobed object such as $\boldsymbol{Q}$. Instead, we found that introducing a rank-4 tensor $\boldsymbol{C}$ corresponding to the coefficients of the fourth-order term in the spherical harmonic expansion of $P(\boldsymbol{p})$ provides a significantly better description.

The results of this chapter suggest that future efforts at modelling the microstructure of suspensions might need to take both two- and four-lobed details of the microstructure into account. Further insight might also be gained by considering other flow geometries than shear flow, such as planar extensional flow. Taking a step back, the key motivation for the research in this chapter was the need to test the assumptions underlying the fabric tensor description of the microstructure. Having tested the adequacy of the rank-2 fabric tensor as a proxy for the near-contact orientation distribution $P(\boldsymbol{p})$, it might make sense to now ask to what extent $P(\boldsymbol{p})$ is sufficient as a description of the microstructure.

7.4 Relaxation dynamics

Finally, in Ch. 6, we explored the dynamics of a soft suspension of spheres relaxing towards the local energy minimum of the system. We found that the dynamics is non-trivial, involving slow power-law decay and coarsening with, in two dimensions, velocity correlations which grow as a power-law. Displacement fields reminiscent of the quadrupolar displacement fields for a plastic event in an elastic medium observed in, e.g., sheared [196, 212–217] soft suspensions are seen.

One direction for future work would be to further probe the hotspots observed in our system, and determine whether they are a manifestation of the same local plastic events seen in thermal or sheared systems. In either case, it would also be useful to gain a physical understanding of the phenomena we observe, which may lead to insights on the physics of glassy materials in general.

7.5 Closing remarks

Going forward, the evidence of this thesis suggests that when trying to understand a phenomenon in suspension dynamics, one should identify the simplest system that displays the behaviour in question, and then thoroughly test any proposed model or explanation against detailed particle simulation or experimental data. Furthermore, surprising insights may be gained by using particle simulations to test what was previously assumed, and by seeing if a phenomenon observed in one system can be found in a simpler one.

Suspensions are conceptually simple systems with surprisingly rich behaviour, with many open and interesting questions still to be answered. I hope that this thesis has provided a flavour of this.

Bibliography

[1] S. Strauch and S. Herminghaus. Wet granular matter: a truly complex fluid. *Soft Mattter* **8**, 8271 (2012).

[2] D. A. Weitz and M. Oliveria. Fractal structures formed by kinetic aggregation of aqueous gold colloids. *Physical Review Letters* **52**, 1433 (1984).

[3] G. R. Cokelet, E. W. Merrill, E. R. Gilliland, H. Shin, A. Britten, and R. E. Wells. The rheology of human blood—measurement near and at zero shear rate. *Transactions of the Society of Rheology* **7**, 303 (1963).

[4] R. Höhler and S. Cohen-Addad. Rheology of liquid foam. *Journal of Physics: Condensed Matter* **17**, R1041 (2005).

[5] N. J. Wagner and J. F. Brady. Shear thickening in colloidal dispersions. *Physics Today* **62**, 27 (2009).

[6] H. A. Barnes. Shear-thickening ("dilatancy") in suspensions of nonaggregating solid particles dispersed in newtonian liquids. *Journal of Rheology* **33**, 329 (1989).

[7] A. K. Townsend and H. J. Wilson. The fluid dynamics of the chocolate fountain. *European Journal of Physics* **37**, 015803 (2016).

[8] C. Servais, R. Jones, and I. Roberts. The influence of particle size distribution on the processing of food. *Journal of Food Engineering* **51**, 201 (2002).

[9] A. Einstein. *Eine neue Bestimmung der Molekul-dimensionen.* PhD thesis, University of Zurich, (1905).

[10] N. Y. C. Lin, M. Bierbaum, P. Schall, J. P. Sethna, and I. Cohen. Measuring nonlinear stresses generated by defects in 3d colloidal crystals. *Nature Materials* **15**, 1172 (2016).

[11] Y. Peng, Z. Wang, A. M. Alsayed, A. G. Yodh, and Y. Han. Melting of colloidal crystal films. *Physical Review Letters* **104**, 205703 (2010).

[12] A. M. Alsayed, M. F. Islam, J. Zhang, P. J. Collings, and A. G. Yodh. Premelting at defects within bulk colloidal crystals. *Science* **309**, 1207 (2005).

[13] G. L. Hunter and E. R. Weeks. The physics of the colloidal glass transition. *Reports on Progress in Physics* **75**, 066501 (2012).

[14] J. Mewis and N. J. Wagner. *Colloidal Suspension Rheology.* Cambridge University Press, Cambridge, UK (2011).

[15] M. M. Denn and J. F. Morris. Rheology of non-brownian suspensions. *Annual Review of Chemical and Biomolecular Engineering* **5**, 203 (2014).

[16] C. D. Cwalina, K. J. Harrison, and N. J. Wagner. Rheology of cubic particles suspended in a newtonian fluid. *Soft Matter* **12**, 4654 (2016).

[17] F. Tapia, S. Shaikh, J. E. Butler, O. Pouliquen, and É. Guazzelli. Rheology of concentrated suspensions of non-colloidal rigid fibres. *Journal of Fluid Mechanics* **827**, R5 (2017).

[18] N. Koumakis, A. Pamvouxoglou, A. S. Poulos, and G. Petekidis. Direct comparison of the rheology of model hard and soft particle glasses. *Soft Matter* **8**, 4271 (2012).

[19] P. F. Luckham and M. A. Ukeje. Effect of particle size distribution on the rheology of dispersed systems. *Journal of Colloid and Interface Science* **220**, 347 (1999).

[20] M. Trulsson, B. Andreotti, and P. Claudin. Transition from the viscous to inertial regime in dense suspensions. *Physical Review Letters* **109**, 118305 (2012).

[21] F. Boyer, É. Guazzelli, and O. Pouliquen. Unifying suspension and granular rheology. *Physical Review Letters* **107**, 188301 (2011).

[22] A. B. Metzner. Rheology of suspensions in polymeric liquids. *Journal of Rheology* **29**, 739 (1985).

[23] H. A. Barnes. A review of the rheology of filled viscoelastic systems. In *Rheology Reviews*, British Society of Rheology (2003).

[24] F. Gadala-Maria and A. Acrivos. Shearinduced structure in a concentrated suspension of solid spheres. *Journal of Rheology* **24**, 799 (1980).

[25] J. F. Morris and E. Guazzelli. *A Physical Introduction to Suspension Dynamics.* Cambridge University Press, Cambridge, UK (2011).

[26] F. Blanc, E. D'Ambrosio, L. Lobry, F. Peters, and E. Lemaire. Universal scaling law in frictional non-brownian suspensions. *Physical Review Fluids* **3**, 114303 (2018).

[27] A. Ikeda, L. Berthier, and P. Sollich. Disentangling glass and jamming physics in the rheology of soft materials. *Soft Matter* **9**, 7669 (2013).

[28] G. K. Batchelor. *An Introduction to Fluid Dynamics.* Royal Society of Chemistry, London, UK (1988).

[29] P. R. Nott, É. Guazzelli, and O. Pouliquen. The suspension balance model revisited. *Physics of Fluids* **23**, 043304 (2011).

[30] R. W. Zwanzig. *Nonequilibrium Statistical Mechanics.* Oxford University Press, Oxford, UK (2001).

[31] G. K. Batchelor. The stress system in a suspension of force-free particles. *Journal of Fluid Mechanics* **41**, 545 (1970).

[32] E. J. Hemingway. *Internally and externally driven flows of complex fluids: viscoelastic active matter, flows in porous media and contact line dynamics.* PhD thesis, Durham University, (2015).

[33] N. Frankel and A. Acrivos. On the viscosity of a concentrated suspension of solid spheres. *Chemical Engineering Science* **22**, 847 (1967).

[34] R. C. Ball and J. R. Melrose. A simulation technique for many spheres in quasi-static motion under frame-invariant pair drag and brownian forces. *Physica A: Statistical Mechanics and its Applications* **247**, 444 (1997).

[35] J. F. Brady and G. Bossis. Stokesian dynamics. *Annual Review of Fluid Mechanics* **20**, 111 (1988).

[36] R. Mari, R. Seto, J. F. Morris, and M. M. Denn. Shear thickening, frictionless and frictional rheologies in non-brownian suspensions. *Journal of Rheology* **58**, 1693 (2014).

[37] W. Noll. *On the Continuity of the Solid and Fluid States.* PhD thesis, Indiana University, (1955).

[38] R. C. Ball and J. R. Melrose. Lubrication breakdown in hydrodynamic simulations of concentrated colloids. *Advances in Colloid and Interface Science* **59**, 19 (1995).

[39] R. Seto, R. Mari, J. F. Morris, and M. M. Denn. Discontinuous shear thickening of frictional hard-sphere suspensions. *Physical Review Letters* **111**, 218301 (2013).

[40] P. A. Cundall and O. D. L. Strack. A discrete numerical model for granular assemblies. *Géotechnique* **29**, 47 (1979).

[41] S. Luding. Cohesive, frictional powders: contact models for tension. *Granular Matter* **10**, 235 (2008).

[42] C. S. O'Hern, L. E. Silbert, A. J. Liu, and S. R. Nagel. Jamming at zero temperature and zero applied stress: The epitome of disorder. *Physical Review E* **68**, 011306 (2003).

[43] P. Chaudhuri, L. Berthier, and S. Sastry. Jamming transitions in amorphous packings of frictionless spheres occur over a continuous range of volume fractions. *Physical Review Letters* **104**, 165701 (2010).

[44] G. D. Scott. Packing of spheres: Packing of equal spheres. *Nature* **188**, 908 (1960).

[45] S. S. Manna and H. J. Herrmann. Precise determination of the fractal dimensions of apollonian packing and space-filling bearings. *Journal of Physics A: Mathematical and General* **24**, L481 (1991).

[46] K. W. Desmond and E. R. Weeks. Influence of particle size distribution on random close packing of spheres. *Physical Review E* **90**, 022204 (2014).

[47] K. W. Desmond and E. R. Weeks. Random close packing of disks and spheres in confined geometries. *Physical Review E* **80**, 051305 (2009).

[48] C. P. Goodrich, A. J. Liu, and S. R. Nagel. Finite-size scaling at the jamming transition. *Physical Review Letters* **109**, 095704 (2012).

[49] R. B. Bird, R. C. Armstrong, and O. Hassager. *Dynamics of Polymeric Liquids.* Wiley, New York, US, 2nd edition (1987).

[50] A. Fall. *Rhéophysique des fluides complexes: Écoulement et Blocage de suspensions concentrées.* PhD thesis, Université Paris-Diderot - Paris VII, (2008).

[51] E. Brown and H. M. Jaeger. Shear thickening in concentrated suspensions: phenomenology, mechanisms and relations to jamming. *Reports on Progress in Physics* **77**, 046602 (2014).

[52] B. M. Guy, M. Hermes, and W. C. K. Poon. Towards a unified description of the rheology of hard-particle suspensions. *Physical Review Letters* **115**, 088304 (2015).

[53] V. Rathee, D. L. Blair, and J. S. Urbach. Localized stress fluctuations drive shear thickening in dense suspensions. *Proceedings of the National Academy of Sciences* **114**, 8740 (2017).

[54] I. R. Peters, S. Majumdar, and H. M. Jaeger. Direct observation of dynamic shear jamming in dense suspensions. *Nature* **532**, 214 (2016).

[55] B. M. Guy, J. A. Richards, D. J. M. Hodgson, E. Blanco, and W. C. K. Poon. Constraint-based approach to granular dispersion rheology. *Physical Review Letters* **121**, 128001 (2018).

[56] M. Wyart and M. E. Cates. Discontinuous shear thickening without inertia in dense non-brownian suspensions. *Physical Review Letters* **112**, 098302 (2014).

[57] R. L. Hoffman. Discontinuous and dilatant viscosity behavior in concentrated suspensions. ii. theory and experimental tests. *Journal of Colloid and Interface Science* **46**, 491 (1974).

[58] R. L. Hoffman. Discontinuous and dilatant viscosity behavior in concentrated suspensions iii. necessary conditions for their occurrence in viscometric flows. *Advances in Colloid and Interface Science* **17**, 161 (1982).

[59] D. P. Kalman and N. J. Wagner. Microstructure of shear-thickening concentrated suspensions determined by flow-usans. *Rheologica Acta* **48**, 897 (2009).

[60] J. Bender and N. J. Wagner. Reversible shear thickening in monodisperse and bidisperse colloidal dispersions. *Journal of Rheology* **40**, 899 (1996).

[61] B. J. Maranzano and N. J. Wagner. Flow-small angle neutron scattering measurements of colloidal dispersion microstructure evolution through the shear thickening transition. *The Journal of Chemical Physics* **117**, 10291 (2002).

[62] X. Cheng, J. H. McCoy, J. N. Israelachvili, and I. Cohen. Imaging the microscopic structure of shear thinning and thickening colloidal suspensions. *Science* **333**, 1276 (2011).

[63] J. F. Brady and G. Bossis. The rheology of concentrated suspensions of spheres in simple shear flow by numerical simulation. *Journal of Fluid Mechanics* **155**, 105 (1985).

[64] R. S. Farr, J. R. Melrose, and R. C. Ball. Kinetic theory of jamming in hard-sphere startup flows. *Physical Review E* **55**, 7203 (1997).

[65] O. Reynolds. Lvii. on the dilatancy of media composed of rigid particles in contact. with experimental illustrations. *The London, Edinburgh, and Dublin Philosophical Magazine and Journal of Science* **20**, 469 (1885).

[66] A. Fall, N. Huang, F. Bertrand, G. Ovarlez, and D. Bonn. Shear thickening of cornstarch suspensions as a reentrant jamming transition. *Physical Review Letters* **100**, 018301 (2008).

[67] A. Fall, F. Bertrand, G. Ovarlez, and D. Bonn. Shear thickening of cornstarch suspensions. *Journal of Rheology* **56**, 575 (2012).

[68] H. Nakanishi, S.-i. Nagahiro, and N. Mitarai. Fluid dynamics of dilatant fluids. *Physical Review E* **85**, 011401 (2012).

[69] E. Brown and H. M. Jaeger. The role of dilation and confining stresses in shear thickening of dense suspensions. *Journal of Rheology* **56**, 875 (2012).

[70] S. R. Raghavan and S. A. Khan. Shear-thickening response of fumed silica suspensions under steady and oscillatory shear. *Journal of Colloid and Interface Science* **185**, 57 (1997).

[71] V. Gopalakrishnan and C. F. Zukoski. Effect of attractions on shear thickening in dense suspensions. *Journal of Rheology* **48**, 1321 (2004).

[72] C. O. Osuji, C. Kim, and D. A. Weitz. Shear thickening and scaling of the elastic modulus in a fractal colloidal system with attractive interactions. *Physical Review E* **77**, 060402 (2008).

[73] D. Lootens, H. van Damme, Y. Hémar, and P. Hébraud. Dilatant flow of concentrated suspensions of rough particles. *Physical Review Letters* **95**, 268302 (2005).

[74] I. A. Bashkirtseva, A. Y. Zubarev, L. Y. Iskakova, and L. B. Ryashko. On rheophysics of high-concentrated suspensions. *Colloid Journal* **71**, 446 (2009).

[75] N. Fernandez, R. Mani, D. Rinaldi, D. Kadau, M. Mosquet, H. Lombois-Burger, J. Cayer-Barrioz, H. J. Herrmann, N. D. Spencer, and L. Isa. Microscopic mechanism for shear thickening of non-brownian suspensions. *Physical Review Letters* **111**, 108301 (2013).

[76] C. Heussinger. Shear thickening in granular suspensions: Interparticle friction and dynamically correlated clusters. *Physical Review E* **88**, 050201 (2013).

[77] R. Mari, R. Seto, J. F. Morris, and M. M. Denn. Discontinuous shear thickening in brownian suspensions by dynamic simulation. *Proceedings of the National Academy of Sciences* **112**, 15326 (2015).

[78] N. Y. C. Lin, B. M. Guy, M. Hermes, C. Ness, J. Sun, W. C. K. Poon, and I. Cohen. Hydrodynamic and contact contributions to continuous shear thickening in colloidal suspensions. *Physical Review Letters* **115**, 228304 (2015).

[79] J. Comtet, G. Chatté, A. Niguès, L. Bocquet, A. Siria, and A. Colin. Pairwise frictional profile between particles determines discontinuous shear thickening transition in non-colloidal suspensions. *Nature Communications* **8**, 15633 (2017).

[80] C. Clavaud, A. Bérut, B. Metzger, and Y. Forterre. Revealing the frictional transition in shear-thickening suspensions. *Proceedings of the National Academy of Sciences* **114**, 5147 (2017).

[81] L. C. Hsiao, S. Jamali, E. Glynos, P. F. Green, R. G. Larson, and M. J. Solomon. Rheological state diagrams for rough colloids in shear flow. *Physical Review Letters* **119**, 158001 (2017).

[82] C.-P. Hsu, S. N. Ramakrishna, M. Zanini, N. D. Spencer, and L. Isa. Roughness-dependent tribology effects on discontinuous shear thickening. *Proceedings of the National Academy of Sciences* **115**, 5117 (2018).

[83] G. Chatté, J. Comtet, A. Niguès, L. Bocquet, A. Siria, G. Ducouret, F. Lequeux, N. Lenoir, G. Ovarlez, and A. Colin. Shear thinning in non-brownian suspensions. *Soft Matter* **14**, 879 (2018).

[84] Z. Zhou, P. J. Scales, and D. V. Boger. Chemical and physical control of the rheology of concentrated metal oxide suspensions. *Chemical Engineering Science* **56**, 2901 (2001).

[85] H. J. Wilson and R. H. Davis. The viscosity of a dilute suspension of rough spheres. *Journal of Fluid Mechanics* **421**, S0022112000001695 (2000).

[86] M. Otsuki and H. Hayakawa. Critical scaling near jamming transition for frictional granular particles. *Physical Review E - Statistical, Nonlinear, and Soft Matter Physics* **83**, 5 (2011).

[87] S. Gallier, E. Lemaire, F. Peters, and L. Lobry. Rheology of sheared suspensions of rough frictional particles. *Journal of Fluid Mechanics* **757**, 514 (2014).

[88] J. Y. Moon, S. Dai, L. Chang, J. S. Lee, and R. I. Tanner. The effect of sphere roughness on the rheology of concentrated suspensions. *Journal of Non-Newtonian Fluid Mechanics* **223**, 233 (2015).

[89] F. Peters, G. Ghigliotti, S. Gallier, F. Blanc, E. Lemaire, and L. Lobry. Rheology of non-brownian suspensions of rough frictional particles under shear reversal: A numerical study. *Journal of Rheology* **60**, 715 (2016).

[90] J. R. Royer, D. L. Blair, and S. D. Hudson. Rheological signature of frictional interactions in shear thickening suspensions. *Physical Review Letters* **116**, 188301 (2016).

[91] A. K. Townsend and H. J. Wilson. Frictional shear thickening in suspensions: The effect of rigid asperities. *Physics of Fluids* **29**, 121607 (2017).

[92] N. M. James, E. Han, R. A. L. de la Cruz, J. Jureller, and H. M. Jaeger. Interparticle hydrogen bonding can elicit shear jamming in dense suspensions. *Nature Materials* **17**, 965 (2018).

[93] R. Mari, R. Seto, J. F. Morris, and M. M. Denn. Nonmonotonic flow curves of shear thickening suspensions. *Physical Review E* **91**, 052302 (2015).

[94] Z. Pan, H. de Cagny, B. Weber, and D. Bonn. S-shaped flow curves of shear thickening suspensions: Direct observation of frictional rheology. *Physical Review E* **92**, 032202 (2015).

[95] M. Hermes, B. M. Guy, W. C. K. Poon, G. Poy, M. E. Cates, and M. Wyart. Unsteady flow and particle migration in dense, non-brownian suspensions. *Journal of Rheology* **60**, 905 (2016).

[96] G. Bossis, P. Boustingorry, Y. Grasselli, A. Meunier, R. Morini, A. Y. Zubarev, and O. Volkova. Discontinuous shear thickening in the presence of polymers adsorbed on the surface of calcium carbonate particles. *Rheologica Acta* **56**, 415 (2017).

[97] B. Saint-Michel, T. Gibaud, and S. Manneville. Uncovering instabilities in the spatiotemporal dynamics of a shear-thickening cornstarch suspension. *Physical Review X* **8**, 031006 (2018).

[98] R. N. Chacko, R. Mari, M. E. Cates, and S. M. Fielding. Dynamic vorticity banding in discontinuously shear thickening suspensions. *Physical Review Letters* **121**, 108003 (2018).

[99] J. Yerushalmi, S. Katz, and R. Shinnar. The stability of steady shear flows of some viscoelastic fluids. *Chemical Engineering Science* **25**, 1891 (1970).

[100] P. D. Olmsted. Perspectives on shear banding in complex fluids. *Rheologica Acta* **47**, 283 (2008).

[101] C.-Y. D. Lu, P. D. Olmsted, and R. C. Ball. Effects of nonlocal stress on the determination of shear banding flow. *Physical Review Letters* **84**, 642 (2000).

[102] P. D. Olmsted and C.-Y. D. Lu. Coexistence and phase separation in sheared complex fluids. *Physical Review E* **56**, R55 (1997).

[103] S. M. Fielding and P. D. Olmsted. Flow phase diagrams for concentration-coupled shear banding. *The European Physical Journal E* **11**, 65 (2003).

[104] M. Neuville, G. Bossis, J. Persello, O. Volkova, P. Boustingorry, and M. Mosquet. Rheology of a gypsum suspension in the presence of different superplasticizers. *Journal of Rheology* **56**, 435 (2012).

[105] P. R. Nott and J. F. Brady. Pressure-driven flow of suspensions: simulation and theory. *Journal of Fluid Mechanics* **275**, 157 (1994).

[106] J. F. Morris and F. Boulay. Curvilinear flows of noncolloidal suspensions: The role of normal stresses. *Journal of Rheology* **43**, 1213 (1999).

[107] Y. Yurkovetsky and J. F. Morris. Particle pressure in sheared brownian suspensions. *Journal of Rheology* **52**, 141 (2008).

[108] D. Lhuillier. Migration of rigid particles in non-brownian viscous suspensions. *Physics of Fluids* **21**, 023302 (2009).

[109] M. A. van der Hoef, R. Beetstra, and J. A. M. Kuipers. Lattice-boltzmann simulations of low-reynolds-number flow past mono- and bidisperse arrays of spheres: results for the permeability and drag force. *Journal of Fluid Mechanics* **528**, 233 (2005).

[110] J. G. Berryman. Random close packing of hard spheres and disks. *Physical Review A* **27**, 1053 (1983).

[111] A. W. Lees and S. F. Edwards. The computer study of transport processes under extreme conditions. *Journal of Physics C: Solid State Physics* **5**, 1921 (1972).

[112] A. Singh, R. Mari, M. M. Denn, and J. F. Morris. A constitutive model for simple shear of dense frictional suspensions. *Journal of Rheology* **62**, 457 (2018).

[113] D. Bi, J. Zhang, B. Chakraborty, and R. P. Behringer. Jamming by shear. *Nature* **480**, 355 (2011).

[114] G. Düring, E. Lerner, and M. Wyart. Length scales and self-organization in dense suspension flows. *Physical Review E* **89**, 022305 (2014).

[115] R. Besseling, L. Isa, P. Ballesta, G. Petekidis, M. E. Cates, and W. C. K. Poon. Shear banding and flow-concentration coupling in colloidal glasses. *Physical Review Letters* **105**, 268301 (2010).

[116] R. N. Chacko, R. Mari, S. M. Fielding, and M. E. Cates. Shear reversal in dense suspensions: the challenge to fabric evolution models from simulation data. *Journal of Fluid Mechanics* **847**, 700 (2018).

[117] A. Fall, F. Bertrand, D. Hautemayou, C. Mezière, P. Moucheront, A. Lemaître, and G. Ovarlez. Macroscopic discontinuous shear thickening versus local shear jamming in cornstarch. *Physical Review Letters* **114**, 098301 (2015).

[118] W. H. Press, S. A. Teukolsky, W. T. Vetterling, and B. P. Flannery. *Numerical Recipes*. Cambridge University Press, Cambridge, UK, 3rd edition (2007).

[119] M. Frigo. A fast fourier transform compiler. *ACM SIGPLAN Notices* **34**, 169 (1999).

[120] A. Sierou and J. F. Brady. Rheology and microstructure in concentrated noncolloidal suspensions. *Journal of Rheology* **46**, 1031 (2002).

[121] G. Drazer, J. Koplik, B. Khusid, and A. Acrivos. Deterministic and stochastic behaviour of non-brownian spheres in sheared suspensions. *Journal of Fluid Mechanics* **460**, 307 (2002).

[122] G. Drazer, J. Koplik, B. Khusid, and A. Acrivos. Microstructure and velocity fluctuations in sheared suspensions. *Journal of Fluid Mechanics* **511**, 237 (2004).

[123] F. Blanc, F. Peters, and E. Lemaire. Experimental signature of the pair trajectories of rough spheres in the shear-induced microstructure in noncolloidal suspensions. *Physical Review Letters* **107**, 208302 (2011).

[124] F. Blanc, E. Lemaire, A. Meunier, and F. Peters. Microstructure in sheared non-brownian concentrated suspensions. *Journal of Rheology* **57**, 273 (2013).

[125] C. Ness and J. Sun. Flow regime transitions in dense non-brownian suspensions: Rheology, microstructural characterization, and constitutive modeling. *Physical Review E* **91**, 012201 (2015).

[126] R. Seto, G. G. Giusteri, and A. Martiniello. Microstructure and thickening of dense suspensions under extensional and shear flows. *Journal of Fluid Mechanics* **825**, R3 (2017).

[127] O. Cheal and C. Ness. Rheology of dense granular suspensions under extensional flow. *Journal of Rheology* **62**, 501 (2018).

[128] G. K. Batchelor and J. T. Green. The hydrodynamic interaction of two small freely-moving spheres in a linear flow field. *Journal of Fluid Mechanics* **56**, 375 (1972).

[129] N. J. Wagner and B. J. Ackerson. Analysis of nonequilibrium structures of shearing colloidal suspensions. *The Journal of Chemical Physics* **97**, 1473 (1992).

[130] A. K. Gurnon and N. J. Wagner. Microstructure and rheology relationships for shear thickening colloidal dispersions. *Journal of Fluid Mechanics* **769**, 242 (2015).

[131] I. E. Zarraga, D. A. Hill, and D. T. Leighton. The characterization of the total stress of concentrated suspensions of noncolloidal spheres in newtonian fluids. *Journal of Rheology* **44**, 185 (2000).

[132] A. Singh and P. R. Nott. Experimental measurements of the normal stresses in sheared stokesian suspensions. *Journal of Fluid Mechanics* **490**, S0022112003005366 (2003).

[133] É. Couturier, F. Boyer, O. Pouliquen, and É. Guazzelli. Suspensions in a tilted trough: second normal stress difference. *Journal of Fluid Mechanics* **686**, 26 (2011).

[134] S. Dai, E. Bertevas, F. Qi, and R. I. Tanner. Viscometric functions for noncolloidal sphere suspensions with newtonian matrices. *Journal of Rheology* **57**, 493 (2013).

[135] T. Dbouk, L. Lobry, and E. Lemaire. Normal stresses in concentrated non-brownian suspensions. *Journal of Fluid Mechanics* **715**, 239 (2013).

[136] A. Boromand, S. Jamali, B. Grove, and J. M. Maia. A generalized frictional and hydrodynamic model of the dynamics and structure of dense colloidal suspensions. *Journal of Rheology* **62**, 905 (2018).

[137] R. Seto and G. G. Giusteri. Normal stress differences in dense suspensions. *Journal of Fluid Mechanics* **857**, 200 (2018).

[138] N. Y. C. Lin, C. Ness, M. E. Cates, J. Sun, and I. Cohen. Tunable shear thickening in suspensions. *Proceedings of the National Academy of Sciences* **113**, 10774 (2016).

[139] C. Ness, R. Mari, and M. E. Cates. Shaken and stirred: Random organization reduces viscosity and dissipation in granular suspensions. *Science Advances* **4**, eaar3296 (2018).

[140] F. Parsi and F. Gadala-Maria. Foreandaft asymmetry in a concentrated suspension of solid spheres. *Journal of Rheology* **31**, 725 (1987).

[141] H. J. Wilson. An analytic form for the pair distribution function and rheology of a dilute suspension of rough spheres in plane strain flow. *Journal of Fluid Mechanics* **534**, 97 (2005).

[142] E. Nazockdast and J. F. Morris. Pair-particle dynamics and microstructure in sheared colloidal suspensions: Simulation and smoluchowski theory. *Physics of Fluids* **25**, 070601 (2013).

[143] D. T. Leighton and A. Acrivos. Viscous resuspension. *Chemical Engineering Science* **41**, 1377 (1986).

[144] A. Fall, F. Bertrand, G. Ovarlez, and D. Bonn. Yield stress and shear banding in granular suspensions. *Physical Review Letters* **103**, 178301 (2009).

[145] V. G. Kolli, E. J. Pollauf, and F. Gadala-Maria. Transient normal stress response in a concentrated suspension of spherical particles. *Journal of Rheology* **46**, 321 (2002).

[146] T. Narumi, H. See, Y. Honma, T. Hasegawa, T. Takahashi, and N. Phan-Thien. Transient response of concentrated suspensions after shear reversal. *Journal of Rheology* **46**, 295 (2002).

[147] F. Blanc, F. Peters, and E. Lemaire. Local transient rheological behavior of concentrated suspensions. *Journal of Rheology* **55**, 835 (2011).

[148] F. Boyer, O. Pouliquen, and É. Guazzelli. Dense suspensions in rotating-rod flows: normal stresses and particle migration. *Journal of Fluid Mechanics* **686**, 5 (2011).

[149] C. Gamonpilas, J. F. Morris, and M. M. Denn. Shear and normal stress measurements in non-brownian monodisperse and bidisperse suspensions. *Journal of Rheology* **60**, 289 (2016).

[150] C. Gamonpilas, J. F. Morris, and M. M. Denn. Erratum: shear and normal stress measurements in non-brownian monodisperse and bidisperse suspensions [j. rheol. 60 (2), 289296 (2016)]. *Journal of Rheology* **62**, 665 (2018).

[151] E. Bertevas, X.-j. Fan, and R. I. Tanner. Simulation of the rheological properties of suspensions of oblate spheroidal particles in a newtonian fluid. *Rheologica Acta* **49**, 53 (2010).

[152] E. J. Hinch and L. G. Leal. Constitutive equations in suspension mechanics. part 1. general formulation. *Journal of Fluid Mechanics* **71**, 481 (1975).

[153] R. G. Larson. *Constitutive Equations for Polymer Melts and Solutions.* Butterworth-Heinemann, Boston, US (1988).

[154] M. Johnson and D. Segalman. A model for viscoelastic fluid behavior which allows non-affine deformation. *Journal of Non-Newtonian Fluid Mechanics* **2**, 255 (1977).

[155] H. Giesekus. A simple constitutive equation for polymer fluids based on the concept of deformation-dependent tensorial mobility. *Journal of Non-Newtonian Fluid Mechanics* **11**, 69 (1982).

[156] C. Ness and J. Sun. Shear thickening regimes of dense non-brownian suspensions. *Soft Matter* **12**, 914 (2016).

[157] N. Phan-Thien. Constitutive equation for concentrated suspensions in newtonian liquids. *Journal of Rheology* **39**, 679 (1995).

[158] N. Phan-Thien, X.-J. Fan, and B. C. Khoo. A new constitutive model for monodispersed suspensions of spheres at high concentrations. *Rheologica Acta* **38**, 297 (1999).

[159] J. J. Stickel, R. J. Phillips, and R. L. Powell. A constitutive model for microstructure and total stress in particulate suspensions. *Journal of Rheology* **50**, 379 (2006).

[160] J. D. Goddard. A dissipative anisotropic fluid model for non-colloidal particle dispersions. *Journal of Fluid Mechanics* **568**, 1 (2006).

[161] O. Ozenda, P. Saramito, and G. Chambon. A new rate-independent tensorial model for suspensions of noncolloidal rigid particles in newtonian fluids. *Journal of Rheology* **62**, 889 (2018).

[162] J. J. J. Gillissen and H. J. Wilson. Modeling sphere suspension microstructure and stress. *Physical Review E* **98**, 033119 (2018).

[163] J. J. Stickel, R. J. Phillips, and R. L. Powell. Application of a constitutive model for particulate suspensions: Time-dependent viscometric flows. *Journal of Rheology* **51**, 1271 (2007).

[164] C. Gao, S. D. Kulkarni, J. F. Morris, and J. F. Gilchrist. Direct investigation of anisotropic suspension structure in pressure-driven flow. *Physical Review E* **81**, 041403 (2010).

[165] S. Deboeuf, N. Lenoir, D. Hautemayou, M. Bornert, F. Blanc, and G. Ovarlez. Imaging non-brownian particle suspensions with x-ray tomography: Application to the microstructure of newtonian and viscoplastic suspensions. *Journal of Rheology* **62**, 643 (2018).

[166] É. Guazzelli and O. Pouliquen. Rheology of dense granular suspensions. *Journal of Fluid Mechanics* **852**, P1 (2018).

[167] G. L. Hand. A theory of anisotropic fluids. *Journal of Fluid Mechanics* **13**, 33 (1962).

[168] C. Ness and J. Sun. Two-scale evolution during shear reversal in dense suspensions. *Physical Review E* **93**, 012604 (2016).

[169] F. Blanc, E. Lemaire, and F. Peters. Tunable fall velocity of a dense ball in oscillatory cross-sheared concentrated suspensions. *Journal of Fluid Mechanics* **746**, R4 (2014).

[170] A. K. Townsend and H. J. Wilson. Simulations of a heavy ball falling through a sheared suspension. *Journal of Engineering Mathematics* **107**, 179 (2017).

[171] J. F. Morris and B. Katyal. Microstructure from simulated brownian suspension flows at large shear rate. *Physics of Fluids* **14**, 1920 (2002).

[172] E. Nazockdast and J. F. Morris. Microstructural theory and the rheology of concentrated colloidal suspensions. *Journal of Fluid Mechanics* **713**, 420 (2012).

[173] V. Magnanimo and S. Luding. A local constitutive model with anisotropy for ratcheting under 2d axial-symmetric isobaric deformation. *Granular Matter* **13**, 225 (2011).

[174] J. Sun and S. Sundaresan. A constitutive model with microstructure evolution for flow of rate-independent granular materials. *Journal of Fluid Mechanics* **682**, 590 (2011).

[175] J. D. Goddard. Continuum modeling of granular media. *Applied Mechanics Reviews* **66**, 050801 (2014).

[176] N. Kuzuu and M. Doi. Constitutive equation for nematic liquid crystals under weak velocity gradient derived from a molecular kinetic equation. *Journal of the Physical Society of Japan* **52**, 3486 (1983).

[177] H. See, M. Doi, and R. G. Larson. The effect of steady flow fields on the isotropicnematic phase transition of rigid rodlike polymers. *The Journal of Chemical Physics* **92**, 792 (1990).

[178] K.-I. Kanatani. Distribution of directional data and fabric tensors. *International Journal of Engineering Science* **22**, 149 (1984).

[179] R. Rivlin. Further remarks on the stress-deformation relations for isotropic materials. *Indiana University Mathematics Journal* **4**, 681 (1955).

[180] J. Cheng, X. Z. Jia, and Y. B. Wang. Numerical differentiation and its applications. *Inverse Problems in Science and Engineering* **15**, 339 (2007).

[181] J. Feng, C. V. Chaubal, and L. G. Leal. Closure approximations for the doi theory: Which to use in simulating complex flows of liquid-crystalline polymers? *Journal of Rheology* **42**, 1095 (1998).

[182] E. J. Hinch and L. G. Leal. Constitutive equations in suspension mechanics. part 2. approximate forms for a suspension of rigid particles affected by brownian rotations. *Journal of Fluid Mechanics* **76**, 187 (1976).

[183] M. Doi. Molecular dynamics and rheological properties of concentrated solutions of rodlike polymers in isotropic and liquid crystalline phases. *Journal of Polymer Science: Polymer Physics Edition* **19**, 229 (1981).

[184] D. Barthés-Biesel and A. Acrivos. The rheology of suspensions and its relation to phenomenological theories for non-newtonian fluids. *International Journal of Multiphase Flow* **1**, 1 (1973).

[185] E. M. Stein and G. Weiss. *Introduction to Fourier Analysis on Euclidean Spaces*. Princeton University Press, Princeton, USA (1971).

[186] L. Qi. Rank and eigenvalues of a supersymmetric tensor, the multivariate homogeneous polynomial and the algebraic hypersurface it defines. *Journal of Symbolic Computation* **41**, 1309 (2006).

[187] C. Bingham. An antipodally symmetric distribution on the sphere. *The Annals of Statistics* **2**, 1201 (1974).

[188] K. V. Mardia and P. E. Jupp. *Directional Statistics*. Wiley, Chichester, UK (1999).

[189] E. C. Bingham. *Fluidity and Plasticity*. McGraw Hill, New York, US (1922).

[190] D. Bonn, M. M. Denn, L. Berthier, T. Divoux, and S. Manneville. Yield stress materials in soft condensed matter. *Reviews of Modern Physics* **89**, 035005 (2017).

[191] A. Ikeda, L. Berthier, and P. Sollich. Unified study of glass and jamming rheology in soft particle systems. *Physical Review Letters* **109**, 018301 (2012).

[192] P. C. F. Møller, J. Mewis, and D. Bonn. Yield stress and thixotropy: on the difficulty of measuring yield stresses in practice. *Soft Matter* **2**, 274 (2006).

[193] P. Sollich, F. Lequeux, P. Hébraud, and M. E. Cates. Rheology of soft glassy materials. *Physical Review Letters* **78**, 2020 (1997).

[194] P. Sollich. Rheological constitutive equation for a model of soft glassy materials. *Physical Review E* **58**, 738 (1998).

[195] G. Picard, A. Ajdari, F. Lequeux, and L. Bocquet. Elastic consequences of a single plastic event: A step towards the microscopic modeling of the flow of yield stress fluids. *European Physical Journal E* **15**, 371 (2004).

[196] C. E. Maloney and A. Lemaître. Amorphous systems in athermal, quasistatic shear. *Physical Review E* **74**, 016118 (2006).

[197] F. Puosi, J. Rottler, and J.-L. Barrat. Time-dependent elastic response to a local shear transformation in amorphous solids. *Physical Review E* **89**, 042302 (2014).

[198] J. D. Eshelby. The determination of the elastic field of an ellipsoidal inclusion, and related problems. *Proceedings of the Royal Society A: Mathematical, Physical and Engineering Sciences* **241**, 376 (1957).

[199] N. P. Bailey, J. Schiøtz, A. Lemaître, and K. W. Jacobsen. Avalanche size scaling in sheared three-dimensional amorphous solid. *Physical Review Letters* **98**, 095501 (2007).

[200] A. Lemaître and C. Caroli. Rate-dependent avalanche size in athermally sheared amorphous solids. *Physical Review Letters* **103**, 065501 (2009).

[201] A. Lemaître. Structural relaxation is a scale-free process. *Physical Review Letters* **113**, 245702 (2014).

[202] D. J. Durian. Foam mechanics at the bubble scale. *Physical Review Letters* **75**, 4780 (1995).

[203] E. Flenner and G. Szamel. Relaxation in a glassy binary mixture: Mode-coupling-like power laws, dynamic heterogeneity, and a new non-gaussian parameter. *Physical Review E* **72**, 011205 (2005).

[204] K. M. Salerno, C. E. Maloney, and M. O. Robbins. Avalanches in strained amorphous solids: Does inertia destroy critical behavior? *Physical Review Letters* **109**, 105703 (2012).

[205] C. Liu, E. E. Ferrero, F. Puosi, J.-L. Barrat, and K. Martens. Driving rate dependence of avalanche statistics and shapes at the yielding transition. *Physical Review Letters* **116**, 065501 (2016).

[206] R. D. Groot and P. B. Warren. Dissipative particle dynamics: Bridging the gap between atomistic and mesoscopic simulation. *The Journal of Chemical Physics* **107**, 4423 (1997).

[207] M. Kapnistos, D. Vlassopoulos, G. Fytas, K. Mortensen, G. Fleischer, and J. Roovers. Reversible thermal gelation in soft spheres. *Physical Review Letters* **85**, 4072 (2000).

[208] J. J. Crassous, M. Siebenbürger, M. Ballauff, M. Drechsler, O. Henrich, and M. Fuchs. Thermosensitive core-shell particles as model systems for studying the flow behavior of concentrated colloidal dispersions. *The Journal of Chemical Physics* **125**, 204906 (2006).

[209] E. H. Purnomo, D. van den Ende, S. A. Vanapalli, and F. Mugele. Glass transition and aging in dense suspensions of thermosensitive microgel particles. *Physical Review Letters* **101**, 238301 (2008).

[210] S. Karmakar, C. Dasgupta, and S. Sastry. Length scales in glass-forming liquids and related systems: a review. *Reports on Progress in Physics* **79**, 016601 (2016).

[211] M. L. Falk and J. S. Langer. Dynamics of viscoplastic deformation in amorphous solids. *Physical Review E* **57**, 7192 (1998).

[212] A. Tanguy, F. Leonforte, and J.-L. Barrat. Plastic response of a 2d lennard-jones amorphous solid: Detailed analysis of the local rearrangements at very slow strain rate. *The European Physical Journal E* **20**, 355 (2006).

[213] A. Lemaître and C. Caroli. Plastic response of a two-dimensional amorphous solid to quasistatic shear: Transverse particle diffusion and phenomenology of dissipative events. *Physical Review E - Statistical, Nonlinear, and Soft Matter Physics* **76**, 1 (2007).

[214] R. Dasgupta, H. G. E. Hentschel, and I. Procaccia. Microscopic mechanism of shear bands in amorphous solids. *Physical Review Letters* **109**, 255502 (2012).

[215] K. W. Desmond and E. R. Weeks. Measurement of stress redistribution in flowing emulsions. *Physical Review Letters* **115**, 098302 (2015).

[216] A. Lemaître. Tensorial analysis of eshelby stresses in 3d supercooled liquids. *The Journal of Chemical Physics* **143**, 164515 (2015).

[217] T. Albaret, A. Tanguy, F. Boioli, and D. Rodney. Mapping between atomistic simulations and eshelby inclusions in the shear deformation of an amorphous silicon model. *Physical Review E* **93**, 053002 (2016).

[218] J. Chattoraj and A. Lemaître. Elastic signature of flow events in supercooled liquids under shear. *Physical Review Letters* **111**, 066001 (2013).

[219] B. Illing, S. Fritschi, D. Hajnal, C. Klix, P. Keim, and M. Fuchs. Strain pattern in supercooled liquids. *Physical Review Letters* **117**, 208002 (2016).

[220] S. Gelin, H. Tanaka, and A. Lemaître. Anomalous phonon scattering and elastic correlations in amorphous solids. *Nature Materials* **15**, 1177 (2016).

[221] M. P. Allen and D. J. Tildesley. *Computer Simulation of Liquids*. Oxford University Press, Oxford, UK, 2nd edition (2017).

[222] U. Welling and G. Germano. Efficiency of linked cell algorithms. *Computer Physics Communications* **182**, 611 (2011).

[223] D. Rapaport. Large-scale molecular dynamics simulation using vector and parallel computers. *Computer Physics Reports* **9**, 1 (1988).

[224] B. M. Guy, C. Ness, M. Hermes, L. J. Sawiak, J. Sun, and W. C. K. Poon. Testing the Wyart-Cates model for non-Brownian shear thickening using bidisperse suspensions. arXiv:1901.02066.